Application of X-ray phase imaging in the estimation of tissue optical scattering

Charlotte Joanna Maughan Jones

Department of Medical Physics and Biomedical Engineering
University College London

A thesis submitted for the degree of Doctor of Philosophy

I, Charlotte Joanna Maughan Jones confirm that the work presented in this thesis is my own. Where information has been derived from other sources, I confirm that this has been indicated in the thesis.

Signed……

Date……

Publications

The following peer reviewed publications include results from, and therefore are directly quoted within this thesis:

1. Charlotte J. Maughan Jones, Peter R. T. Munro, "Development of a reliable and reproducible phantom manufacturing method using silica microspheres in silicone," J. Biomed. Opt. 22(9) 095004 (18 September 2017)
2. Charlotte J. Maughan Jones, Fabio A. Vittoria, Alessandro Olivo, Marco Endrizzi, and Peter R. T. Munro, "Retrieval of weak x-ray scattering using edge illumination," Opt. Lett.43, 3874-3877 (2018)
3. Charlotte J. Maughan Jones and Peter R. T. Munro, "Stability of gel wax based optical scattering phantoms," Biomed. Opt. Express 9, 3495-3502 (2018)

Acknowledgements

I would like to thank my primary supervisor Dr Peter Munro, firstly for taking a chance on a biology graduate with a physics-based PhD, but also and for his patience with me as I learnt a whole new subject area, and his confidence in my abilities, when my own confidence was lacking. I also am eternally grateful for the support I received during my pregnancy, through my maternity leave, and on returning to study, and I appreciate how lucky I am to have been able to stop and start my work so seamlessly. I would also like to thank all the members of the advanced x-ray group, including my second supervisor, Prof. Sandro Olivo, for their fruitful discussions and debates regarding all areas of phase contrast imaging. Special thanks to Dr Anna Zamir and Dr Fabio Vittoria, who, without question, helped to run my synchrotron experiments, when I found out I was pregnant less than two months before I was due to fly out to the facility. Finally, to Alberto Mittone for his help in performing the experiments at ESRF, and subsequent discussions about the results.

Spelling and Grammar are not strengths of mine, therefore I am eternally grateful for my little army of proof readers (Penny Tobin, Jasmine Bundock, Natalie Cheese and Sarah Knight), who have a much greater understanding of the correct use of a semi colon than I do. Thank you for giving up your precious time, and for at least pretending it was an interesting document to read.

To my friends (Lizzie, Caroline, Jasmine and Rachel), thank you for your support during my pregnancy and early motherhood. I couldn't have done it without you all. Thank you also for giving me sanity during my PhD, and for the laughs and happiness that your presence in my life brings.

When you have spent 5 hard years training to become a Veterinary surgeon, then, unexpectedly have to say goodbye to that dream only 4 years into your career, it is terrifying. However, I have to say a huge thank you to my parents (Angela and Philip), for never once questioning my decision to abandon the stethoscope for the laboratory, and for supporting me unconditionally with my research journey.

Thank you to the NHS for everything you have done for me during my PhD. To the midwives, doctors and consultants who brought my son safely into the

world, the physiotherapists for helping me deal with my severe birth injury, and especially to Lois, the women's health councillor, for letting me cry, and for giving me the tools to live with my birth trauma whilst constantly believing in my ability to overcome adversity. You are all greater than you realise.

Finally, I would like to thank my wonderful little family, my husband James, and our beautiful son Arlo, I love you both very much. James, thank you for never questioning my decision to leave veterinary practice, and for your emotional support during that difficult time in our lives. Thank you also for financially supporting us, and for staying in a career that I know you were not all that happy in to enable me to follow my passion, I promise that one day, I will return the favour. Arlo, thank you for giving me a new lease of life, for making me realise what I was born to do, and for learning to sleep through the night a whole 2 weeks before the end of my PhD (although If you could sleep past 5.30am, that would be great). You have given me the motivation to succeed in life, so you can be proud of your mummy and what she has achieved, even if she has taken it a little longer to get there than most.

Abstract

The ability to non-invasively estimate the optical properties of biological tissues *in vivo* would enable the advancement of quantitative optical based techniques such as photoacoustic imaging. It has, to date, proven difficult to make such an estimation for large three-dimensional tissue sections and small animals using optical approaches. To overcome this limitation, the correlation between the optical scattering properties, and the dark field x-ray phase contrast (XPCi), or 'x-ray scattering' signal has been investigated. To do this, phantoms with unknown x-ray scattering, but controlled optical scattering were designed, and manufacturing methods developed, to enable simultaneous manufacture of phantoms suitable for either x-ray or optical imaging. Phantoms consisted of agarose, gel wax or silicone embedded with either TiO_2 powder or silica microspheres. The x-ray phantoms were imaged using the edge illumination (EI) system at UCL. Due to the very low scattering and high absorption of many of the samples, along with the imperfect absorption of the masks in the EI system, existing scatter retrieval methods were unable to accurately determine the scattering properties of the phantoms. A novel, more sensitive x-ray scatter retrieval method was thus developed to overcome these problems. The optical scattering of phantoms was retrieved using a spectrophotometer combined the inverse adding doubling method. The optical and x-ray scattering of the phantoms was thus compared which did not reveal any correlation between the two.

In order to assess a correlation between optical and x-ray scattering in biological tissue, Optical coherence tomography (OCT) was investigated as a method of determining the optical scattering properties. Along with the use of a controlled 'calibration phantom', the optical properties of such tissues were determined. Finally, biological tissue samples were imaged using both OCT and EI-XPCi, and the optical and x-ray scattering properties compared, with no correlation observed.

Central Hypothesis

I hypothesise that the x-ray scattering signal retrieved from the edge illumination x-ray phase contrast (EI-XPCi) system at UCL can be used to predict the optical scattering properties of biological tissues.

Null Hypothesis

There is no correlation between the x-ray scattering signal retrieved from the EI-XPCi system and the optical scattering properties of biological tissues.

Impact Statement

The work presented in this thesis has had some immediate impacts within the field of medical imaging, but also has the potential to lead to future clinical and diagnostic developments within clinical practice.

Firstly, the method presented in this thesis for creating silicone and silica microsphere phantoms which was disseminated via open access publication[1], has already been cited by other research groups. This illustrates that the wider research community is already utilizing, and therefore benefiting from the results obtained here.

The International Photoacoustic Standardisation Consortium has adopted gel wax as one of the "most promising stable phantom materials", as discussed in a letter written in Nature Photonics[2]. The results presented within this thesis, and disseminated via open access publication[3] regarding the instability of gel wax phantoms, will aid the development of gel wax as the phantom standard for photoacoustic imaging, and could translate to other imaging modalities due to its simple manufacturing method and cost effective nature.

The scattering retrieval algorithm developed and tested in this thesis, known as the "Three Gaussian Retrieval", has already been implemented within the Advanced X-ray Imaging group at UCL, within the fields of biomedical imaging, as well as material science. This has allowed the detection of small scattering signals, which were otherwise invisible to previous retrieval methods, allowing further knowledge to be gained into the ultrastructure of, and damage to, for example, composite materials. By allowing the retrieval of very small scattering signals, which have been shown to be retrievable from biological tissues without known pathology, further information can be gained about the microscopic structure of tissues, and may reveal differences in diseased and healthy tissues, therefore further developing the edge illumination system as a feasible clinical diagnostic tool. Potential diagnostic applications of the system lie within the field of oncology, specifically breast cancer diagnosis, and the sensitivity and specificity of the system with regards to detecting areas of abnormal tissue could be improved by the accurate retrieval of low scattering signals. Finally, the algorithm has been disseminated via open access publication[4], therefore is available to others who wish to utilise the edge illumination system.

Contents

List of Tables

List of Figures

List of Symbols:

μ_s – Optical scattering coefficient

μ'_s – Optical reduced scattering coefficient

μ_a – Optical absorption coefficient

Γ - Grüneisen parameter

n – Refractive index

c – Speed of light

v – Speed

λ – Wavelength

ρ – Particle density

N – Number of particles

V – Volume

σ_a – Absorption cross section

σ_{sc} – Scattering cross section

σ_{tot} – Total cross section

α – Molar absorption coefficient

N_A – Avogadro's constant

C – Concentration

I – Intensity

z – Distance

$\boldsymbol{S}$ – Poynting Vector

A – Surface area

$\hat{\boldsymbol{n}}$ – Surface normal

$\mathbb{S}$ – Arbitrary surface area

$(p(\hat{\mathbf{s}}, \hat{\mathbf{s}}_\mathbf{0}))$ – Scattering phase function

$(f(\hat{\mathbf{s}}, \hat{\mathbf{s}}_\mathbf{0}))$ – Scattering amplitude

$\hat{\mathbf{s}}$ – Scattered unit vector

$\hat{\mathbf{s}}_\mathbf{0}$ – Incident unit vector

Q_{sc} – Scattering efficiency

P – Power

g – Anisotropy factor

r – Radius

δ – Real part of the refractive index (delta)

β – Imaginary part of refractive index (beta)

Φ – Phase shift

r_e – Classical electron radius

ρ_e – Electron density

F – Dilution factor

a, b, c and d – Fitting coefficients for Gaussian retrieval methods

$y_{object}(x)$ – Recorded intensity in each pixel

yic – Recorded intensity for illumination curve

$t_{flat}, r_{flat}, s_{flat}$ – Transmission, refraction and scattering flat field coefficients

$t_{object}, r_{object}, s_{object}$ – Transmission, refraction and scattering sample coefficients

t_0 – Offset coefficient

t_{image} – Retrieved transmission signal

r_{image} – Retrieved refraction signal

s_{image} – Retrieved scattering signal

Overview

This thesis seeks to address the central hypothesis of whether planar dark field x-ray phase contrast imaging (XPCi), or 'x-ray scattering' can be used to quantitatively map or estimate the distribution of optical scattering properties of biological tissues. If a correlation were to be found, then the methods of x-ray scattering retrieval developed within this thesis could be applied to tomographic images to map the 'thickness independent scattering parameter' throughout a tissue volume and therefore estimate the optical scattering. This would enable translation to a clinical or biomedical research setting, where the optical properties of large volumes of tissue within a patient could be accurately defined. Such a map of scattering properties would be useful in addressing the inverse problem in quantitative photoacoustic tomography, where accurate knowledge of optical transport through tissue is required in order to determine the concentration of optically absorbing substances (chromophores) within a tissue volume or an entire patient.

This hypothesis is important as if it were true it would positively impact a range of biomedical imaging techniques such as photoacoustic imaging. Photoacoustic imaging is a promising three-dimensional biomedical imaging technique. It enables functional imaging to be performed, due to the rich optical contrast provided by light absorbing chromophores, whilst maintaining high spatial resolution (down to 50 μm) and penetration depth (up to a few centimetres)[5]. There is currently much interest in performing quantitative, rather than just qualitative imaging, for example measuring the degree of blood oxygenation. Such a measurement is, however, heavily dependent on accurate knowledge of the optical properties of biological tissues, in particular scattering[6,7].

The ability to non-invasively and accurately quantify the reduced scattering coefficient (μ_s') throughout large volumes of tissue would be ground-breaking. Current methods used to quantify the scattering properties of tissue are largely performed on *ex vivo* tissues and are restricted to superficial regions or thin slices or are inaccurate. Optical properties generated by such methods are therefore either unreliable or unable to be translated to *in vivo* tissues.

Edge illumination x-ray phase contrast imaging (EI-XPCi) provides image contrast based on the refraction of x-rays as they traverse a sample[8], with the scattering signal representing refraction from sub pixel structures within a sample. The technique can perform high resolution imaging of large tissue volumes and has the potential to be used on entire small animals, thus allowing optical properties to be determined for individual animals in a specific physiological state at a defined point in time.

An experimental approach was developed to test the central hypothesis, initially using phantoms to allow refinement of the optical and x-ray experimental techniques, enabling the subsequent use of biological tissues. Phantoms with known optical, but unknown x-ray properties were constructed using either silicone, gel wax or agarose as a bulk material. Each bulk material was embedded with scatterers, in the form of either TiO_2 powder or silica microspheres. Manufacturing methods for each of the six bulk material-scatterer combinations were developed and refined in order to allow simultaneous production of both optical and x-ray appropriate phantoms.

The reduced scattering coefficient (μ'_s) of the phantoms was controlled by adding appropriate quantities of scatterer to the bulk material. Once manufactured, the reflectance and transmittance values of the phantoms were determined via the use of a spectrophotometer with integrating sphere. These values were used within the inverse adding doubling program (IAD) to accurately determine the μ'_s of each phantom. To ensure that the phantoms designed were appropriate for continued, long term use, the temporal stability of the optical scattering properties was monitored over a period of approximately 2 years, with significant instability seen within the gel wax phantoms.

The x-ray phantoms were imaged using the edge illumination x-ray phase contrast imaging system at UCL (EI-XPCi), and their scattering properties retrieved. Due to the very low scattering and high absorption of many of the samples, along with the imperfect absorption of the masks in the EI system, existing retrieval methods were unable to accurately determine the scattering properties of the phantoms. A retrieval method was therefore developed to enable the determination of very low scattering signals from highly absorbing samples, subsequently known as the ‘three Gaussian retrieval’ method. This

method is the most sensitive EI-XPCi scatter retrieval method developed to date. The scattering values retrieved by this method demonstrate a linear relationship with the synchrotron analyser-based imaging (ABI) scattering signal, although the reason for this relationship is currently unknown, and should be the subject of future investigations.

Comparison between the optical and x-ray scattering properties of the phantoms did not reveal a correlation, however, it was not possible to determine from this that a correlation between the two properties would not be present in biological tissues. Methods to measure both values in tissues were therefore developed.

The measurement of the optical properties of biological tissues *ex vivo* poses problems due to the difficulty in preparing a thin and uniformly flat sample of each tissue type for measurement within a spectrophotometer, therefore optical coherence tomography (OCT) was investigated as a method for determining the optical scattering properties in such tissues. This was initially investigated via the use of the previously designed phantoms, enabling comparison between the spectrophotometer and OCT obtained values of optical scattering, confirming the accuracy of the data collection method under single scattering conditions. After refinement of the data collection method, the attenuation coefficient (a combination of the scattering and absorption coefficients) of biological tissues was calculated In accordance with previously described analysis methods[9,10].

To determine an x-ray scattering parameter that was independent of the thickness of the sample (much like with the parameters associated with optical scattering), multiple thicknesses of each biological tissue were imaged using EI-XPCi, and the x-ray scattering signal retrieved using the previously developed ‘three Gaussian retrieval’ method. Finally, a comparison of the calculated x-ray and optical scattering values of the biological tissues was performed, revealing no correlation, therefore disproving the hypothesis.

1. Introduction to Photoacoustic Imaging

1.1 History

The photoacoustic effect, or the "photophonic effect" was initially observed by Alexander Graham Bell in 1880. He reported that if pulsed light was shone on a variety of substances[11], then audible sound was produced[12]. He observed that darker coloured objects produced much louder sounds than lighter coloured ones, leading to the conclusion that the sound produced was highly dependent on the amount of light absorbed[11]. Current biomedical photoacoustic imaging techniques are still based on the principles described by Bell in the nineteenth century, exploiting differences in optical absorption by various tissue types to produce differing acoustic (ultrasound) signals. (Figure 1)

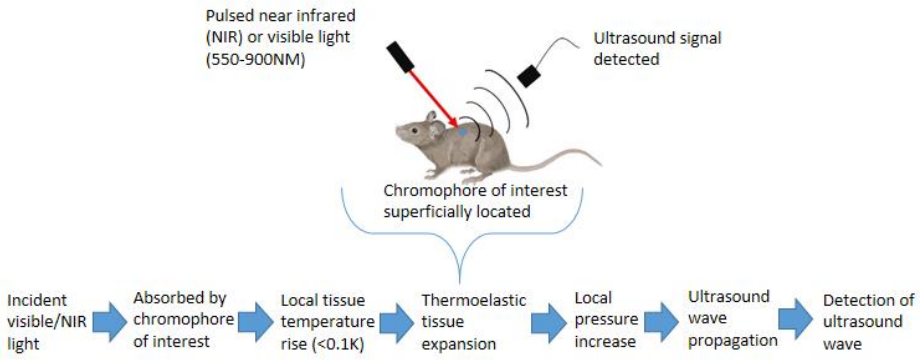

Figure 1. *Principles of photoacoustic imaging.*

The development of the effect into a usable clinical and industrial technique was revived by the development of the laser as a source, and later, by the development of improved detector technology. This enabled detection of signals indiscernible to the human ear. Despite such advances, it wasn't until the mid-1990's that the photoacoustic effect was considered as a potential biomedical imaging modality. This is when it was demonstrated theoretically, and subsequently experimentally, that an ultrasound signal generated by pulsed light could be detectable by medical ultrasonic transducers[13]. Initial studies using tissue mimicking phantoms, revealed that photoacoustic imaging showed promise in medical diagnostic imaging, and even out performed some established imaging methods (x-ray and ultrasound) in breast imaging[14]. Further investigations were initiated to determine whether

this method, be it tomographic or planar, could be used to identify and image human and animal anatomy *in vivo,* with some of the first evidence of the potential of *in vivo* imaging coming from murine models of breast cancer[15].

1.2. Quantitative Photoacoustic Imaging

Photoacoustic imaging achieves rich tissue contrast due to optical absorption by the principal chromophores present within tissue, such as lipids and haemoglobin. Contrast is derived due to differing concentrations of such chromophores throughout tissue and also due to the strong wavelength dependence of each chromophore's absorption spectrum (further discussed in section 2.1.2. Optical Absorption). Furthermore, photoacoustic imaging offers a relatively high spatial resolution, deep in tissue, because the generated ultrasound waves experience very little tissue induced perturbation upon propagation to the ultrasound sensor. The use of photoacoustic imaging is extensive, and *in vivo* applications include visualisation of the peripheral nervous and circulatory systems[16], non-invaisive myoglobin oxygen saturation monitoring[17] and the combination of photoacoustic imaging with optical coherence tomography to image retinal and choroidal vasculature and pigmentation[18].

Further information regarding the concentration of the absorbing chromophores could be gained through quantitative analysis of the received acoustic signal. The differential absorption of light throughout a sample is detected as a time varying acoustic signal, and efforts have been made to translate this received ultrasound signal to quantitative information regarding a chromophore of interest, creating an 'absorption map' of the tissue being imaged. This can be described as the inverse problem of quantitative photoacoustic imaging. This inverse problem can be split into two distinct parts: (1) the acoustic, and (2) the optical inverse problems. The acoustic inverse problem considers how to convert the detected ultrasound signal into the initial pressure increase within the tissue. The optical inverse problem is concerned with determining chromophore concentration from the calculated initial pressure increase, which entails calculating the fluence of excitation light throughout the sample. The acoustic inverse problem has been studied extensively, and although improvements can undoubtedly be made, it has been well addressed[7]. The optical inverse problem has also been studied in detail yet remains unsolved under all but the most ideal of situations.

1.2.1. The Optical Inverse Problem

When considering the optical inverse problem, this can further be subdivided into the following, (1) conversion of the initial pressure distribution caused by thermal expansion of the tissue into the absorbed optical density (i.e., the optical energy that is absorbed by the chromophore of interest), and (2) conversion of the absorbed optical density into the concentration of chromophores. The Grüneisen parameter *(Γ),* is a measure of the photoacoustic efficiency of a tissue, i.e., how well it can convert heat energy into a pressure increase and is used to address the first of these subdivisions. This parameter does vary between tissues and increases linearly with increasing haemoglobin concentration[19], however, this variation is considered insignificant[5]. Regardless of whether the variation in Γ is significant or not, the contrast obtained in photoacoustic imaging can be assumed to be predominantly dependent on the significant differences in optical absorption and scattering within tissue[5]. It is for this reason that the conversion of absorbed optical density to chromophore concentration is currently of most interest.

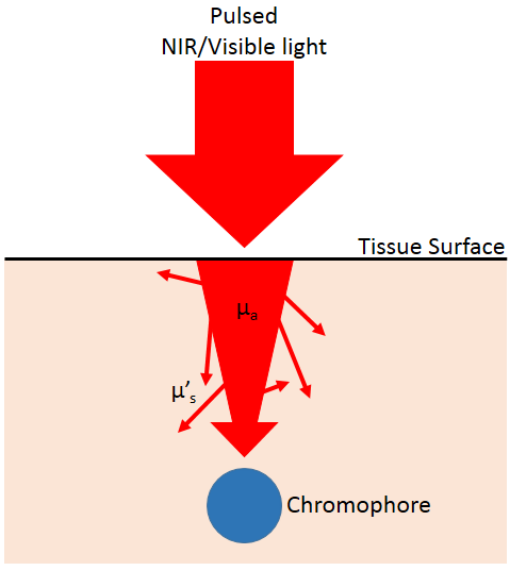

Figure 2. *Factors affecting the absorbed optical density. As the light enters the tissue it is subject to absorption as well as multiple scatter events. This decreases the fluence at the level of the chromophore compared to what was present at the tissue surface.*

Robust models of light transport in tissue that account for the absorption and scattering properties of tissue are required to accurately determine the fluence of light incident on chromophores (Figure 2). The fluence directly influences the absorbed optical density, and therefore accurate knowledge of tissue absorption and scattering distributions are required for photoacoustic imaging to be made quantitative. Multiple models have been adopted to account for light transport in tissue, and multiple approaches to solving the inverse problem have been implemented[6]. However, none of these are applicable in all imaging situations as various assumptions have had to be made to account for the unknown light transport. Accurate knowledge of the scattering properties of a tissue of interest is required to make photoacoustic imaging quantitative, and the measurement of such properties *in vivo* and *ex vivo* is currently unreliable (further discussed in 2.3 Optical properties of biological tissue). Furthermore, whilst estimated reference data is available based on a variety of measurement techniques[20], this data is not able to be used in practice due to wide variations in optical properties of tissue type which occur through any population. Due to the scatter dominant nature of biological tissues, efforts should therefore be focused on determining accurate methods of measuring the scattering properties of such tissues in order to further photoacoustic techniques.

2. Introduction to Optical Properties of Matter

2.1 Optical Interactions in homogeneous materials

2.1.1. Refractive Index

The electric field of an incident wave interacts with electrons contained within the atoms of a material. Consider, in the first instance, a single electron which is accelerated by the incident wave. If the electron were free it would radiate as an oscillating dipole. Since, however, when the electron is bound to an atom it will radiate as a damped oscillating dipole, so long as the frequency of the incident wave is far from resonant frequencies of the damped oscillator. Therefore, the electron can be viewed as an oscillating dipole, oscillating with the same frequency as the incident wave. The oscillating electron thus re-radiates an electric field, i.e. a scattered wave, at the same frequency as its oscillation. This phenomenon known as Thomson scattering is an elastic process as the frequencies, and therefore photon energies, of the incident and scattered waves are identical. When considering an atom with multiple bound electrons, the scattered field is a sum of the scattered fields from all of the electrons within it and when considering a bulk material made up of a finite number of atoms, the field emanating from the material is then a sum of all fields originating from the atoms within[21]. This summation of scattered fields on a bulk material level is the origin of the refractive index and is observed as a perturbation to the wave front that emerges from a material of differing refractive index to its surroundings.

The refractive index (n) of a medium is defined as the ratio of the speed of light in a vacuum to the speed of light in the medium of interest:

$$n = \frac{c}{v} \qquad \textit{Equation 1}$$

Where c is the speed of light in a vacuum and v is the speed of light within the medium. The refractive index can also be expressed in relation to the wavelength of light:

$$n = \frac{\lambda_0}{\lambda} \qquad \textit{Equation 2}$$

Where λ_0 is the wavelength of incident light in a vacuum, and λ is the wavelength of light within the medium. Although the wavelength and speed both change as a wave propagates through an area of fluctuating refractive index, the frequency of the wave within the medium remains equal to that of the incident wave in a vacuum. The gross effect of changing wavelength and speed is that the wave front refracts when the wave is incident upon a material at non-normal incidence. On a macroscopic level, the change in direction encountered by a plane wave as it travels from a medium of refractive index n_0 to a medium of refractive index n_1 (Figure 3) can be described using Snell's law:

$$n_1 \sin\theta_1 = n_0 \sin\theta_0 \qquad \textit{Equation 3}$$

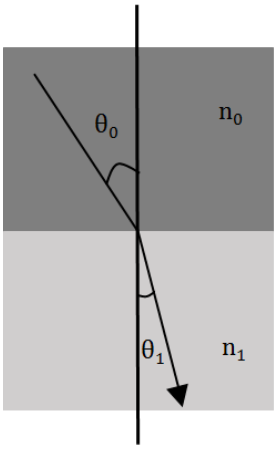

***Figure 3**. Snell's law - a plane wave travels from a medium of refractive index n_0 to a medium of refractive index n_1. θ_0 and θ_1 are the angle of incidence and angle of refraction respectively. In this case $n_1 > n_0$.*

Biological tissues contain refractive index fluctuations, due to the microstructure of each tissue type. Refractive index boundaries therefore do not just occur at gross tissue boundaries, but also exist on a cellular and subcellular level, which means that Snell's law alone, is not enough to describe the propagation of light through a bulk tissue mass. The mean refractive index of the tissue can be obtained *ex vivo* via use of a refractometer, however optical coherence tomography (OCT) has also successfully been used to obtain the mean refractive index of *ex vivo* porcine cranial bone[22] as well as human skin *in vivo*[23]. The refractive index range seen for different tissue types, if the mean of the microscopic variation is considered, often only varies between that of fat and water, 1.5 and 1.33 respectively at 800nm[24].

2.1.2. Optical Absorption

Every molecule has a distinct set of rotational, vibrational and electronic energy levels in which the molecule can exist. The energy required to move between levels of the same classification is smallest for rotational and largest for electronic levels (Figure 4). The differences between energy levels determines the natural frequencies of the molecule. If the frequency of incident light matches that of the natural frequency of the molecule, then a stable transition between energy levels i.e. absorption, can occur.

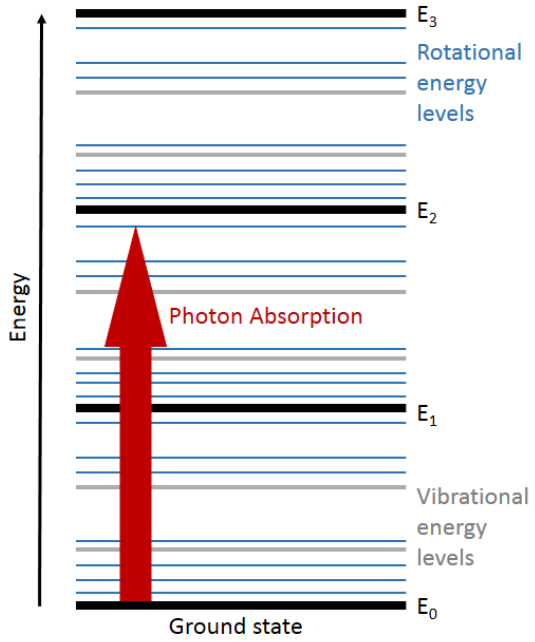

Figure 4. *Energy level diagram showing the rotational (blue), vibrational (grey) and electronic (black) energy levels. An absorption event has been shown between two energy levels i.e. one of the natural frequencies of this diagram.*

Within the visible spectrum, transitions associated with absorption fall within the vibrational and lower electronic energy level transitions. It is the variations in these levels between different molecules that forms the basis of the absorption spectra of complex biological tissues, containing multiple absorbing molecules, known as chromophores. If the frequency of incident light does not match that of one of the natural frequencies of the molecule, then re-radiation of the light, i.e. scattering is much more likely to occur.

2.1.2.1. Absorption coefficient (μ_a)

The absorption coefficient (μ_a) for a collection of identical absorbing particles can be described by:

$$\mu_a = \rho\sigma_a \qquad \textit{Equation 4}$$

Where ρ is the particle density - the ratio between the number of scatterers (N) and the volume that they are found within (V), and σ_a is the absorption cross section. The absorption cross section is a representation of the effective cross-section that a particle has and is a measure of the probability that an absorption interaction will occur.

When considering a collection of identical absorbing molecules, then the absorption coefficient can be defined in terms of the molar absorption coefficient (α). The molar absorption coefficient is the total absorption cross section created by one mole of defined substance. The number of molecules in one mole is known as Avogadro's constant (N_A), and therefore this relationship can be written as:

$$\alpha = N_A\sigma_a \qquad \textit{Equation 5}$$

This can only be used to describe a collection of identical molecules, and therefore is not applicable to biological tissue which is made up of multiple different absorbing substances (chromophores) present at varying concentrations. Therefore, if considering biological tissues, the molar absorption coefficient can be weighted according to concentration of each substance, and then summed. This summation is the absorption coefficient. For example, if considering the chromophores commonly found in skin (HbO_2, Hb and melanin), then the absorption coefficient would be:

$$\mu_a = \alpha_{HbO_2}C_{HbO_2} + \alpha_{Hb}C_{Hb} + \alpha_{melanin}C_{melanin} \qquad \textit{Equation 6}$$

Where C_{HbO2}, C_{Hb} and $C_{melanin}$ are the molar concentrations of HbO_2, Hb and melanin respectively. If considering an arbitrary material with k number of chromophores of various concentrations (C), then μ_a can be expressed as:

$$\mu_a = \sum_{k=1}^{K}\alpha_k C_k \qquad \textit{Equation 7}$$

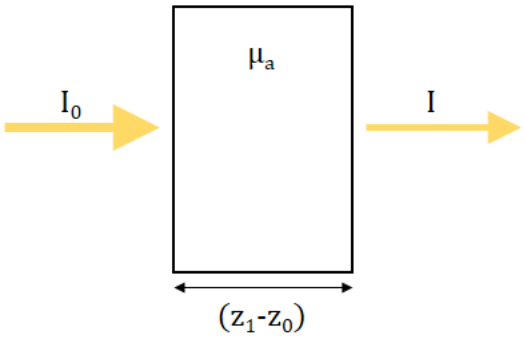

Figure 5. *Basic experimental set up to determine μ_a of a homogeneously absorbing, non-scattering sample, of thickness$(z_1 - z_0)$.*

Consider the situation as depicted in Figure 5, as the beam traverses the sample over the distance$(z_1 - z_0)$, some of the photons will be absorbed from the primary beam, and the intensity of the beam leaving the sample will be reduced. The reduction of intensity over a given value of $(z_1 - z_0)$ will follow an exponential decay such that:

$$\frac{I}{I_0} = e^{-\mu_a(z_1 - z_0)} \qquad \textit{Equation 8}$$

This is known as the Beer-Lambert-Bouguer law. The basic experimental set up shown in Figure 5, along with Equation 8, can be used to measure the absorption spectra of a purely absorbing sample using a spectrophotometer.

The value of μ_a varies non-linearly with wavelength, and each absorbing compound has its own unique absorption spectrum, which describes the absorption over a range of wavelengths.

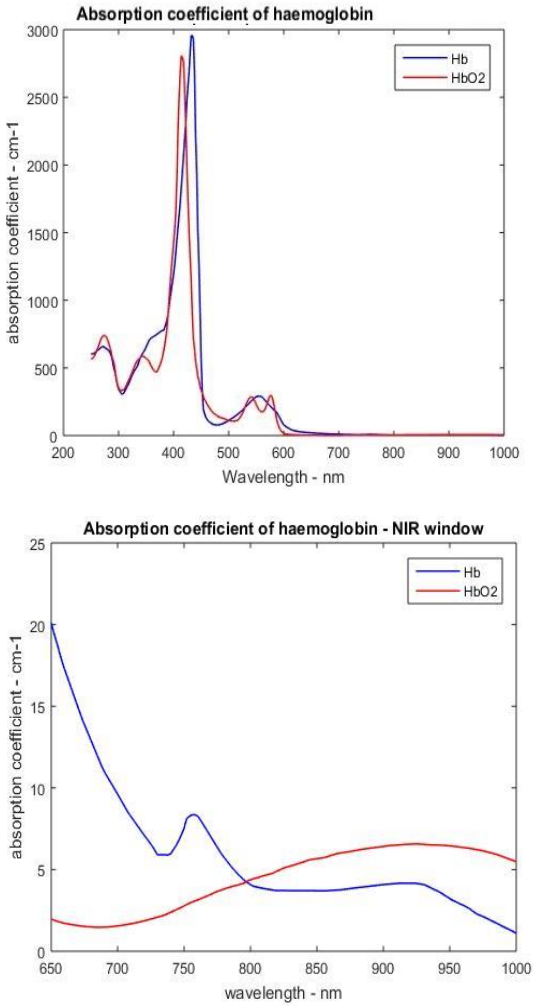

***Figure 6**. Absorption spectra of Hb and HbO_2 in the entire visible (top) and near infra-red (NIR) (bottom) part of the spectrum. Graphs reproduced using data from http://omlc.org/spectra/hemoglobin/summary.html.*

Figure 6 shows the non-linear variation of the absorption coefficient of haemoglobin with wavelength. Haemoglobin is the dominant chromophore within biological tissue and therefore, to increase penetration depth, many optical techniques take advantage of the low absorption displayed by Hb and HbO_2 in the NIR wavelengths (between approximately 650nm to 1350nm), with wavelengths of 800nm or 1300nm commonly used for optical imaging techniques such as in photoacoustic tomography as discussed in section 1.2. Quantitative Photoacoustic Imaging.

2.2 Optical Interactions in Inhomogeneous Materials: Scattering

2.2.1. Poynting Vector

The Poynting vector is defined as the energy flowing through a unit area per unit time. Considering a material of uniform optical properties, in which time harmonic magnetic ($\mathbf{H}$) and electric ($\mathbf{E}$) fields are present, then the time averaged Poynting vector ($\mathbf{S}$) determines the quantity ($|\mathbf{S}|$) and direction ($\mathbf{S}/|\mathbf{S}|$) of energy flowing through a unit area per unit of time (power per unit area).

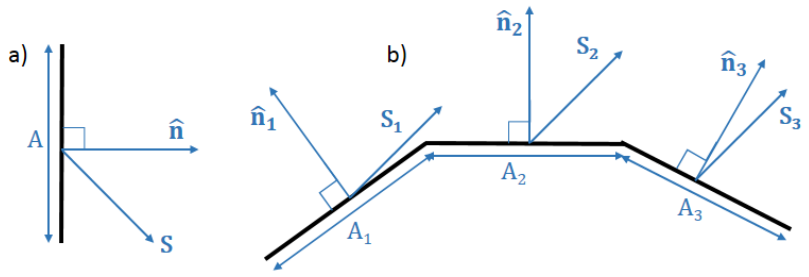

Figure 7. *Parameters associated with measuring the power crossing a) a surface of defined area A, and b) a larger surface made up of multiple smaller units of surface areas A_1, A_2, A_3. $\hat{n}$, $\hat{n}_1$ $\hat{n}_2$ and $\hat{n}_3$ are the surface normals. S_1, S_2 and S_3 are all parallel.*

Considering a surface of area, A, then the total power crossing that area (P) is equal to $A(\mathbf{S} \cdot \hat{\mathbf{n}})$. The power flowing through a surface made up of multiple units of surface area A (Figure 7) is therefore:

$$P = A_1(\hat{\boldsymbol{n}}_1 \cdot \boldsymbol{S}_1) + A_2(\hat{\boldsymbol{n}}_2 \cdot \boldsymbol{S}_2) + A_3(\hat{\boldsymbol{n}}_3 \cdot \boldsymbol{S}_3) \qquad \textit{Equation 9}$$

Finally, if considering measuring the power flowing through an arbitrary surface, such as a detector with surface $\mathbb{S}$, then the total power crossing the surface is:

$$P = \int_{\mathbb{S}} \mathbf{S} \cdot \hat{\mathbf{n}} \, \mathrm{d}A \, . \qquad \textit{Equation 10}$$

2.2.2. Scattering Phase function

The scattering phase function ($p(\hat{\mathbf{s}}, \hat{\mathbf{s}}_0)$) is a probability measure of the distribution of scattered light at each scattering angle when considering a single scattering event. The scattering amplitude($f(\hat{\mathbf{s}}, \hat{\mathbf{s}}_0)$) is the amplitude of

the scattered wave in the direction of the scattered unit vector ($\hat{\mathbf{s}}$) compared to amplitude of the incident plane wave in the direction of the incident unit vector ($\hat{\mathbf{s}}_\mathbf{0}$) and is related to the scattering phase function by the following:

$$p(\hat{\mathbf{s}}, \hat{\mathbf{s}}_\mathbf{0}) = \frac{1}{\sigma_{tot}} |f(\hat{\mathbf{s}}, \hat{\mathbf{s}}_\mathbf{0})|^2 \qquad \textit{Equation 11}$$

Where $\sigma_{tot} = \sigma_a + \sigma_{sc}$, σ_a and σ_{sc} are the absorption and scattering cross sections, respectively. This equation is used to construct scattering diagrams which demonstrate the directionality of scatter, and the probability of a wave being scattered in a specific direction. As this is a probability function, if there are no absorbers or sources present within the volume considered, then the integral of the phase function over all angles in three dimensional space will always equal 1 [25]. The Henyey-Greenstein phase function is considered a good analytic approximation to the phase function of various tissue types, and is therefore used as the standard phase function in the inverse adding-doubling method of optical property retrieval[26].

2.2.3. Scattering Cross Section

The relative power scattered by a particle of arbitrary shape and cross-sectional area A, can be described by the scattering efficiency(Q_{sc}), the ratio between the total scattered power (P_{sc}) and the total incident power (P_{inc}):

$$Q_{sc} = \frac{P_{sc}}{P_{inc}}. \qquad \textit{Equation 12}$$

Using the time averaged Poynting vector, then the total power incident on the particle can be calculated and inserted into Equation 12 giving:

$$Q_{sc} = \frac{P_{sc}}{|\boldsymbol{S}^{\boldsymbol{inc}}| A} \qquad \textit{Equation 13}$$

The parameter that relates the geometric cross section (A) with the scattered energy is termed the scattering cross section (σ_s) and is equal to

$$\sigma_s = \frac{P_{sc}}{|\boldsymbol{S}^{\boldsymbol{inc}}|} = A \cdot Q_{sc} \qquad \textit{Equation 14}$$

The scattering cross section defines the likelihood of a scattering event occurring when an incident field encounters a particle of area A. It is the effective size of the particle compared to its geometrical cross section and demonstrates the particle's effectiveness as a scatterer and is therefore unique to each scattering substance considered. Therefore, a particle which

scatters weakly with a low scattering efficiency (i.e. only scatters a small amount of the incident power) will have a much smaller scattering cross section than one which scatters strongly with a high scattering efficiency[25].

2.2.4. Scattering Coefficient (μ_s)

The scattering coefficient (μ_s) is a measure of the number of scattering events that would occur per unit length, therefore, its units are inverse length. If considering a single scatterer then this scatterer has a scattering cross section (σ_s), which is applicable to scatterers of any shape. When considering a collection of identical scatterers, then the scattering coefficient is approximately equal to the product of the concentration of scatterers with the scattering cross section of a single scatterer:

$$\mu_s = \rho\sigma_s, \qquad \textit{Equation 15}$$

Where ρ is the particle density. This assumes that all scatterers are of the same radius, making it applicable to phantoms made of, for example, microspheres of known diameter and minimal or known size variation.

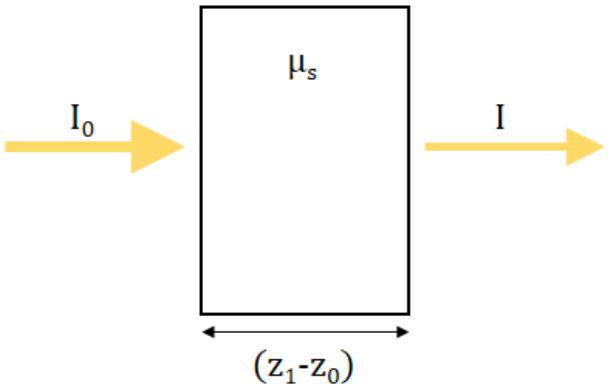

Figure 8. *Basic experimental set up to determine μ_s of a homogeneously scattering, non-absorbing sample, of thickness$(z_1 - z_0)$.*

Consider the example in Figure 8. A homogeneously scattering and non-absorbing sample is irradiated by a collimated beam of light (UV, Visible or IR) of intensity I_0. As that beam traverses the sample over the distance$(z_1 - z_0)$, some of the photons will be scattered away from the line of the primary beam, and the intensity of the beam leaving the sample will be reduced (I). The reduction of intensity over a given value of $(z_1 - z_0)$ will follow an exponential decay such that:

$$\frac{I}{I_0} = e^{-\mu_s(z_1 - z_0)}, \qquad \textit{Equation 16}$$

The value of μ_s is difficult to measure in biological samples, as it requires the preparation of exceptionally thin samples (in the region of 100μm or less), which become fragile, are prone to desiccation, and often not representative of the large tissue bulk they originate from[20]. An added difficulty in obtaining accurate values for μ_s is that the detector must be highly collimated to only record light that is in the line of the primary beam and exclude all scattered photons. If all these conditions are met, then μ_s can be calculated via the equation:

$$\mu_s = \frac{-\ln T}{(z_1 - z_0)} \qquad \textit{Equation 17}$$

Where:

$$T = \frac{I}{I_0} \qquad \textit{Equation 18}$$

However, even if all the above conditions are met, the intensity of light transmitted through the sample (I) is very small, leading to a low signal-to-noise ratio, which decreases further as the thickness of the sample is increased[27].

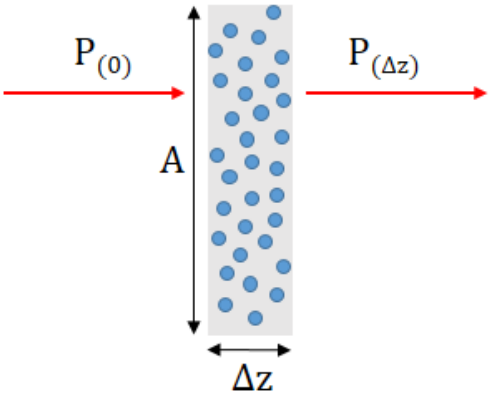

Figure 9. *A sample containing a number (N) spheres within an otherwise homogeneous, non-absorbing medium. The sample has a volume V, thickness Δz and transverse surface area A, such that $V = A\Delta z$. $P_{(0)}$ is the power entering the sample, and $P_{(\Delta z)}$ is the power leaving the sample.*

If the scatterers within a sample are modelled as a group of homogeneously distributed spheres, it can be shown that the total power scattered by the sphere (P_{sc}) for one sphere, is equal to $P_{sc} = \sigma_{sc}|\mathbf{S^{inc}}|$, where $\mathbf{S^{inc}}$ is the time averaged Poynting vector of the incident beam. For a collection of N number of identical spheres within a volume V the total scattered power is:

$$N\sigma_{sc}|\boldsymbol{S^{inc}}| \qquad \textit{Equation 19}$$

When considering a situation as in Figure 9 then the power lost due to scattering over the distance Δz, when $\frac{P_{\Delta z}-P_0}{\Delta z} = {dP}/{\Delta z}$ is:

$$\frac{dP}{\Delta z} = \frac{-N\sigma_{sc}|\boldsymbol{S^{inc}}|}{\Delta z} \qquad \textit{Equation 20}$$

At the limit where $\Delta z = dz$, i.e., it is infinitesimally small and therefore $\mathbf{S}^{inc} \approx \mathbf{S}$, the power ($P$) crossing any surface of area A is defined as $|\mathbf{S}|A$, the volume of the sample $V = Adz$, and the number of spheres per unit volume, i.e. the particle density (ρ) is equal to ${N}/{V}$, therefore:

$$\frac{d|\boldsymbol{S}|}{dz} = -\rho\sigma_{sc}|\boldsymbol{S}| \qquad \textit{Equation 21}$$

Which when solved for a sample of thickness z_1-z_0 gives:

$$S_{(z_1-z_0)} = S_0 e^{-\rho\sigma_{sc}(z_1-z_0)} \qquad \textit{Equation 22}$$

Where $S_{(z_1-z_0)}$ is the power leaving a sample of thickness $(z_1\text{-}z_0)$, and S_0 is the power incident upon the sample at point z_0. The relationship between σ_{sc} and μ_s $(\mu_s = \rho\sigma_s)$ can then be substituted into the above equation to give the well-known Beer-Lambert-Bouguer law, and subsequently the value of μ_s can be found for any given sample of volume V containing N spherical scatterers.

2.2.5. Anisotropy Factor

The anisotropy factor (g) is the average cosine of the scattering angle, and is a measure of directionality of scatter, for example, g = 0, g = -1 and g = 1 represent isotropic, completely backscattered, and completely forward scattered light respectively. The value of g depends on wavelength, with longer wavelengths of incident light demonstrating a greater tendency towards forward scatter within biological tissues[20]. As with all other optical properties thus discussed, the measured value of g varies between authors, however biological tissues exibit a forward scattering value with g often

quoted as 0.9[20]. Use of this value of g for all wavelengths and in all situations should be done with caution, as it can lead to inaccurate μ_s values[28].The refractive indices of extracellular fluid (ECF), cytoplasm and intracellular organelles are approximately 1.35 – 1.36, 1.36-1.375 and 1.38-1.41 respectively[29]. The differences between the refractive indices of biological scattering structures and their surrounding material is small, and it is this, along with the large size of the structures in comparison to the wavelength of light that causes the tissue scatter to be forward in direction[29]. Measurement of g can be difficult, however one method of measurement is goniometry. A collimated laser beam is incident on a tissue sample, and this light is scattered in a variety of directions. An optical fibre bundle is placed at a specific angle from the path of the incident beam (i.e. 0^o would detect the primary unscattered beam), and this relays the scattered light to a detector (a photodiode). The optical fibre, and therefore the detector are then rotated 360^o around the tissue sample, collecting scattered intensity at multiple angles[30]. This gives a measurement of the scattering phase function, which can then be used to calculate g.

2.2.6. Reduced Scattering Coefficient

Reduced scattering coefficient is defined as:

$$\mu_s' = \mu_s(1 - g) \qquad \textit{Equation 23}$$

Where g is the anisotropy factor. The reduced scattering coefficient thus considers not only the scattering power of the sample, but the directionality of scatter, and is much lower than μ_s in biological tissues because of the strong forward scattering nature of tissues.

The stated values of μ'_s for single tissue types vary significantly between authors[20,31], as well as between and within individuals[32], meaning a “look-up table” for this parameter is not viable. The problems with measuring optical properties in biological tissues is discussed further in section 2.3 Optical properties of biological tissue. An estimate of the values of μ'_s for a variety of tissue types can however, be calculated using the following equation, derived by Jacques[20]:

$$\mu_s' = a\left(\frac{\lambda}{500\ (nm)}\right)^{-b} \qquad \textit{Equation 24}$$

Where a is the value of μ_s' at the wavelength of 500nm and b is called the 'scattering power', which is a value that is unique to each different tissue type. The equation and associated parameters were derived from the existing literature values of μ_s', and therefore corresponds to the mean of the experimentally measured values considered by the author. This estimation is valid when the incident wavelength is between 400 and 1300nm, and as long as the tissue is grossly cellular and doesn't contain a high concentration of mitochondria, lysosomes or collagen, all of which produce significant Rayleigh scattering, which is not accounted for here[20]. Typical mean values calculated using the parameters and equations derived by Jacques[20] are shown in Table 1, along with the range of experimental μ_s' values found in the literature that the equation and parameters were derived from.

Tissue Type	μ_s' at 589nm (mm^{-1})	Range of μ_s' at 589nm (mm^{-1})
Skin	3.64	2.56 – 5.68
Fatty Tissue	1.65	0.97 – 2.99
Muscle	0.84	0.62 – 1.12
Breast	1.41	0.75 – 2.03

Table 1. *Typical μ_s' values of common tissue types*[20]

2.2.7. Mie Scattering

Mie scattering describes the scattering of a plane electromagnetic wave by a spherical or cylindrical object, of any size, that has differing refractive index to the material by which it is surrounded, and is therefore commonly used to calculate the scattering coefficient of phantoms consisting of microspheres[25]. Mie theory allows for easy calculation of σ_{sc} in situations where scatterers can be modelled as spheres. Calculators are widely available online to do this, for example, the online "Mie Calculator" developed by Scott Prahl[33]. Mie theory predictions of μ_s for phantoms consisting of epoxy resin and microspheres (diameter 1000nm) were shown to match with values gained experimentally[34], demonstrating the acuracy of the theory in such situations.

Mie theory can be used to describe scattering by larger structures within a tissue, from collagen fibres[35] to the nucleus and the cell itself, both of which contribute heavily to the forward scattering nature of biological tissue[36]. Mie

theory gives a first order approximation of the distribution of scattered light from non-spherical particles[37], however its application to biological tissues may be problematic. By employing Mie theory to model light scattering in tissues, we assume that all tissue can be modeled simply as spheres or cylinders of known diameter and refractive index, suspended in a medium of known refractive index. It should however be noted that although this assumption often holds true, the physiological condition of the tissue being modelled can effect the parameters required in Mie theory calculations, for example, glucose concentration can dynamically effect both the cell (scatterer) size and refractive index[38].

2.2.7.1. Theory

Mie theory can calculate the power scattered by a sphere in any direction relative to that of an incident plane wave. This can then be used in combination with scattering theory to determine the scattering cross section (σ_{sc}) of the individual scatterers.

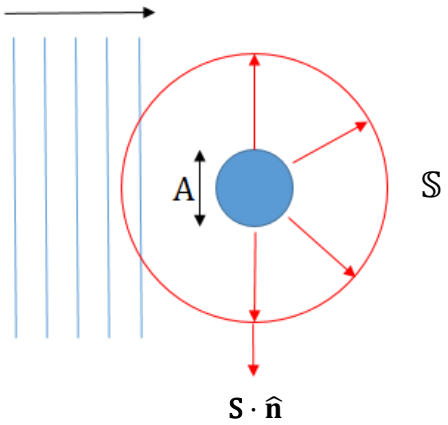

Figure 10. *Plane wave incident on a single spherical scatterer of area A. The red circle indicates a surface area $\mathbb{S}$ around the sphere. $\hat{\mathbf{n}}$ is the surface normal and $\mathbf{S}$ is the poynting vector.*

Considering the situation depicted in Figure 10, and considering a time harmonic field, the total scattered power that propagates in a given direction through the surface of the reference sphere is given by $\mathbf{S} \cdot \hat{\mathbf{n}}$ and can be readily calculated using Mie theory. The time averaged Poynting vector of the scattered light ($\mathbf{S}$), is equal to the amount of power flowing through a unit of area (power per unit area – Wm^{-2}). Therefore, the total power scattered by

the sphere (P_{sc}) over a surface area $\mathbb{S}$ is also analytically calculable from Mie theory and is equal to

$$P_{sc} = \int_{\mathbb{S}} \boldsymbol{S} \cdot \boldsymbol{n}\, dA \qquad \textit{Equation 25}$$

From this Mie theory prediction, the scattering efficiency and scattering cross section of the sphere can be determined as in Equations 12, 13 and 14.

The knowledge of the scattered power from a single sphere, calculated via Mie theory, can then be extended to a collection of spheres within a volume V to obtain the σ_{sc} of the individual spheres, and therefore the μ_s of the sample.

2.2.7.2. Rayleigh Scattering: The Small Particle Limit

Rayleigh scattering was first described and refined by Lord Rayleigh in a series of papers in the late 1800s and describes the scattering that occurs when light interacts with a particle much smaller than its wavelength. In reality, Rayleigh scattering is not a separate entity, but is just the small particle limit of Mie theory. The size that a particle must be to be able to be described by Rayleigh theory is calculated via the equation:

$$x = \frac{2\pi r}{\lambda} \ , \qquad \textit{Equation 26}$$

Where r is the radius of the particle, λ is the wavelength of incident light and x is the size parameter. For Rayleigh scattering to be applicable, we must have x<<1, therefore the particle size will be much smaller than the wavelength of incident light. The size condition dictates that it is most commonly seen due to atoms or molecules within gases, but it is also possible in liquids and solids, including biological tissues. The reduced scattering coefficient (μ'_s) of neonatal skin, has been measured experimentally, with the importance of Rayleigh scattering within tissue samples demonstrated as Mie theory alone was not able to accurately predict the μ'_s value[35]. Small collagen fibrils of diameter much smaller than the incident wavelength, along with other sub cellular structures produce a measured contribution to tissue scattering in accordance with Rayleigh theory[35,39]. Scattering in adult skin can also be modelled with an approximate 10% contribution from Rayleigh, and 90% from Mie theory[35]. The anisotropy

value for Rayleigh scattering is approximated at 0, meaning that scattering is considered to be isotropic. Scattering by these small particles is highly wavelength dependent (~$1/\lambda^4$). This wavelength dependence along with the isotropic nature of scatter means that at shorter wavelengths, the contribution of Rayleigh scattering in many human tissues may act to reduce the anisotropy factor (g) and increase the scattering coefficient from what it would be if scattering were entirely due to larger particles described by Mie theory[39].

2.3 Optical properties of biological tissue

It has been shown that a mixture of spheres of different diameters can accurately replicate scattering in biological tissues, and Mie theory can therefore be used within this context to design and make tissue mimicking phantoms. The correlation between the values measured (for example via spectrophotometry and IAD) and those calculated via Mie theory, is not only dependent on the accuracy of the method used, but also the assumption that the phantoms can be designed and manufactured in such a way that the assumptions of Mie theory can be satisfied. Practically, for biological tissues, the scattering coefficient is experimentally determined rather than theoretically derived (as is done for biological tissues within this thesis), therefore Mie theory is never used in the determination of scattering properties of biological tissues. The focus is therefore on the limitations of the measurement techniques which may be employed to determine μ_s' and g.

There is an extensive history of studies which attempt to determine the accurate scattering and absorption properties of biological tissues, however there is also a wide variation of values obtained, meaning that standard reference values do not exist[20,31,40]. Both *ex vivo* and *in vivo* measurements are subject to potential error, and the ability to determine the optical properties on a sample by sample basis, in a time efficient manner should be the gold standard, especially when properties are required for quantitative analysis such as within the inverse problem of photoacoustic tomography.

2.3.1 Measurement Techniques

2.3.1.1. Spectrophotometer and Inverse Adding Doubling

A common method of determining the optical properties *ex vivo* is via measurement of the collimated transmittance, total transmittance and the total reflectance of a sample using an integrating sphere with a spectrophotometer. A single integrating sphere can be used to measure optical properties *in vivo*, however its use is limited to very thin tissues such as mouse ears which have an approximate thickness of between 310μm and 460μm[41]. A single or double sphere can be used to collect the required data[42], and then the 'Inverse Adding-Doubling' (IAD) method can be applied to calculate the optical properties of the material in question[43]. The IAD method uses the radiative transport equation to solve for μ_s, μ_a and g. IAD finds a solution by comparing the calculated values of transmittance and reflectance with those gained experimentally. If they do not match to within a defined tolerance, the algorithm continues to iteratively solve the equation whilst varying μ_s, μ_a and g until the calculated and experimentally measured values match, thereby determining the optical properties. The IAD program, and handbook which details the optimal experimental parameters are both freely available (http://omlc.org/software/iad/). Using a double integrating sphere to simultaniously obtain total transmittance and reflectance is considered the 'gold standard' as both measurements will be subject to identical illumination and physical conditions, and identical parts of the sample will be considered[44]. This has led to the National Institute of Standards and Technology suggesting this as the universal standard for measuring optical properties in phantoms[44].

2.3.1.2. Optical Coherence Tomography

Optical coherence tomography (OCT) produces images based on the backscatter, or reflection of light from subsurface structures within samples, with the data also used to extract the optical properties of tissues[9,10,45,46]. Initially developed to locate faults in optical fibres and devices[47,48], OCT has now gained widespread clinical application in the field of ophthalmology[49–52], with the Royal College of Ophthalmologists stating that OCT is an "essential requirement for hospital eye services in the UK"[53]. Its use is recommended for the monitoring and diagnosis of glaucoma, and visualisation of the retinal

layers and its vasculature[53], recommendations replicated by the American Academy of Ophthalmology[51].

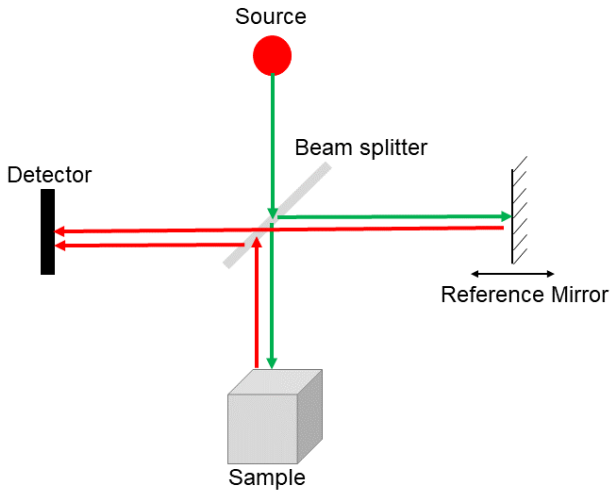

Figure 11. *Basic schematic of interferometer principles used within time domain OCT systems.*

Figure 11 depicts the basic principle behind OCT. Here I consider a so-called time domain OCT system. A broadband source is split at the beam splitter, with part continuing onto the sample (sample arm), and the other part onto the reference mirror (reference arm). In practice, the beam is directed down the two separate paths by a series of fibres[54]. The sample and reference beams are then reflected by either sub surface structures of the sample, or the reference mirror, towards the detector, and the so-called A-scan (i.e., a depth resolved line scan) is generated from the interference pattern created from the combination of the sample and reference beams at the detector. Interference is strongest when the optical distance travelled by light from reference and sample arms is the same due to the low coherence of the light. This principle is exploited in time domain OCT, by axially scanning the reference mirror through a series of distances from the detector (Figure 11). This allows the degree of interference to be measured at multiple sample depths, thus creating a depth profile of sample reflectance, also known as an A-scan. Spectral domain OCT is a much faster technique, that does not involve any moving parts, which can obtain higher resolution images (in the order of microns)[55]. To obtain such images, the position of the reference mirror is fixed, and the detector is replaced with a spectrometer. The spectrometer collects the interference data as a function of wavelength, with a Fourier transform applied to create the A-scan[56]. Multiple A-scans can be

taken to create a cross sectional slice through a sample (B-scan), or a three-dimensional image of a chosen area of a sample (C-scan). The surface of a sample, as well as various sub surface depths of a sample, can be viewed from the reconstructed C-scan, and these slices are known as *en face* images.

The measurement of optical properties, typically the attenuation coefficient (μ_t), from OCT images is based on monitoring the signal decay as a function of depth[9,10,57–59]. The signal decay is a result of both absorption and scattering within the sample, with the attenuation coefficient (μ_t) representing a combination of both properties. Scattering is the dominant interaction in biological tissues, therefore it is often assumed that absorption can be considered negligible, meaning $\mu_t \approx \mu_s$, however, only backscattered light contributes to the OCT signal. Forward scattered light never reaches the detector, effecting the retrieved μ_t and therefore underestimating μ_s. Corrections have been suggested when converting between μ_t and μ_s to account for this undetected scattering[10,60]. OCT provides a suitable method for measuring the optical properties of tissues, as it can measure spatial variations in μ_t without any complex tissue preparation techniques, as with spectrophotometry, which requires very thin samples. As a result, the scattering properties of multiple tissues, such as *ex vivo* lymph nodes[10], ovary[58] and vascular tissues[59] as well as *in vivo* bladder[57], skin[9] and cervix[61] have been determined.

2.3.2. *ex vivo* measurements

As much as possible, tissues should be measured in their 'fresh' state, as freezing, as well as the freeze-thaw process acts to reduce the values of μ_s, μ'_s, μ_a and g[62,63]. Refrigeration also effects the optical properties of tissues with μ_s and μ'_s increasing, and μ_a decreasing after 24 hours[63]. Post mortem tissues undergo autolytic processes including erythrolysis leading to diffuse dispersion of Hb throughout the tissue, as well as the degradation of the extra and intracellular matrices. These changes have been proposed as the reason for the change in absorption and scatter properties respectively[63]. Although changes to μ_s are negligible from those *in vivo* at 5 to 10 minutes post mortem, Hb rapidly deoxygenates creating measurable differences in μ_a of tissue[41]. *Post mortem* changes start within the first hour after euthanasia, and include cellular oedema, clumping of nuclear chromatin and

morphological changes of the mitochondrial inner membrane[64], all of which have the potential to effect optical scattering by effecting the shape or size of the microscopic scatterers. With changes occurring so rapidly post mortem, the measurement of the optical properties of *ex vivo* tissue as a model for *in vivo* tissue is clearly fraught with potential error.

2.3.3. *In vivo* measurements

Despite the potential ethical considerations, and difficulty in obtaining the values, efforts should be focused on improving the measurements of optical properties *in vivo* due to their higher biological relevance. Although *in vivo* measurements will not be prone to the same tissue handling artefacts as those obtained *ex vivo*, it should still be remembered that intrinsic properties of a patient such as their physiological condition[65,66] or the disease state of the tissue[9,61,67–69] have been shown to effect tissue scattering properties. The effect that anaesthesia and surgery itself has on the optical properties of the tissue should also be considered when invasive measurements are taken. Commonly used agents, such as ketamine and isoflurane produce varying degrees of respiratory and cardiovascular depression[70], and therefore have the potential to effect tissue perfusion. This will change the optical properties, thus preventing these measurements being considered as being from "normal" tissue. The superficial and extensive nature of skin makes it the ideal target for *in vivo* imaging, however when repeated measurements of μ_a and μ'_s were made months apart on the same set of participants with the same experimental conditions, an inexplicable variation of approximately 10% was observed[32], showing the importance of patient and time specific optical property determination. Variation of optical properties within a single individual can be used advantageously with regards to *in vivo* physiological monitoring of spatially and temporaly varying molecules. For example, blood glucose levels in diabetics can be non-invasively monitored using optical coherence tomography, where an increase in glucose concentration leads to higher scattering coefficient of the dermis of the skin[65]. Optical properties of multiple tissue types *in vivo* including, cervix[61], prostate[67], colon polyps[68] and brain[71] have been successfully obtained, with only the brain measurements requiring a surgical procedure. The cervical measurements go some way to taking into account the normal inter and intra-subject variations, by performing a 'normalisation' technique on each patient before using the

personalised baseline measurement to help detect abnormal cervical tissues with lower scattering coefficients[61].

3. Introduction to X-ray Properties of Matter

3.1. X-ray Interactions with materials

X-ray photon interactions with matter on a macroscopic level are generally described by three principal types: absorption, scattering and refraction. These interactions occur in different proportions dependent on the energy of the incident photons as well as the composition and structure of the sample undergoing x-ray imaging.

3.1.1. Absorption

Photons undergoing a photoelectric interaction are completely absorbed by the sample, with such interactions being the source of contrast, as well as the most significant contributor to patient dose in absorption based clinical radiography. The photoelectric effect is a low energy phenomenon, and is encountered when an incident photon interacts with, and transfers all its energy to, an inner shell (k shell) electron, enabling it to overcome the k shell binding energy and therefore ejecting it from its orbit. The ejected 'photoelectron' is quickly absorbed by the surrounding material. An electron from an outer shell drops into the k shell void, and in doing so, gives up energy in the form of a photon. The energy of this photon is characteristic of electronic energy levels present within the atom ('characteristic radiation') and is therefore specific to the element of which the sample is made. The chance of a photoelectric interaction occurring is inversely proportional to the cube of the incident energy, and directly proportional to the cube of the atomic number, therefore, as we cannot control the composition of a patient, using higher kVp techniques will act to reduce the patient dose[72].

3.1.2. Scattering

Scattering in its most general form is, as in the optical wavelengths, a deviation of a photon from its original path. Within the energy range used for medical imaging, approximately 20-150KeV, x-ray scattering can be either elastic (Thomson and Rayleigh) or in-elastic (Compton), with the latter occurring more frequently.

To remove ambiguity, from hereon in the terms 'elastic scattering' and 'inelastic scattering' shall refer to the interaction of a photon with an electron (or electrons) which perturbs the trajectory and/or energy of the photon.

However, the terms ‘x-ray scattering signal’ and ‘x-ray scattering’ shall refer to the detected signal caused by elastic and inelastic scattering, usually attributable to subpixel features within a sample.

3.1.2.1. Elastic Scattering

Thomson scattering within the x-ray wavelengths occurs in the same way as in the optical wavelengths (2.1.1. Refractive Index), with Rayleigh scattering being the sum of the scattered fields due to all electrons within an atom. Elastically scattered photons can reach the detector due to the maintenance of their incident energy and therefore lack of dose deposition, therefore, are able to contribute to noise. However, Rayleigh scattering is of little importance in traditional absorption imaging, as very few photons undergo this type of interaction at diagnostic wavelengths, however elastic scattering events do form the basis of x-ray investigations into material structure, such as x-ray crystallography[73]

3.1.2.2. Inelastic Scattering

Compton scattering also occurs due to the interaction of an x-ray photon with an electron of an atom, however this time the photon loses a proportion of its energy, as opposed to a photoelectric interaction, which is where a photon is completely absorbed during the electronic interaction. Furthermore, the energies involved in the two interactions are different, with the photoelectric effect a low-energy phenomenon, and Compton scattering, a mid-energy phenomenon, where the incident photon energy is greater than the electronic binding energy. An incident photon interacts with an electron, which is ejected from its orbit when a proportion of the photon energy is transferred to it. The photon energy is now equal to the incident energy minus what was transferred to the free electron, and the direction in which it now propagates depends on both the incident energy, and the energy retained by the photon. Photons maintaining a higher proportion of their incident energy will be scattered at much smaller angles than those maintaining a lower proportion, which can be scattered at angles up to 180^{o} [72]. Photons scattered in a forward direction with enough retained energy have the potential to reach the detector and are a source of noise.

3.1.3. Refraction

X-ray refraction is the same as optical refraction, i.e., a change in direction of a wave, due to a delayed or advanced wave front. As with optical refraction, x-ray refraction occurs due to differences in refractive index at material boundaries, however the angles of refraction encountered for x-rays are much smaller, within the micro radian range[8].

3.1.3.1. Refractive Index and Scattering

Refraction and elastic scattering are closely related, and this can be seen when considering the complex refractive index (n):

$$n = 1 - \delta + i\beta \qquad \textit{Equation 27}$$

The values of β and δ are related to the absorption and phase properties of a material respectively, and combined, make up the imaginary and real portions of the refractive index, thus determining the path in which a wave travels through any material with known distribution of δ (Figure 12) [8,74].

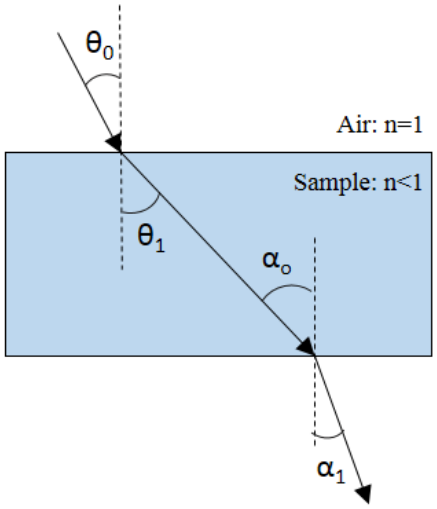

Figure 12. *Refraction of an x-ray wave when travelling through a sample (n<1), in air (n=1). $\theta_0 < \theta_1$ and $\alpha_0 < \alpha_1$. The wave front is advanced as it travels into a material, (phase velocity (v) is $v > c$) from air ($v = c$).*

As within the optical wavelengths, elastic scattering from an atom can be considered the sum of the scattered fields from the electrons within it, and the sum of the fields originating from within each atom of a material gives the scattered field emanating from a bulk material[21]. It is this sum of scattered

fields that is the origin of the refractive index, and therefore the change in direction of the wave front as it travels from a material of one refractive index to another. The refraction angle (α) and phase shift are closely related, and the refraction angle is the first derivative of the phase shift[8]:

$$\alpha = \frac{\lambda}{2\pi}\nabla_{x,y}\Phi \qquad \textit{Equation 28}$$

where[75]

$$\Phi = \frac{\lambda}{2\pi}\int_{z_0}^{z_1} n(x,y)dy \qquad \textit{Equation 29}$$

The phase shift (Φ) caused by elastic scattering is due to the presence of δ (represented in n - Equation 27) in an object of thickness (z_1-z_0). The value of δ is therefore directly proportional to the electron density (ρ_e) of a material and varies with the wavelength (λ) of the incident wave. This relationship is valid when the photons have energy far from the material absorption edges:

$$\delta = \frac{r_e \rho_e \lambda^2}{2\pi}. \qquad \textit{Equation 30}$$

Where r_e is the classical electron radius.

The value of δ is typically in the region of 1x10^{-6}, and therefore n is always less than, but close to 1 for x-rays. Using $v = \frac{c}{n}$, where n < 1, the phase velocity of an x-ray wave travelling through any medium is greater than the speed of light in a vacuum (c). It should be noted however that relativity is not violated, as the group velocity remains less than c. This increase in velocity causes an advancement of the wave front as it enters a sample (n<1) from a vacuum (n=1), and a delay of the wave front as it leaves the sample and re-enters the surrounding vacuum again (Figure 12). The resulting refraction event therefore occurs in the opposite direction to what would be expected for optical wavelengths where materials generally have a real part of refractive index greater than 1. The change in direction caused by gradients in refractive index, and ultimately δ can be exploited, and refraction forms the basis of the 'phase contrast' seen in the edge illumination x-ray phase contrast (EI-XPCi) method adopted at UCL, however other interferometry-based methods are also able to create images directly related to the sample induced phase change.

4. Introduction to X-ray Phase Contrast Imaging

Conventional attenuation based x-ray images are formed due to the variation in β of different biological tissues, with contrast generation due to photoelectric absorption[72]. The value of β is equal to $\mu_a\lambda/4\pi$, with μ_a equal to the linear absorption coefficient[74]. The intensity (I) of the beam that is transmitted through a homogeneous sample of thickness (z_1-z_0) follows an exponential relationship:

$$I = I_0 e^{-\mu_a(z_1 - z_0)}, \qquad \textit{Equation 31}$$

Where I_0 is the incident intensity. Absorption has been exploited to produce diagnostic x-ray images since their discovery by Röntgen in the late 19th century, who used his newly discovered 'x-rays' to create an absorption image of a human hand[76]. Röntgen observed that x-rays were capable of undergoing absorption and scatter, however he was uncertain of their ability to undergo refraction, observing "a possible deviation"[76]. We now know that X-rays do undergo refraction, however due to the very small angles of deflection it would have been impossible for Röntgen to observe this using the equipment available at the time.

As previously discussed, refraction and absorption by a material of thickness (z_1-z_0) are associated with a phase shift (related to δ), and a decrease in the amplitude (related to β) of the wave, respectively. The value of δ is, in general, three orders of magnitude greater than β when considering energies and materials consistent with medical diagnostic imaging, and therefore the contrast generated by differences in δ may be expected to be greater than the contrast generated by differences in β[8], however techniques different to those currently employed for diagnostic imaging must be adopted in order to observe these phase effects. The phase effects are observed generally either via the use of interferometry or the use of structured illumination to enable refraction to be observed.[8]

4.1 Imaging Methods

Multiple imaging methods have been developed, which enable visualisation of sample induced phase and refraction effects (crystal based interferometry and grating interferometry, analyser based imaging, free space propagation and edge illumination), details of which have been extensively reported[8,74].

Analyser based imaging (ABI) shall briefly be discussed due to its use within this body of work, however the focus shall remain on the edge illumination technique. Other techniques shall not be discussed here.

4.1.1. Analyser Based Imaging (ABI)

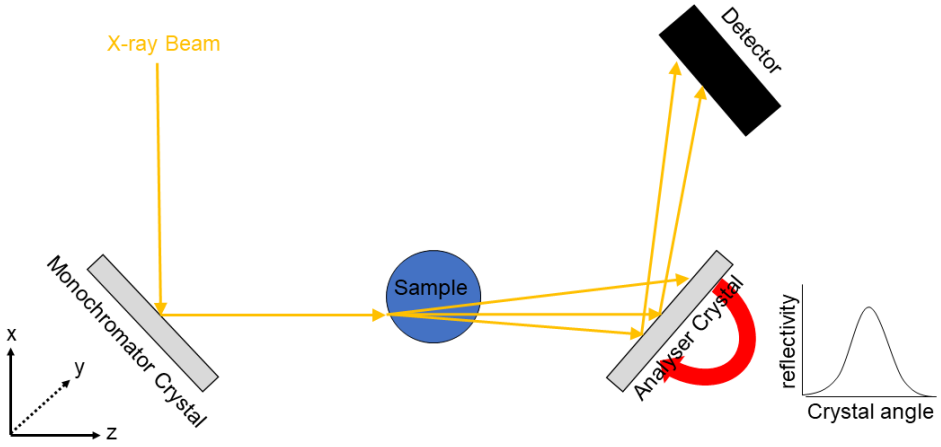

Figure 13. *Schematic (not to scale) of ABI system along with sample rocking curve, created by rotating ('rocking') the analyser crystal about its Bragg angle, and recording the intensity at the detector. To obtain a full image of the sample, it must be translated through the system in the y direction. The beam is normally sufficiently wide in the x direction to cover the sample.*

A typical ABI system is depicted in Figure 13. Due to the system's requirement for a highly collimated monochromatic beam, a monochromator crystal is used to select a beam energy from the potentially broadband synchrotron radiation. Translation to a laboratory source is possible, however after the monochromator, the flux will be significantly reduced, therefore increasing the experimental exposure times. For example, if a 4 minute exposure is required, a total imaging time of 1 hour is required to obtain articular cartilage images at 15 analyser crystal angles[77]. The so-called rocking curve (RC) is unique to the system and represents the reflectivity of the crystal when positioned at different angles, with the maximum reflectivity obtained at the Bragg angle. The RC is created by obtaining images as the analyser crystal is rotated about the y axis in Figure 13 without a sample in place, and commonly has a FWHM in the region of microradians[78]. The RC represents the range of angles that will be reflected by the analyser crystal

towards the detector, and the intensity or probability in which the reflection occurs. Due to the narrow width of the RC, x-rays refracted by a sample away from the path of the primary beam at large angles have a low probability of being reflected by the crystal and therefore will not contribute to the final signal, but will instead be attributed to absorption by the sample[8,78]. To increase the sensitivity of the system to sample induced refraction, the analyser crystal can be positioned at an angle away from the point of maximum reflectivity. Maximum sensitivity can be obtained by positioning the crystal at the angle corresponding to the points, on either side of the RC, where the magnitude of the RC slope is maximised. This ensures that small changes in beam direction will result in dramatically reduced or elevated reflectivity[8]. This has been utilized in pre-clinical synchrotron mammography, where positioning the crystal at 50% reflectivity showed improved contrast compared to standard mammographic techniques[79].

Single images obtained via ABI are composed of a combination of absorption, refraction and scattering caused by the sample[78], which serve to reduce the amplitude, shift the position of the peak, and broaden the RC, commonly approximated by a Gaussian. Multiple methods have been employed to enable separation of each of the image components, with initial efforts focused only on the refraction and absorption signals by taking images at two symmetrical angles about the Bragg angle on the rocking curve[80]. Subsequent retrieval methods were developed, allowing all three signal components to be separated[81–85], requiring multiple images to be taken over the entire angular width of the rocking curve, thus yielding further information about the sample. As well as mammographic examination, ABI has also found use in imaging cartilage[77,86], uterine leiomyomas[87], eyes[88], liver[89] and lungs[90], to name but a few[78].

4.1.2. Edge Illumination (EI)

The edge illumination (EI) method of x-ray phase contrast imaging was initially developed by Olivo et. al. for a synchrotron source and a detector composed of a single row of pixels[91]. It is sensitive not to the phase changes, but the related refraction event, and provides increased image quality and contrast (differential phase contrast) compared to conventional absorption images, initially demonstrated using a standard mammographic phantom[91]. By blocking part of the detector pixel, sensitive and insensitive pixel areas

were created, meaning the system was able to detect very small refraction induced deviations of the beam[91]. Although initially developed for synchrotron sources, the method was successfully translated to polychromatic, non-microfocal, and divergent conventional sources with finite focal spot sizes, demonstrating its ability to operate under relaxed coherence requirements[92].

4.1.2.1. System

The laboratory system is depicted in Figure 14 (not to scale) along with a typical signal gained. The sample mask is used to create an array of 'beamlets' and may be misaligned with respect to the detector mask, which is aligned with the detector pixels. The misalignment between the sample and detector mask means that only part of the incident beamlet reaches the detector whilst the other part is absorbed by the detector mask, therefore the refraction signal is created by the deflection of photons onto (positive signal) or away from (negative signal) the pixel's sensitive surface when a sample is placed between the two masks for imaging. Both masks are identical, however the size of the detector mask is magnified to account for beam divergence[92]. If the sample remains static within the system, then the resulting image is a two-dimensional, projection image as in conventional radiography. Alternatively, if three-dimensional images are required, as in computed tomography, the sample can be rotated around the y axis in Figure 14, obtaining projection images at multiple rotation angles, whilst the source, masks and detector all remain static[93]. By incrementally scanning the sample mask through a number of sub-pitch steps (sample mask positions) in relation to the static detector mask, without a sample in place, and recording the integrated intensity detected by each pixel, the so called illumination curve (IC) can be measured[94]. The illumination curve is unique to each system set up.

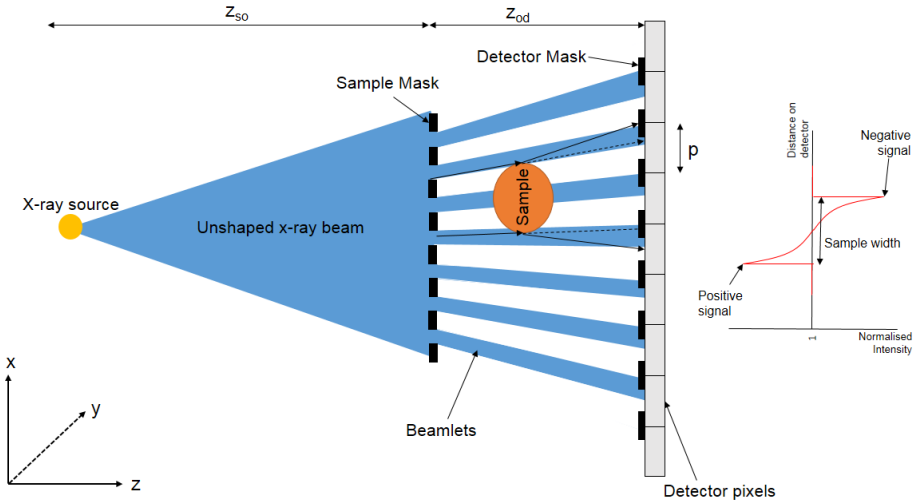

Figure 14. *XPCi - EI set up with a sample in place (left) along with the generated signal (right). The dashed lines show the path the x-ray beam would have taken if the sample had not been in place and the solid lines show the refracted path that the x-ray beam will take with the sample in place.* z_{so} *is the source to sample mask distance,* z_{od} *is the sample mask to detector distance and p is the pixel size. This demonstrates the creation of both a negative and positive signal* [95]*. The intensity at the detector is normalised to a region external to the sample, therefore the background is scaled to 1.*

The EI system as shown in Figure 14 is sensitive to nano-radian refraction angles, and this excellent angular sensitivity has been demonstrated at both high and low beam energies at synchrotron facilities[96] as well as with spatially and temporally incoherent laboratory sources[97]. During image acquisition the sample may be moved by several sub-pitch increments, known as 'dithering'. This increases the spatial resolution, which would otherwise depend on the sample mask aperture size, detector PSF and source focal spot size[98,99]. Although the system depicted in Figure 14 provides excellent angular resolution, it is only able to detect refraction in the x direction, however with use of two-dimensionally 'L-shaped' apertures for both the sample and detector masks, refraction can be detected in both the x and y directions[100] without the necessity to rotate the sample 90°.

4.1.2.2. Signal Retrieval

Images at multiple different illumination fractions can be taken for retrieval of the absorption, refraction[94,96,97,101] and scattering signals[102] of a sample. These images can be used to determine the sample induced changes to the beam profile (typically modelled as a single Gaussian –'one Gaussian' method), the reduction of amplitude due to absorption, shift in the centre point due to refraction, and broadening due to scattering (Figure 15). If information about the individual signal components is not required, then a 'single shot', non-retrieved image still offers an improvement in contrast at clinically acceptable doses compared to standard mammographic techniques[103]. With some modification to the standard EI set up, single shot retrieval of all three signal components can be achieved with laboratory sources[104]. Further to this, a 'phase map' of a sample can be obtained from a single image acquired using the EI principle at a synchrotron source[105], although translation to the laboratory set up has not been made for this method. The phase and refraction signals offer complimentary sample information, and these 'single shot' methods go some way to increasing the clinical viability of this method by reducing acquisition time and delivered dose.

4.1.2.3. Dark Field Imaging

As well as refraction caused by macroscopic sample features, refraction is also caused by microscopic, sub-pixel features within a sample. These features are non-resolvable, however the refraction caused by them contains useful information about the microscopic structure of an object. This signal is known as the x-ray scattering signal, and can be retrieved using the XPCi-EI system[102,106,107]. The signal is observed as a broadening of the beamlet created by the sample mask, and therefore of the IC observed in each pixel[102,108], with retrieval of the signal focused on monitoring this broadening[102,104,106].

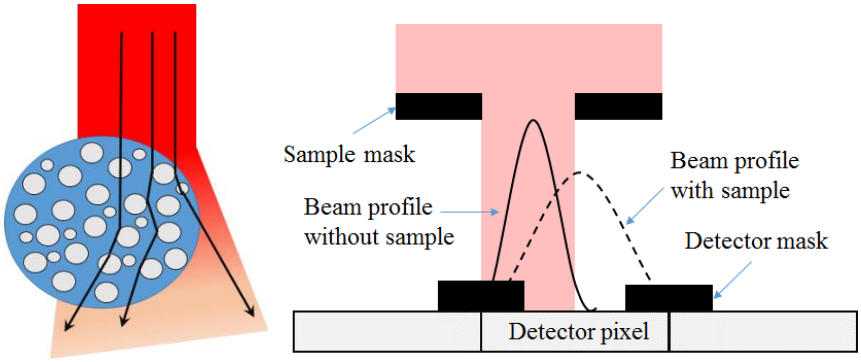

Figure 15. *Left – sub-pixel inhomogeneity causing refraction events leading to a broadened beam - scatter signal. The attenuation and refraction signal are also depicted. Right - The beam profile is "shifted" due to refraction at the edges of the sample, attenuated due to sample absorption, and broadened due to scatter.*

To retrieve this additional structural information about a sample via the 'one Gaussian' method, images must be taken at a minimum of three points on the illumination curve, one at maximum illumination, and the others at equal points on the left and right slopes of the illumination curve[102,106]. True 'dark field' imaging is an alternative approach to obtaining an image based on the scattering properties of a sample. In this case the sample and detector masks are completely misaligned, so the beamlet falls entirely on the absorbing parts of the detector mask[91].The raw image obtained from this set up is purely of the x-ray scattering properties of the sample, however this relies on the assumption that the primary beam is entirely absorbed by the fully absorbing masks. This has been proven not to be true due to the non-zero intensity value obtained when the masks are misaligned as described[106], despite masks being designed to be 98% absorbing at 40keV. Although true dark field imaging is a 'one-shot' scattering technique, obtaining a minimum of three images is preferential due to the ability to simultaneously retrieve refraction, absorption and x-ray scattering images from the same data set.

The x-ray scatter signal gained from the 'one Gaussian' approach is able to provide complimentary diagnostic information in mammographic examinations[102]. Even further information from the subpixel properties of the sample can be gained by increasing the number of images taken to 32, enabling the "moments of scattering distribution" to be retrieved. These have been used to differentiate between normal and emphysematous lung tissue[107], although this application requires further investigation due to low

sample numbers, preliminary results are promising. Thus far, the scattering signal has only been investigated in samples where the scattering Is unable to be controlled such as paper[102,106], breast calcifications[102], composite materials[109] and alveolar tissues[107], therefore the assessment of the quantitative capabilities of the system has yet to be evaluated. As well as biomedical applications, the x-ray scatter signal is also of great interest for security screening[110] and non-destructive testing of composite materials[109]. Finally, microbubbles provide excellent scatter contrast[111]. Microbubbles could therefore be used as exogenous contrast agents to enhance the intrinsic scattering signal of biological tissues, a concept that is already exploited with absorption-based contrast agents: barium and iodine.

5. Introduction to Biomedical Phantoms

5.1. Overview

Phantoms are objects with controllable physical properties which can be used within imaging systems to evaluate and optimise performance. They are usually designed to mimic the properties of biological tissues and should be stable and reproducible, and therefore produce more consistent and predictable results than a living patient.

5.2. Scatterers

Many different scattering particles are commercially available and have been used within phantoms[112,113]. The commonly employed particles are: lipids, microspheres and TiO_2 or Al_2O_3 powders, all of which vary in stability, uniformity and cost, and have all been used with success in a variety of phantoms for different optical applications

5.2.1. Lipid

Milk is widely available at a nominal cost and can be used as a scatterer within phantoms. The lipid component is found as stable, non-coalescing 'globules'[114]. It is these globules that are the scattering particles within bovine milk, along with (and to a lesser extent) the much smaller casein micelles[115]. The refractive index of the globules and casein micelles has been reported as 1.461 at 589nm and 1.570 +/- 0.006 at 600nm respectively[116,117]. Commercially available UHT and pasteurised milk demonstrates a variation in lipid globule size, with the average falling below 1μm for all commercially bought varieties[118], therefore milk does not offer a uniform or controllable particle size distribution, and as well as its well-known limited shelf life, precludes its use in many phantoms

Over time, milk has been replaced with commercially available intravenous lipid emulsions, arguably the most common scatterer used in optical phantoms. Intralipid®, Liposyn™ and Neutralipid™ are all available brands whose use is interchangeable in both intravenous feeding and phantom preparation. Intralipid (Fresenius Kabi Ltd.) is widely available as a 10%, 20% or 30% fat emulsion. The value of μ_a is negligible for all visible wavelengths for stock solution of Intralipid® 10%[119,120], and can therefore be treated purely

as a forward scattering medium (g is between 0.8 and 0.9)[119]. The scattering particles within such lipid emulsions are triglyceride containing fat globules with mean globule size of 0.33µm in 10% and 0.37µm in 30% formulations, both with a standard deviation of no more than 1.3%[121]. Despite the reasonable stability in globule diameter across batches, a small variation of the optical properties between studies, and therefore batches, has been demonstrated[119,120,122], indicating the importance of determining the optical properties of each container prior to use[123]. The optical properties of each batch however remains stable over a period of approximately 2 years, with the inference that stability occurs up to 10 years[122].

Although very commonly used, the use of Intralipid® is not without problems, as it demonstrates fluorescence between wavelengths of 360 and 650nm with two peaks: the first at 450nm and the second at 500nm when an excitation wavelength of 355nm is used[124]. Further to this, Intralipid® has a relative density of 0.988 compared to water[122,125], therefore when left undisturbed, the fat droplets rise to the surface, creating a surface layer which increases in thickness tenfold after an hour[126]. Finally the high lipid content can provide an excellent medium in which mould can form, and this can been seen within a few days of phantom manufacture[24]. Despite its limitations, Intralipid® has been successfully incorporated into a variety of bulk materials such as epoxy resin[127], fibrin[128], gelatin[129] and can also be used in its native liquid form[130].

5.2.2. Inorganic Powders

Both TiO_2 and Al_2O_3 are widely available due to their use as the main pigments in white paint. The particle diameter and size range vary between manufacturers (diameters in the region of 10s to 1000s of nm), so choice can be tailored to suit phantom requirements. The particles are often not spherical, have a variable size and shape distribution[131] and demonstrate rough surfaces when viewed via scanning electron microscopy[132]. Both TiO_2 and Al_2O_3 powders provide a highly stable source of scattering which does not degrade over time or with heating, and all the while the samples are stirred adequately to prevent flow marks and clumping, scattering within the final phantom will be homogeneous[132], however even with careful stirring, sedimentation of powder may still occur[133]. TiO_2 powders have a very high refractive index compared to biological tissues, between approximately 2.6

to 2.9 at 589nm[134], therefore the use of Al_2O_3 with its refractive index of approximately 1.76 at 589nm[135,136] may be more appropriate for tissue mimicking phantoms. The high refractive index of TiO_2 particles also limits the value of g that can be obtained, with a maximum of 0.7 being obtainable for an epoxy resin based phantom of particle size 0.7µm[137]. Al_2O_3 powders of particle size 1µm, can obtain a much more "tissue like" value of g, with 0.97 being obtained when combined with epoxy resin[137].

5.2.3. Microspheres

Microspheres are available in a variety of materials and a range of sizes from the submicron to tens of microns in diameter. Commonly used microspheres include the polymer type: polystyrene or poly (methyl methacrylate) (PMMA), and silica (silicon dioxide - SiO_2). Their highly controllable size of minimal variation and known refractive index means they can be modelled accurately using Mie theory[25] to produce phantoms with known scattering properties. Furthermore, the refractive index of available spheres is similar to that of biological tissues, with n=1.49, 1.59 and 1.46 at 589nm for PMMA[138], polystyrene[139] and silica[140] respectively. Despite offering highly controllable scattering, the use of microspheres is not without problems. When an excitation wavelength of 355nm is used, polystyrene microspheres fluoresce between the wavelength range of 360-650nm[124], although this is with three times less intensity than Intralipid®. Particle aggregation is a significant problem and has the potential to make theoretical predictions of μ_s less accurate by creating spatially varying sphere concentrations within one phantom. Hydrophobic interactions and electrostatic forces are the main cause of sphere aggregation in polymeric and silica spheres respectively[141]. These interactions can be a significant challenge to overcome when preparing phantoms, with aggregation increasing with decreasing sphere diameter, increased temperature, increased sphere concentration, and in the presence of buffer salts[141]. Methods for reducing aggregation that are commonly employed during phantom manufacture are stirring[34] or sonication[131,142,143], however these can be used successfully in combination. Vortexing, vigorous pipetting or grinding with a pestle and mortar have also been recommended for silica microspheres[141].The main barrier to the widespread use of microspheres in phantom studies is their high cost per unit mass. Despite this, they have been successfully incorporated into a range of matrix materials. Polystyrene spheres have been used within epoxy

resin[143], PVA slime[24], gelatine[144] agarose and in aqueous suspension[145]. Although not as commonly used, silica spheres have similarly been successfully incorporated within silicone[131,142,146], and epoxy resin[34] matrices.

5.3. Bulk Materials

The bulk material is generally the main component by volume of any phantom and is the vehicle in which scatterers and absorbers are contained. Common choices for bulk materials include the aqueous solutions - water or saline, hydrogels - gelatine and agar, resins - polyurethane, epoxy and polyester, silicone rubber and polyvinyl alcohol, as well as novel materials such as gel wax. With such a wide variety of different materials available, choice is highly dependent on the properties of the bulk material itself, not only its optical properties (n, μ_s, μ_a), but also its mechanical and chemical properties.

5.3.1. Aqueous Phantoms

Arguably the simplest of all the phantom materials, the use of water or saline with added scatterers or absorbers is cheap. The scattering and absorption properties can be altered with both biological materials such as Intralipid®[126,147] or human erythrocytes[147], and synthetic materials such as India Ink[125,148], microspheres[130] or Cresyl Blue[149], making the process of mimicking tissue (for example the neonatal brain[147]), relatively trivial. Aqueous phantoms can also be used for dynamic studies due to the ability to add various substrates during the experimental procedure. For example, the oxygenation status of human erythrocytes can be altered via the addition of either yeast or oxygen allowing the dynamic study of both deoxygenated or oxygenated states respectively[147]. Despite the flexibility offered by aqueous phantoms, there are disadvantages which often preclude their use. Water has its own intrinsic optical properties, and the absorption spectra of water should be considered when designing phantoms as it is a significant source of absorption through the longer wavelength visible and NIR, as well as the ultraviolet regions of the spectrum. At visible wavelengths below 700nm it can, however, be considered negligible[112]. Liquid phantoms are not stable as the scattering and absorbing particles can freely move within the system whereby causing the phantoms to become heterogeneous over time, due to migration of the particles. Ideally phantoms would be stirred throughout any measurement procedures to ensure homogeneity is maintained[147]. Finally, aqueous phantoms cannot exist on their own. They

must be placed within a container and the addition of a container-phantom interface may introduce errors into measurements, therefore novel containers designed for specific purposes have been created to house liquid phantoms to try to minimise the effect of such an interface on any measurements[147,149]

5.3.2. Silicone

Silicone rubber is a hydrophobic inorganic-organic polymer molecule which consists of atoms of silicon (Si), carbon (C), Hydrogen (H) and Oxygen (O) arranged in a branched chain structure. The backbone of the molecule consists of a repeating Si-O unit, with organic groups attached to the Si atoms within the chain[150]. The most commonly encountered silicone is polydimethylsiloxane, whose structure is depicted in Figure 16. The organic group in this case is the alkyl - methyl (CH_3).

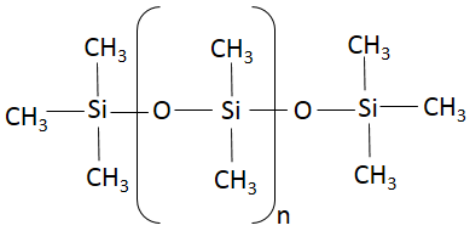

Figure 16. *Polydimethylsiloxane - repeating Si-O backbone with the alkyl group, methyl, attached to the Si within the structure. The $SiO(CH_3)_2$ unit is repeated n times.*

Silicone is available from a variety of sources, however the 2 part, room temperature vulcanising, addition-curing silicone rubber is most commonly used as a phantom material[131,133,146,151]. For such addition curing silicones, the final cured silicone rubber is produced by mixing a cross linker and the polymer, with a catalyst, in a suitable ratio. The mixture can cure at room temperature, however the curing time is significantly decreased by heating the sample.

Silicone rubber is highly versatile, and ideal for phantom manufacture due to its long shelf life and stability as well as its ability to be moulded to any complex or biologically mimicking shape, for example the tracheobronchial tree[152] and textured skin phantoms[142]. The use of silicone is especially useful when simulating skin as it is able to reproduce not only the optical properties

and surface roughness[142], but also the electrical, mechanical, and thermal properties[153]. Silicone is optically clear and has a tissue similar refractive index at 589nm of approximately 1.41[131], making it a suitable bulk material for the manufacture of tissue mimicking optical phantoms. A variety of scattering and absorbing materials have been successfully incorporated into silicone based phantoms including TiO_2[133], barium sulphate[146], polystyrene microspheres and aluminium oxide[152], PMMA microspheres[154], and silica microspheres[131,142,146] as scatterers, and coffee, nigrosin and India ink[151] as absorbers. Due to its moderate viscosity at room temperature, even distribution of such scattering or absorbing particles within silicone can be difficult. Reduction of the viscosity of the silicone is an effective way of enabling greater control over the particle distribution as a less viscous material is both easier to stir, and more amenable to ultrasound treatment. Both methods used to evenly distribute and reduce aggregation of scatterers. Hexane[131] and tert-butyl alcohol (TBA)[146] are both effective solvents for silicone, and both have been used to reduce its viscosity during phantom manufacture methods. Hexane is far more commonly used, due to its ability to act as a solvent at room temperature, whereas TBA is a solid at room temperature and needs heating to 45^{o}C for use as a solvent[146,155]. Despite its wide use, hexane causes undesired and significant swelling of cured silicone, 30% increase in thickness is observed, whereas TBA only increases the thickness of cured silicone by 5%[155]. A novel approach to the use of silicone as a phantom material is via the addition of glycerol into the silicone matrix. This addition, followed by vigorous mixing, creates a stable emulsion of glycerol filled cavities of micron scale diameter within the silicone, the end result being a scattering and negligibly absorbing phantom created without the addition of exogenous scattering particles[156].

5.3.3. Hydrogels

Hydrogels are composed of one or more different (homopolymeric or copolymeric respectively) monomers, cross-linked to form a polymeric material with the ability to absorb and retain a significant volume of water without being water soluble, although in their non-cross linked form they are water soluble[157]. Commonly encountered hydrogels of biological origin are the protein, gelatine and the carbohydrate, agarose, and synthetic hydrogels include polyacrylamide and polyvinyl alcohol gels – all have a similar elemental composition and refractive index to biological tissues[158,159] and all

have been used successfully in optical phantoms[112]. When fully swollen, hydrogels have a higher percentage mass of water than they do of polymer[157], similar to that of biological tissues where all (except bone and adipose tissues) are composed of at least 50% by mass of water[159] in both adults and neonates[158]. This similarity in water content will help to provide a tissue realistic absorption spectrum as water is one of the main chromophores within biological tissues. A wide range of biological (for example Intralipid™ and bovine erythrocytes in gelatine[160]) and synthetic (for example silica powder and ink in agarose[161]) scatterers and absorbers have been successfully incorporated into hydrogels along with other additives commonly used to increased shelf life, such as antimicrobial agents[112] to create phantoms for a variety of optical techniques.

Natural hydrogels, agarose and gelatine, can be purchased from a variety of sources in powder form. Mixing with water and application of heat allows the non-cross-linked powder to dissolve. On cooling, the mixture solidifies via a process called “gelation” – crosslinking of the polymer chains to form the insoluble hydrogel[162], which is able to mimic the mechanical, thermal, acoustic and optical properties of biological tissues[153]. Exogenous scatterers and absorbers are added as the solution cools, with the cooling mixture subject to continuous stirring[160] or an ultrasonic bath[161,163] to ensure even distribution of particles. Although the manufacturing process is simple and fast, agarose is hard to handle due to its brittle nature, meaning it shatters under light force[164], therefore gelatine may be the preferable material due to the ability to add formaldehyde to the mixture, which induces further polymer cross linking and causes an increase in gel strength[162]. Although visibly transparent, plain gelatine exhibits a small amount of intrinsic scattering, which is apparent via the observation of an OCT speckle pattern. This intrinsic scattering is likely due to the presence of collagen fibres within the gel structure[165].

Changes in environmental conditions, for example temperature, light, pH and pressure can cause hydrogels to dry out[157], and therefore special storage conditions must be adopted to increase their otherwise short lifespan. Refrigerating in an air tight container, ideally in a humid environment, is a commonly adopted strategy[112,160], however immersing the phantom in oil is also successful in reducing water loss[164].

Poly(vinyl alcohol) (PVA) is a biocompatible, non-toxic and novel phantom bulk material. It can demonstrate intrinsic scattering properties via the repeat application of freeze-thaw cycles, hence it is known as a "cryogel". As with other hydrogels, PVA powders are dissolved in a solvent, most commonly water, with the application of heat. The mixture is then cooled, but this time rapidly by cooling to below 0°C. It is this freezing and subsequent thawing at room temperature that causes the formation of cross-linking crystallites[166,167]. If the solvent used is water, then the resulting hydrogel is not optically clear and increasing the number of freeze-thaw cycles in such a gel increases the intrinsic scattering, from μ_s=5.04mm^{-1} for 4 freeze-thaw cycles to 6.90mm^{-1} for 7 cycles[168]. This intrinsic scattering is caused by volume expansion of the water component of the gel and subsequent cavitation of the sample[167]. The use of dimethylsulphoxide (DMSO) in the ratio of 80:20 DMSO:water by weight as a solvent decreases the freezing point of water and therefore reduces the volume expansion and porosity of the sample[168,169], whilst also decreasing crystallinity[166] and therefore increasing the transparency, with a light transmission of over 95%[166,169]. Finally, PVA has been used to create a viscoelastic "slime" via the addition of borax which reduces the stability of the crosslinks formed. Although a freely moving material is not practical for all phantoms – when contained within a latex shell it provides an excellent medium in which to model complex, anthropomorphic geometries[24].

5.3.4. Resins

Resins (polyester, polyurethane or epoxy), like silicone, are prepared using two parts – the liquid resin containing the polymer, and a hardener – which when mixed, cure to form a solid and optically clear material with absorption coefficient of one brand of resin being in the region of 0.001mm^{-1} throughout the optical wavelengths[137]. The manufacturing process of a resin phantom is lengthy. If left to harden at room temperature, the phantom may take over 3 days to reach its full hardness[132]. The hardening reaction is an exothermic one[127] in which large volumes of gas are created, therefore it is imperative to place the phantom within a vacuum chamber to prevent air bubbles curing within the final product[112].The high temperature reached during curing may become a safety risk, and therefore precautions should be taken whilst handling. The ratio of polymer to hardener may be doubled from that recommended by the manufacturer, this stops the curing process being exothermic, and also decreases the curing time to 24 hours[127]. The refractive

index of most resins is approximately 1.54 at 589nm[34], which is higher than that of most biological tissues, however a variety of scatterers and absorbers such as TiO_2[137,170], polystyrene and gold microspheres[143], silica microspheres[34], India ink and Intralipid®[127], can be incorporated into a resin matrix, creating a stable phantom with long shelf life. As well as traditional resins, 3D printing provides a novel use of resins as a matrix material[171,172]. This time the resin is cured by exposure to UV light (photopolymer) rather than via the addition of a hardener. 3D printing offers a unique opportunity to create highly anatomically accurate and detailed phantoms. The addition of polystyrene microspheres to the resin prior to curing, means that a homogeneously scattering sample can also be manufactured via 3D printing[172].

5.3.5. Wax

Gel wax, a novel, mineral oil based, gel like, candle making material, has gained increasing interest as both an optical and acoustic phantom material[173–176] due to its wide availability, low cost and non-toxic nature. It can be used within a 3D printing system[176,177], however if the specialist printing equipment is not available, or cost effective, then a simple manufacturing method for phantoms composed of gel wax with embedded scatterers and absorbers has been presented[173,174]. As well as casting into arbitrary shapes[175], gel wax has already been used to successfully create a variety of anatomically accurate phantoms in conjunction with 3D printed molds of the heart and placenta[174]. Optical scattering and absorption has been modulated by the addition of titanium dioxide (TiO_2), carbon black and colored Inks[173], whilst acoustic properties has been controlled by addition of glass spheres and paraffin wax[174] as well as graphite and TiO_2 powder[176]. Silica microspheres have not yet been used in gel wax, although silica powder has previously been used in a mineral oil based ultrasound phantom[178]. TiO_2 powder provides a more affordable and widely available alternative for optical scattering, that has already been adopted in gel wax phantoms[173,175,176]

6. Optical and X-ray Imaging Phantom Development

6.1. Design Criteria

Phantoms are required for the development and refinement of both optical and x-ray scattering measurement techniques and data analysis methods, and therefore require the following essential properties:

1. Tuneable optical scattering (μ_s') – it should be possible to create different values of μ_s' using the chosen combinations of bulk material and scatterer. The measurement of the optical properties would also be used to ensure that the concentration of scattering particles was as expected, as a linear relationship between scatterer concentration and μ_s' would be expected.

2. Phantoms which exhibit x-ray scattering, measurable by the EI-XPCi system. Solid, phase contrast phantoms, with tuneable x-ray scattering signals, have not previously been manufactured specifically for use within the EI-XPCi system. Therefore, it was necessary to experimentally develop design parameters for x-ray scattering phantoms. As a result of this, phantoms should be created initially according to a specified optical scattering. Unlike for optical scatter phantoms, where Mie theory is used to predict the scattering coefficient, there is currently no means of predicting the x-ray scattering signal that a particular phantom will generate within the EI-XPCi system. Scatterers and bulk materials with different electronic densities should therefore be chosen, as the δ value, and therefore refraction and scattering signal, are dependent on this. The relationship between scatterer density and EI-XPCi scattering signal may be established for each phantom type by experimental measurement using the known scatterer concentrations which are verified using optical measurement.

3. Ability to cast the bulk material – scatterer mixture, into a variety of shapes and thicknesses for use within multiple measurement techniques is imperative to allow refinement of the methods. Samples for use within the spectrophotometer must be sandwiched between two glass slides, and should be uniformly thin[26], however x-ray phantoms should be self-supporting, and not reliant on highly absorbing glass slides to hold them in place.

4. Stability in both x-ray and optical properties over period of at minimum one week. However, ideally, stability should extend to months or years, to allow repeat measurement on multiple imaging modalities during the x-ray and optical method refinement process.

Furthermore, the following desirable, but non-essential criteria were specified:

1. Tissue mimicking for both optical imaging and x-ray phase contrast imaging, and

2. Simple storage requirements.

It should also be noted that phantoms containing TiO_2 are widely considered as providing tissue mimicking optical scattering despite their high refractive index and negligible absorption, therefore a higher refractive index (or δ in the x-ray case) does not preclude a material's ability to provide tissue realistic scatter. As the scattering signal in optical and x-ray wavelengths is a complex combination of a variety of factors and given the central hypothesis of this thesis, it would be reasonable to assume that the factors affecting the x-ray scattering were the same as those effecting the optical scattering, therefore a scatterer considered to be tissue realistic in the optical wavelengths would also create tissue realistic x-ray scatter. Finally, as the measurement, retrieval and definition of x-ray scattering using current methods was known to be unreliable at the time of phantom design, it was decided that ensuring there would be a retrievable x-ray scattering signal was of greatest importance. Silica microspheres were therefore chosen, as silica containing microspheres of differing diameter had previously been used to elicit x-ray scattering[179] and TiO_2 also chosen due to its similar chemical formulation to silica, along with having particle diameters (<5μm) previously considered in x-ray scattering particles[179].

Considering the above listed design requirements, agarose, gel wax and silicone were chosen as bulk materials and TiO_2 powder and SiO_2 microspheres as scatterers. All bulk materials and scatterers have been previously used as tissue mimicking optical phantom materials[112,113], however none have been used previously as phantoms within the EI-XPCi system. Incorporation of scatterers with values of δ (approximately 2.6×10^{-6} and 1.3×10^{-6} at 18KeV for TiO_2 and SiO_2 respectively), exceeding that of bulk

materials with lower, more biologically relevant δ values, was expected to create a retrievable scattering signal within the EI-XPCi system. The stability and ease of storage of gel wax was initially unknown and the stability of agarose was known to be limited to short times, with complex storage requirements[112,157], therefore silicone phantoms were also chosen as they offer greater stability[112] with no complex storage requirements. Finally, all materials were able to be moulded into a variety of shapes due to their low viscosity prior to casting, and flexibility once cast, allowing phantoms to be removed with ease from the moulds.

6.2. Methods

6.2.1 Materials

Multiple phantoms of varying scatterer concentration, each comprising of one of three different bulk materials embedded with one of two different scatterers, were manufactured for evaluation as both optical and x-ray scattering phantoms. Each phantom was designed to have known optical scattering, and unknown, but expected x-ray scattering. The bulk materials used were silicone (Elastosil 601 RTV, Wacker Chemie, Munich, Germany), agarose (Product A9539, Sigma Aldrich, Dorset UK) and gel wax (Mindsets (UK) Ltd., Saffron Walden, UK), all of which had similar, tissue realistic refractive indices at 589nm (1.409, 1.34, 1.4 respectively[180–182]). Scattering was introduced by embedding either silica microspheres or TiO_2 powder within the bulk materials. Mean particle size of the TiO_2 powder was <5µm (Product 224227, Titanium (IV) oxide, rutile, Sigma Aldrich, Dorset, UK). The refractive index of the TiO_2 (n_{TiO2}) was not provided by the manufacturer, therefore 2.5082[183] at 589nm was assumed, creating phantoms with a g value of approximately 0.7. Two brands of silica microspheres were considered. Initially 1µm+/- 10%[34] diameter microspheres (Monospher® 1000, Merck, Darmstadt, Germany) were used, and latterly monodisperse silica microspheres of 1µm diameter (Pinfire – Gems and Colloids, Frankfurt, Germany) with a coefficient of variance of <5% were considered, both creating phantoms with a g of between 0.9 and 1. The refractive index of the Monospher microspheres (n_{silica}) was not provided by the manufacturer, therefore initial estimates were based on data for fused silica - 1.4584[140]. The refractive index for the Pinfire silica microspheres (n_{silica}) was quoted as 1.467 at 589nm by the manufacturer, however further information regarding the

wavelength dependence was not available. Silica microspheres provide a more tissue realistic scatter due to the refractive index of the spheres and bulk materials being similar to that of intracellular organelles and cytoplasm respectively[31,184]. As well as offering differing amounts of optical scattering, it is assumed that each combination of scatterer and bulk material will offer varying x-ray properties.

6.2.2 Silicone Phantoms

Work reported in this subsection, regarding the development of silicone phantoms was published in: Charlotte J. Maughan Jones, Peter R. T. Munro, "Development of a reliable and reproducible phantom manufacturing method using silica microspheres in silicone," J. Biomed. Opt. 22(9) 095004 (18 September 2017). https://doi.org/10.1117/1.JBO.22.9.095004

6.2.2.1. Silicone and Silica Microsphere Phantoms

The procedure presented by Bisaillon et al. for incorporating silica microspheres into silicone rubber[131] is considered a robust method for producing phantoms with homogeneously distributed microspheres, however alternative methods for producing silicone and microsphere phantoms have also been presented[142,146,152] without comparison of resulting phantom quality. Two methods of phantom manufacture are presented here. The first (‘Method 1’), a replication of an existing method by Curatolo et al.[154] which was based on a modified, shortened, version of the process described by Bisaillon et al.[131]. The second method, an improvement on Method 1, (‘Method 2’) was devised to overcome the problems encountered during the implementation of Method 1. All difficulties encountered, resulting solutions and method modifications are discussed in detail. Both methods were analysed for their ability to create phantoms with a homogeneous sphere distribution, evidence for the attained improvements in homogeneity when using Method 2 is presented, in doing so we also present a novel method for assessing sphere distribution using x-ray phase contrast microscopy.

6.2.2.2 Materials

Phantoms were constructed using silica microspheres of 1µm diameter Monospher® 1000 (Merck, Darmstadt, Germany) embedded within a 2-part addition curing, room temperature vulcanising silicone rubber - Elastosil® RT 601 (Wacker Chemie AG, Munich, Germany). The silicone consists of a

viscous ‘part A’ (platinum catalyst and polydimethylsiloxane polymer), which, when mixed with ‘part B’ (cross-linker and polydimethylsiloxane) forms an optically clear, deformable and durable rubber. The density of the cured silicone rubber was provided by the manufacturers, with the density of silica microspheres based on data for fused silica, 1.02g/ml[74] and 2.203g/ml[185] respectively. Mie and continuum theory were used to calculate the number of spheres per unit volume required to manufacture multiple phantoms to achieve a particular scattering coefficient, μ_s.

6.2.2.3. Mie Theory and Phantom Design

The known and estimated optical and physical properties of the silicone and microspheres enabled Mie and continuum theory[20] to be used to calculate the quantities required of each of the phantom components to create a phantom of known thickness and scattering coefficient. This was done as follows:

Using the online Mie calculator (http://omlc.org/calc/mie_calc.html) created by Scott Prahl (Oregon Medical Laser Center), along with the manufacturer provided refractive index of silica and silicone, the theoretical μ_s for a concentration (C_{max}) of closely packed spheres of known diameter and therefore volume (V_{sphere}) was calculated (μ_s^{max}). With C_{max} estimated as,

$$C_{max} = \frac{1\mu m^3}{V_{sphere}}. \qquad \textit{Equation 32}$$

C_{max} is an estimate of the concentration of spheres when purchased, however neglects the spaces between the spheres, which would occur when spheres are tightly packed within a container. Note, however, that neglecting the space between spheres in this way does not introduce error since C_{max} is used only as a reference concentration and it does not matter if it is physically realisable. The required scattering coefficient of the phantom is specified ($\mu_s^{phantom}$), and along with μ_s^{max} is used to calculate how much the purchased concentration of spheres must be diluted to reach $\mu_s^{phantom}$. This dilution factor (F) can then be used to calculate the concentration of spheres ($C_{phantom}$) required to create a phantom with a defined scattering coefficient $\mu_s^{phantom}$,

$$F = \frac{\mu_s^{phantom}}{\mu_s^{max}}, \qquad \textit{Equation 33}$$

And,

$C_{phantom} = \frac{C_{max}}{F}$, *Equation 34*

Given the concentration of spheres that would be required to create a phantom of known scattering coefficient - $\mu_s^{phantom}$- the total number of spheres (N) required to make a phantom of concentration, $C_{phantom}$ and volume, $V_{phantom}$, can be calculated,

$N = V_{phantom} \times C_{phantom}$. *Equation 35*

With knowledge of the volume of a single sphere, as well as the density of silica, the total number of spheres required can be used to calculate the total mass of spheres required to create a phantom of sphere concentration $C_{phantom}$ and scattering coefficient $\mu_s^{phantom}$. Finally, the mass and volume of silicone required to suspend the now determined quantity of spheres was calculated using the physical density of silicone. The quantities of silicone and silica microspheres were scaled up equally to enable a larger volume, enough to create approximately 10 phantoms per batch to be made.

All phantoms were initially designed at a wavelength of 850nm, with the assumption that the refractive index of silicone rubber remained constant over all visible wavelengths and therefore the manufacturer supplied value at 589nm ($n_{silicone}$=1.409) could be used. However once manufactured the μ_s value of each phantom was recalculated at 589nm due to concerns over the reliability of the previous assumption regarding the value of $n_{silicone}$.

During the manufacturing process the mass of silica microspheres and silicone A, along with the volume of silicone B was recorded, therefore enabling the calculation of the accurate Mie predicted value of μ_s. From the quantities of silicone (A and B) and microspheres, along with their associated physical densities the total volume of the batch was calculated. The total volume of spheres (calculated from the mass, using the physical density) within the batch was used to determine the number of spheres within each phantom by simply dividing the total volume of all spheres by that of 1 sphere. By dividing the number of spheres by the total volume of the batch (in μm^3), the sphere density was determined, and this, along with $n_{spheres}$, $n_{silicone}$, the corresponding wavelength and the sphere diameter were used as input for the online Mie calculator, enabling determination of the predicted value of μ_s and g.

From herein the value referred to as the “Mie predicted value” of μ_s will refer exclusively to the post manufacturing calculated value, and not the designed value ($\mu_s^{phantom}$).

6.2.2.4. Method 1

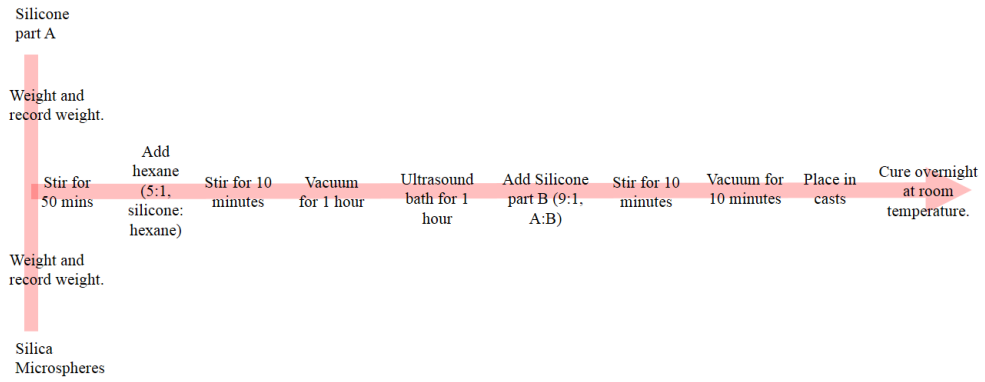

Figure 17. *Summary of Method 1 of phantom manufacture*

An overview of Method 1 is shown in Figure 17. Stirring was performed using an overhead mechanical stirrer and was done to encourage even microsphere distribution within the silicone, which was further aided by the addition of hexane. Hexane thins the silicone, making it easier to stir, whilst also increasing the effectiveness of the ultrasound bath in breaking up sphere aggregates. A less viscous silicone also aids the efficient removal of air bubbles from the microsphere-silicone mixture when in the vacuum chamber. It is assumed that the hexane has fully evaporated from the phantom prior to curing as the vacuum chamber also encourages complete hexane evaporation. Silicone part B was added in a 9:1 ratio (part A:part B) based on manufacturers recommendation[186], with the volume required calculated from the recorded mass of silicone part A. Casts were constructed from glass slides and no. 2 coverslips (Figure 18). A glass slide was placed on top of the mixture to maintain a constant thickness and smooth surface, thus creating a phantom of minimum thickness of 200µm which is the standard thickness of a no. 2 coverslip, with the eventual cured thickness determined by digital calliper measurement. The phantoms were left

overnight at room temperature to cure, after which they were removed from the casts and trimmed to the desired size.

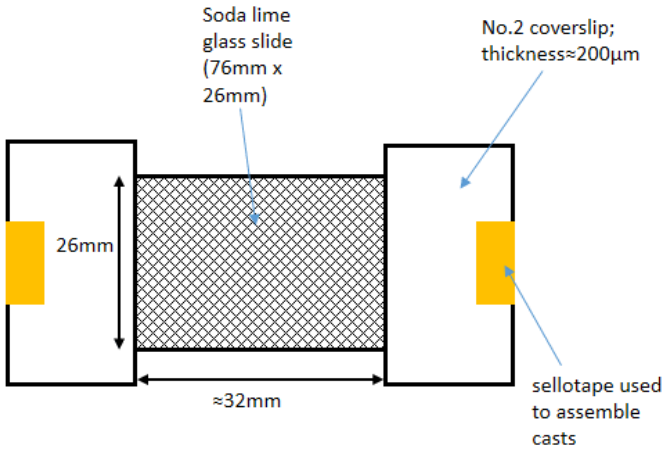

Figure 18. *Diagram of casts used to create phantoms. Each cast was made using glass slides and no. 2 coverslips. The patterned region is the area used for casting and is approximately 26mm x 32mm.*

6.2.2.5. Method 2 – Overcoming Aggregation

After the discovery of sphere aggregates within the phantoms made using Method 1 via the use of x-ray microscopy (6.2.3.1. c X-ray microscopy), and by visual inspection of phantoms, the following modifications were made to the manufacturing process in an attempt to reduce aggregation:

1. Physically grind spheres in a metal bowl using a metal spatula to reduce macroscopic aggregates
2. Increased time in ultrasound bath - 2 hours in total.
3. Ultrasound bath before vacuum so that silicone is at its lowest viscosity after hexane addition, and again after vacuum to re-suspend after period of static activity in the vacuum.
4. Increased hexane (1:1 ratio silicone A:hexane) to reduce silicone viscosity and increase microsphere dispersion

Aggregation was assessed using x-ray microscopy, OCT and spectrophotometry (6.2.3. Verification of Aggregation Reduction and Method Improvement), and a reduction in the scatterer aggregation was observed as a result of the above modifications. The modifications adopted above successfully reduced, but did not eliminate aggregation, yet led to other problems:

1. Significant shrinkage of the phantom post curing. The phantom was seen to peel away from the overlying glass slide, leaving visible marks on the surface. (Figure 19).
2. Adherence of the phantom to the upper and lower glass slides. The phantom was permanently stuck to the cast and was unable to be removed as required.

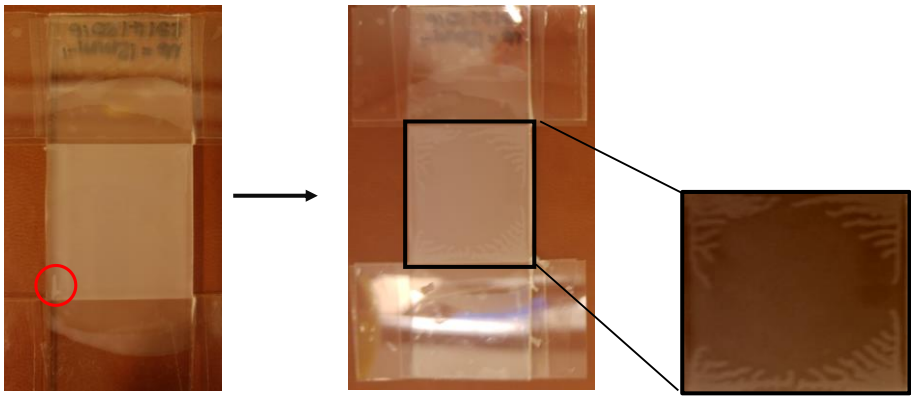

Figure 19. *(Left) evidence of shrinkage was seen immediately after curing, with further, and more extensive shrinkage occurring over the following 24hours post curing (centre). Evidence of shrinkage can be seen as finger like projections which are created as the phantom peels away from cast (right). These projections are imprinted onto the phantom.*

6.2.2.6. Overcoming Shrinkage

Shrinkage can be attributed to the increased ratio of hexane used to reduce the viscosity and aid microsphere dispersion. Hexane is used to swell silicone[155], and once evaporated, the silicone shrinks and returns to its natural state, shrinking, and in this case, peeling away from the casts, leaving visible marks on the surface of the phantom. It is often assumed that hexane has fully evaporated before curing commences[131,142,187], but the presence of shrinkage once fully cured would suggest that this assumption is not true. To confirm that an increased ratio of hexane to silicone was responsible for the shrinkage, 3 batches of phantoms were made using Method 2, but with varying quantities of hexane. The ratio of hexane to silicone part A was varied from 1:4 to 1:1. Shrinkage was still observed with a 1:2 ratio, however became minimal in phantoms made using a ratio of 1:4, confirming that the increased volume of hexane was indeed responsible for the observed shrinkage. Reducing the volume of hexane to reduce shrinkage leads to

greater sphere aggregation, therefore a ratio of 1:1 hexane to silicone was used, with methods to increase hexane evaporation prior to curing adopted to minimise its effect. Hexane was added at the start of the stirring process to increase the time available for evaporation, and the time spent within the vacuum was increased to 2 hours. Furthermore, all stirring occurred within a fume hood, which encouraged evaporation by increasing air flow round the sample. These methods reduced, but did not fully eliminate shrinkage, therefore samples were cured quickly at 70°C for 10 minutes, and then removed from their casts, so that shrinkage could occur evenly without creating visible marks.

6.2.2.7. Overcoming Adsorption

On addition of a higher ratio of hexane, the cured phantom became strongly bonded and adhered to the surface of the slides, making it impossible to remove them from their casts.

a. Surface Chemistry of Silica Glass

The main component of soda lime glass is SiO_2, and the cut surface of SiO_2 based glass displays some unique properties and is largely hydrophilic. The surface of glass is made up of silanol groups (–SOH) which can either be isolated (not close enough to another group to form a hydrogen bond), geminal (two –OH groups attached to one Si), or vicinal (close enough to each other that hydrogen bonds can form). As well as silanol groups which give the surface its hydrophilic properties, stable siloxane bridges exist[188] (Figure 20).

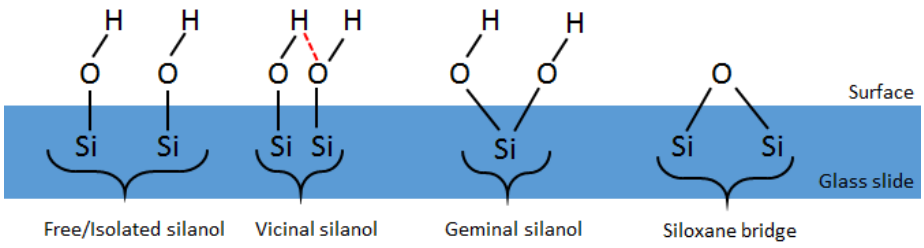

Figure 20. *Surface groups found on a typical SiO_2 glass surface. The hydrogen bond formed by the vicinal silanol is shown in red.*

All exposed surface silanol groups can form strong hydrogen bonds with external molecules, for example water or silicone, a process called adsorption. Siloxane bridges however are stable and therefore unable to

react in such a way in room temperature conditions. It is therefore preferential to increase the proportion of siloxane bridges to create a more inert surface. The hazardous liquid, n-Octyltrimethoxysilane can be used to provide a hydrophobic coating on the surface of a glass slide[146]. Alternatively, heating provides a simple way of modifying the adsorption of the glass surface, in a process known as passivation. By heating the glass, a dehydroxylation condensation reaction of the surface silanol groups occurs, creating siloxane bridges via the loss of a water molecule (Figure 21). To create stable siloxane bridges, a temperature of at least 400ºC[188] is required, with some suggesting a much higher 650ºC[189]. Heating to temperatures of below 400ºC will still create siloxane bridges and cause a decrease in the concentration of surface –OH groups from the standard 5 -OH/nm^2 [188,190], however the temperature must be at least 150ºC[191]. At these temperatures, the siloxane bridges that are formed are 'strained' and may react to reform silanol groups in the presence of excess environmental water[188].

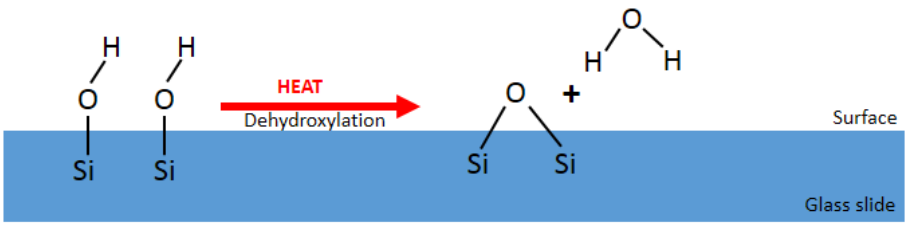

Figure 21. *Dehydroxylation reaction - creating a siloxane bridge from 2 isolated silanol groups. The same reaction can occur with both vicinal and geminal silanols.*

The phantom manufacturing method was modified accordingly to reduce the adsorption between the silicone and glass slides. The slides were cleaned using an ultrasound bath for 15 minutes, after which they were thoroughly dried by heating for 5 minutes at 200ºC. Immediately before assembling the casts, the slides were again heated to 200ºC, but this time for 30 minutes to facilitate the dehydroxylation reaction. Although heating to above 400ºC, where stable siloxane bridges are formed would be ideal, equipment to reach this temperature was not available within the laboratory, and further safety precautions would have to be adopted to work at these temperatures. Increasing the number of siloxane bridges found on the surface, even by a small amount, disrupts the ideal one to one siloxane to silanol ratio required

for effective water adsorption[189]. This modification had the profound effect of enabling the phantom to be removed from its cast with exceptional ease.

All above modifications to prevent adsorption and reduce shrinkage, were incorporated into Method 1, to create Method 2 (Figure 22). These changes created a method with greater similarity to that presented by Bisaillon et al.[131]. It should be noted that phantoms of μ_s=0mm^{-1} were made using pure silicone without the addition of microspheres (named 0a, 0b and 0c). Although microspheres were not used in this phantom, all other manufacturing steps were followed so as to see the effect that the manufacturing process has on the final optical properties of silicone.

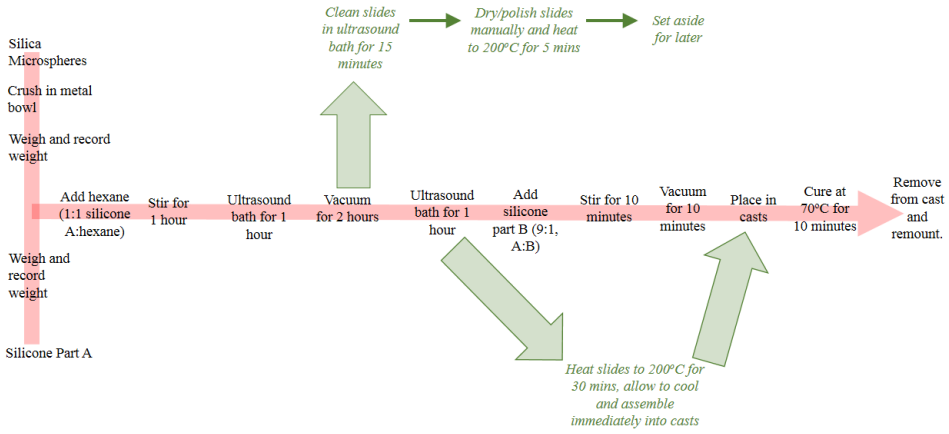

Figure 22. *Summary of Method 2 of phantom manufacture, including steps to reduce sphere aggregation, shrinkage and adherence to the slide.*

6.2.2.8. Phantom Preparation

After removal from their casts, all phantoms made using both Method 1 and 2 were mounted between 2 glass slides using small volumes of clear silicone creating a stable sample ready for characterisation. Two slides per phantom were prepared by cleaning using surgical spirit followed by water – slides were then thoroughly dried to leave a streak and debris free finish. A thin layer of clear silicone was spread over the surface of a clean glass slide. The phantom was placed on top of this and gentle pressure was applied to ensure air free contact between the phantom and the silicone. A further layer of silicone was then placed on top of the phantom and a second glass slide was placed on top. Gentle pressure was again applied to the now remounted

phantom to ensure the silicone layers between both phantom-glass interfaces were even, air free and thin. The silicone layers were cured rapidly at 100^{o}C for 5 minutes, after which the phantoms were ready for measurement. The thickness of the silicone is negligible and is therefore assumed to have no effect on the optical properties of the sample. The remounted phantoms are physically stable and can be stored for repeated use.

6.2.2.9. Method 1 and Method 2 Phantoms

In total 9 batches were made using Method 1, and 6 using Method 2. Details of these can be found in Table 2. Between 2 and 4 phantoms were made per batch, however those containing visible air bubbles, or debris were discarded, leading to a variable number of phantoms being available for verification per batch. Further to this, any phantoms with macroscopically visible aggregation were also discarded. A total of 9 batches were made using Method 1, of which 5 were completely discarded due to aggregation or air bubbles. In contrast, 6 batches were made using Method 2 of which none was entirely discarded, and those that were discarded from Method 2 batches were discarded due to accidental damage or air bubbles rather than aggregation. In total, 69% of manufactured phantoms were discarded for Method 1, with a reduced, but still significant percentage of 43% from Method 2. Due to entire batches manufactured using Method 1 being discarded, the Method 1 phantoms considered here are, therefore, are only those of excellent macroscopic quality.

Method	Batch	Number of phantoms for analysis	Number of phantoms discarded	Reasons for discarding	% Scatterer by weight	Mie Predicted μ_s (mm^{-1}) at 589nm
Method 1	1a	3	1	Aggregation	13.1%	10.4
	1b	1	1	Damage	21.6%	16.9
	1c	3	1	Air bubbles	31.0%	23.4
	1d	3	1	Damage	46.3%	33.1
	1e	0	3	Debris/air bubbles	13.2%	10.7
	1f	0	3	Air bubbles	29.4%	22.3
	1g	0	4	Air bubbles	36.6%	27.1
	1h	0	4	Aggregation	13.1%	10.4
	1i	0	4	Air bubbles/ Aggregation	36.5%	27.0
Method 2	2a	3	1	Damage	12.9%	10.5
	2b	1	3	Air bubbles	13.0%	10.5
	2c	1	3	Air bubbles	29.6%	22.5
	2d	3	0	n/a	29.0%	22.1
	2e	2	2	Damage	44.9%	32.2
	2f	2	0	n/a	47.7%	33.9

Table 2. *The number of phantoms kept and discarded per batch for both manufacturing methods. The reason for discarding listed as "damage" refers to accidental damage inflicted on the phantoms as they were being unmounted from the casts, or whilst they were being prepared for measurement, and are not an indication of problems with the manufacturing process.*

Batches of similar scatterer concentrations (for example 2a/2b, 2c/2d and 2e/f) are considered separately as each batch in Table 2 represents a separately manufactured mixture of silica microspheres and silicone rubber. Therefore, although the scatterer concentrations are the same, the phantoms manufactured from (for example) batch 2a, are not subjected to exactly the same manufacturing conditions as those in batch 2b, therefore their degree of aggregation may have been different, and it was not appropriate to group them together purely based on their scatterer concentrations.

The ‘Mie Predicted’ value of μ_s refers to the value calculated from the recorded mass of silicone part A and B, as well as that of the silica microspheres that were used during the manufacturing process. The ‘% scatterer by weight’ represents the ratio of the initial mass of silica microspheres compared to the initial mass of silicone part A used during phantom manufacture. Both values make no attempt to correct for any losses during the manufacturing process, and represent the values expected if no losses were to occur.

6.2.3. Verification of Aggregation Reduction and Method Improvement

The homogeneity of phantoms was subjectively analysed using optical coherence tomography (OCT) and x-ray microscopy following initial visual inspection. The x-ray microscopy images were also used to subjectively assess the microspheres, their size and shape. The scattering coefficients of all phantoms manufactured via the above method were subsequently determined via use of a dual beam spectrophotometer to provide quantitative evidence of method improvement.

Multiple techniques were employed to subjectively and objectively assess the homogeneity of the microsphere distribution due to the ability to assess different properties of the phantoms. X-ray microscopy is costly, and the image acquisition time lengthy. This, along with the destructive method of imaging, and very small sample size, preclude its use as a high throughput method of analysing phantom quality, however its resolution is unobtainable with an OCT system, therefore allowing for the resolution of individual spheres and their aggregations, allowing subjective, qualitative assessment of aggregation. OCT image acquisition is, in comparison, quick, therefore allowing the qualitative assessment of multiple phantoms in a short time frame. Although the field of view is limited by the system, the ability to move the phantom whilst obtaining live A scans, means that the entire phantom can be assessed quickly and effectively. However, although inconsistencies within a phantom can be noted, the cause of these cannot be determined from OCT alone due to the inability to resolve detail as small as one microsphere. X-ray microscopy and OCT both obtain images of the microstructure of the phantoms, however the use of a spectrophotometer with integrating sphere is a well-established method of accurately determining the average optical properties of a volume of a sample (2.3.1.1.

Spectrophotometer and Inverse Adding Doubling) allowing quantitative analysis of, and confirmation of the subjective assessment of, degree of aggregation as seen on OCT and microscopy. The averaged optical properties are determined for a much larger volume of the phantom compared with OCT and X-ray microscopy and are thus useful in characterising homogeneity of optical properties throughout macroscopic volumes of tissue.

6.2.3.1. Subjective analysis

a. Visual inspection

When inspecting phantoms by eye, it was noted that many of the phantoms made using Method 1 contained large visible macroscopic granules. The reason for these granules could not be determined by eye, and further microscopic techniques were employed to further understand the reliability of the method. Such granules were not observed for those made using Method 2, for which all phantoms appeared macroscopically homogeneous, an early indication that Method 2 was able to produce more consistent and homogeneous results that Method 1. Table 2 indicates the number of phantoms that were discarded due to, amongst other reasons, aggregation, where it can be noted that no phantoms from method 2 were rejected for this reason.

b. Optical Coherence Tomography (OCT)

The OCT system used was developed by the advanced optics group at the University of Kent in Canterbury displaying live *en face* images from 9 depths[192], and operated at a wavelength of 1300nm. Phantoms were placed on the sample stage and a random location of the sample was chosen to observe B scans and *en face* images. The phantom was turned over and the process repeated at a second random location. Images were stored from areas with evidence of aggregation. Two phantoms from Method 1 (1a3 and 1d2), and two from Method 2 (2a3 and 2f1), were examined, where 1a3 and 2a3 have comparable sphere concentrations, as do 1d2 and 2f1. These phantoms were chosen for imaging as they represent the lowest and highest sphere concentrations manufactured respectively.

If the distribution of spheres within each phantom was uniform throughout, then it would be expected that the speckle pattern observed in both B-scan

and en face images (2.3.1.2. Optical Coherence Tomography) would be of homogeneous texture[27]. Areas of inhomogeneous speckle texture, indicative of sphere aggregation, were observed for both phantoms with the lowest sphere concentrations (1a3 and 2a3), however, a greater number as well as larger size of aggregates was subjectively seen for the phantom manufactured using Method 1 compared to Method 2. Figure 23 (a and b) shows the considerable size difference between the largest aggregate seen within the 2 phantoms of lowest sphere concentration. When considering the phantoms with the highest sphere concentrations (1d2 and 2f1), the speckle pattern was highly homogeneous with very few imperfections seen in either phantom. One of the few imperfections seen in both phantoms is depicted in Figure 23 (c and d). In between visible regions of aggregation, the speckle pattern was largely homogeneous (Figure 23– lower row), indicative of at least partial success of aggregation reduction techniques.

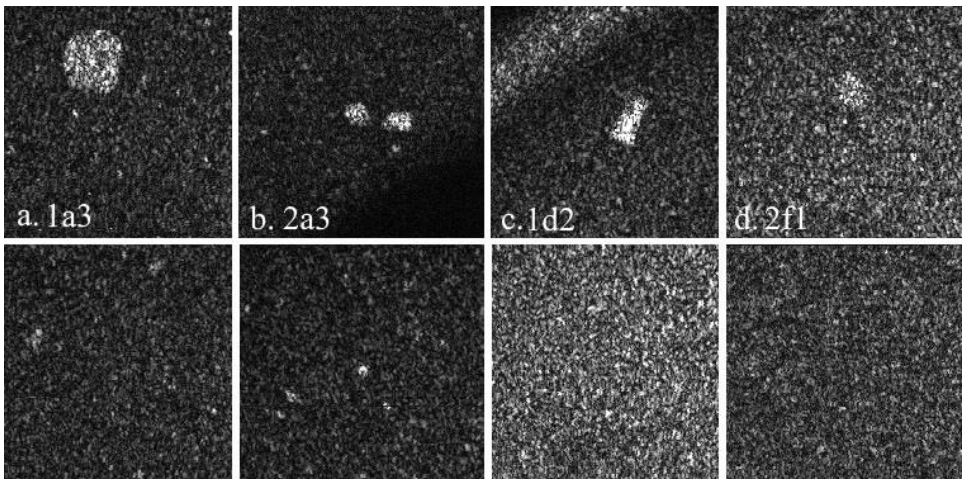

Figure 23. *OCT en face images of 4 phantoms. Top - Largest aggregate found within each phantom. Bottom - homogeneous area in between visible aggregates. All images are taken from OCT images of the same magnification, so direct comparison may be made.*

The cause of the areas of increased signal seen in the OCT images cannot be determined from these images alone as the spatial resolution is not adequate for structural imaging of the individual spheres, however 2 potential sources to be considered would be a) aggregation of spheres, b) air bubbles cured within the phantom. However, as OCT is a high throughput system, it should be considered as a viable option for phantom verification in the future.

c X-ray microscopy

A Zeiss Xradia 810 Ultra, nanoscale X-ray imaging system (Carl Zeiss AG, Oberkochen, Germany) within the department of Chemical Engineering at UCL was used to obtain high spatial resolution (150nm resolution) images of a phantom. Due to the cost of, and length of time it takes to image one sample, it was not feasible to gather images for all the phantoms, therefore one phantom made using each method was chosen for examination – both phantoms examined were designed to have the same sphere concentration, therefore images were directly comparable. A piece of the fully cured phantom, approximately 65μm in width, was removed and attached to the tip of a pin using epoxy resin. The sample was inspected under light microscopy to ensure it was of adequate size (Figure 24) and then was left 24 hours to ensure thermal stability, after which a full x-ray microscopy CT acquisition was performed. Slices through each of the phantoms were obtained from the reconstructed CT image, allowing subjective analysis of the degree of aggregation throughout the sample.

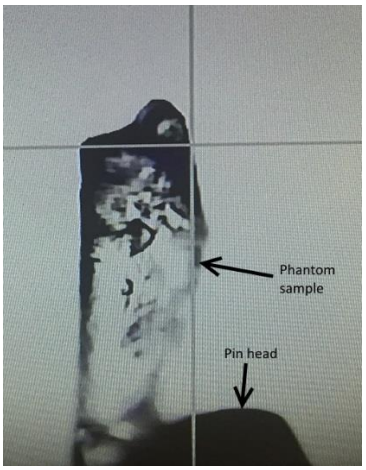

Figure 24. *Light microscopy image of sample of phantom mounted on pin head. The phantom is assessed on its geometry to ensure it is neither too big nor too small to be imaged.*

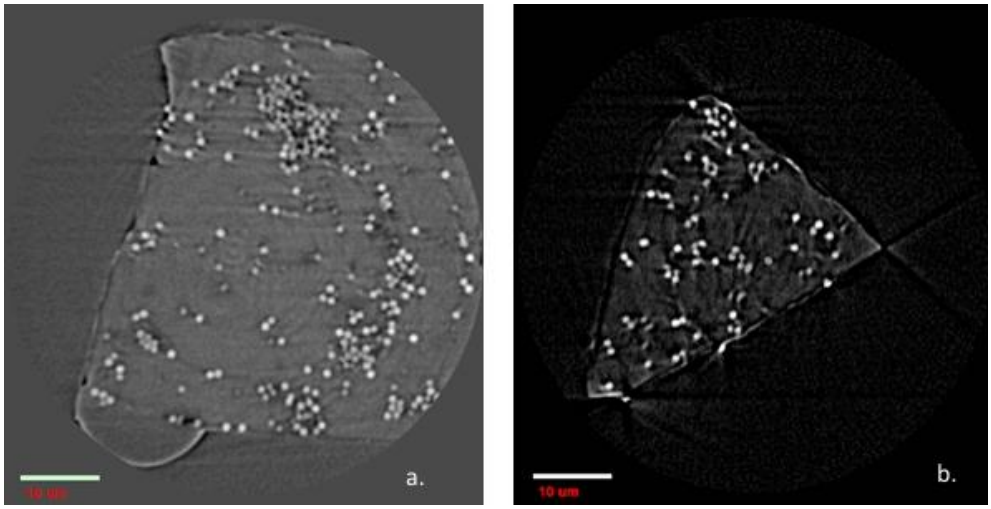

Figure 25. *X-ray microscopy image of representative slice through phantoms made using a. Method 1, and b. Method 2. Both phantoms were designed to have the same sphere density.*

Figure 25 confirms that sphere aggregation is present throughout the phantom made using Method 1. The aggregates vary in size, with large irregular aggregates dominating. The aggregates appear to be randomly distributed throughout the entire volume of the phantom, with no area predilection. An apparent decrease in both the number and size of aggregates present is observed in the phantom made using Method 2, this time aggregates containing fewer spheres appear to dominate. The spheres were otherwise evenly distributed throughout the phantom, and fewer large aggregates compared with the Method 1 phantom are seen, although aggregation was not eliminated, an apparent improvement was seen. When considering the phantom made using Method 2, one larger aggregate was noted towards the tip of the sample, however due to significant movement blur created by the flexible sample, it was difficult to ascertain the extent and significance of aggregation in this region, or whether this was purely a movement artefact, and the slice seen in Figure 25b was considered more representative of the overall sphere distribution.

6.2.3.2. Objective Analysis - Spectrophotometer

X-ray microscopy and OCT both have limitations in terms of assessing the degree of aggregation, namely a limited ability in quantifying an improvement. For OCT, analysing the speckle size within the images was

considered. However, this proved to be an unreliable method for isolating regions of increased contrast caused by aggregations. A suitable method of quantitative analysis with regards to the OCT images could not be identified. Quantitative segmentation of the x-ray microscopy images was considered in order to quantify the degree of aggregation caused by each method, however initial attempts at performing this specialised task proved unsuccessful. When considering that access to the x-ray microscopy equipment is limited as well as the complex, destructive, sample mounting requirements it was decided to pursue a more time effective, non-destructive method of quantitative analysis. Analysis of the standard deviation of μ'_s values as measured via spectrophotometry provided a time effective, non-destructive, and established method of analysing the optical properties of a phantom, and the quantitative data collected from the spectrophotometer forms the basis of the conclusions in this thesis, as well as those previously published[1].

a. Method

A Perkin Elmer® Lambda 750 dual beam spectrophotometer with 100mm single integrating sphere detector accessory was used, allowing measurement of sample reflectance and transmittance within the operating wavelength range of 190nm to 3300nm. Each sample was measured for both reflectance and transmittance over the wavelength range 400 to 1350nm. Ideally each phantom would be repositioned multiple times with many areas of the same phantom measured to obtain a more accurate value of μ_s, however due to their small size (approximately 20mm x 30mm, width x height) compared to the reflectance (17mm x 22mm) and transmittance ports (11mm x 24mm) this was not possible, so one measurement for each phantom was made, the mean being calculated from the multiple phantoms made from the same batch.

b. Inverse Adding Doubling (IAD)

The reduced scattering coefficient (μ'_s) values were extracted using the inverse adding doubling (IAD) programme[26] as mentioned previously (2.3.1.1. Spectrophotometer and Inverse Adding Doubling), and the μ_s values calculated using the relationship $\mu'_s = \mu_s(1-g)$. Calibration measurements for both 100% and 0% reflectance and transmittance were made in line with recommendations for IAD[26]. “Dual beam corrections” were applied, and an

error tolerance of 0.1 (as calculated in the IAD handbook[26]) was specified, as convergence at the standard lower error was not possible. This value specifies the error tolerated by the IAD programme before it terminates, and therefore determines the error in the calculated value of μ'_s, with lower error values producing more accurate optical properties. The thickness of each sample (once mounted) was determined using digital callipers, with the specified thickness of 2 slides (1mm per slide) subtracted to reveal the thickness of the sample itself. This value was used as input in IAD. The slide thickness of 1mm was provided by the slide manufacturers (Thermo Fisher Scientific, Massachusetts, USA), and is the standard thickness of microscope slides. As the slide thicknesses were not individually measured for each phantom, this remains a source of error in the IAD calculations, however it is assumed that the effect is negligible due to the standard thickness specifications of microscope slides.

6.2.3.3. Results

a. Plain Silicone

If simply mixed in the ratio of 9:1, part A: part B then the cured silicone theoretically has no intrinsic scattering ability due to its structural homogeneity, i.e. μ_s = 0mm^{-1}, and ideally the manufacturing process would have no effect on the optical properties. Three plain silicone phantoms made using Method 2 were measured, the value of μ_s for 2 of the phantoms was 0mm^{-1} as expected and 0.01mm^{-1} in the third – therefore it is reasonable to say that the manufacturing process has a negligible effect on the intrinsic scattering of silicone and any scattering observed from the phantoms is solely due to the presence of the silica microspheres within the silicone.

b. Uncertainty Analysis

To determine the uncertainty in obtaining the value of μ_s via spectrophotometry and IAD, Four phantoms – 0b, 2a3, 2d2, 2f1- were selected for consecutive, repeat, measurements at 589nm. These phantoms represent the full range of sphere concentrations. Each phantom was placed in the transmittance port and 10 consecutive transmittance measurements were made without moving the phantom. This was repeated in the reflectance port for the reflectance measurements. The IAD program was then used to obtain 10 values of μ_s per phantom, and from this an error

associated with this method of obtaining μ_s was determined. This resulted in estimated values of μ_s as 0.060 +/-0.003 mm^{-1}, 5.71+/-0.08 mm^{-1}, 8.1+/-0.4 mm^{-1} and 12.34+/-0.02 mm^{-1} for samples 0b, 2a3, 2d2 and 2f1, respectively, with the uncertainty being the standard deviation of the 10 values per phantom. This illustrates the precision with which an measurement of μ_s can be obtained. It should be noted that the uncertainty in μ_s for sample 2d2 is higher than the other samples which is likely due to an unidentified imperfection in the sample. This analysis shows that the uncertainty in estimates of μ_s obtained by spectrophotometry is sufficiently low to support the claims made later in this work. The analysis of the uncertainty inherent to the estimation of μ_s using spectrophotometry, suggests that standard deviations greater than the values stated above strongly indicate substantial intra-batch variability rather than systematic error in obtaining values.

c. Intrabatch Variability

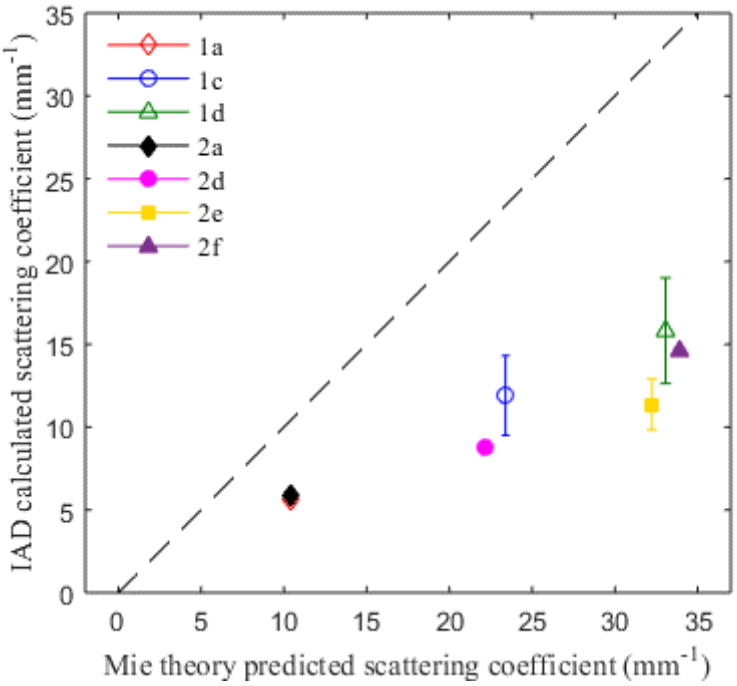

Figure 26. *Mean with error bars +/- 1 standard deviation for 7 phantom batches where 2 or more phantoms were made and measured. The ideal situation of Mie predicted = IAD calculated is also shown.*

Figure 26 shows that when considering only phantoms made using Method 2, Batch 2f shows least deviation from the mean, 14.6+/- 0.2 mm^{-1}(1.21%), whereas batches 2d, 2a and 2e all show an increasing standard deviation

from the mean, 8.7 +/- 0.3mm^{-1} (4%), 5.8 +/- 0.5mm^{-1} (8%) and 11.4 +/- 1.6mm^{-1} (14%) respectively. When looking at phantoms made using Method 1, batches 1c and 1d show a larger standard deviation, than all phantoms made using Method 2, of 20% (11.9 +/- 2.4mm^{-1} and 15.8 +/- 3.2mm^{-1} respectively), whilst batch 1a shows a much smaller deviation of 5.6 +/- 0.1mm^{-1} (2%).

d. Refractive index and Density Uncertainty

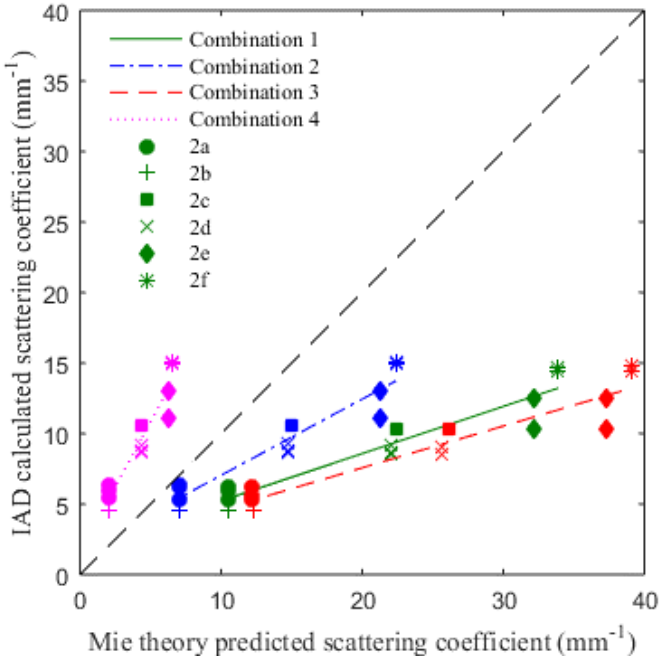

Figure 27. *The effect of varying sphere refractive index and density on the relationship between the predicted and measured values of μ_s made using Method 2. The dashed line shows the ideal situation of predicted = measured.*

Due to the density and refractive index ($n_{spheres}$) of the microspheres being unknown, the effect of this uncertainty was assessed by using different published combinations of density and refractive index throughout the Mie and IAD calculations (Table 3). Both values are used directly in Mie calculations, however $n_{spheres}$ effects the g value, which is used within IAD, therefore both are potentially affected by this uncertainty. Combination 1 represents the initial estimate, and was based on reference data for fused silica, combination 2 consisted of values used for the same brand (but different diameter) of microspheres in a study by Schnaiter et al.[193]. Finally, combinations 3 and 4 were taken from values quoted by Bangs laboratory

for their silica microspheres[194] (1.43 to 1.46 at 589nm). Figure 27 demonstrates how using different combinations of sphere refractive index and density can profoundly affect the relationship between the predicted and measured values of μ_s. Regardless of this change in relationship, it can clearly be seen that if considering any of the batches individually, the values predicted by Mie theory vary dramatically, up to 35mm^{-1}, whilst the values calculated by IAD have a much smaller distribution of less than 3mm^{-1}, with batches 2b, 2c, 2d and 2f varying by less than 1mm^{-1}. This shows that despite uncertainty in $n_{spheres}$, the IAD value of μ_s is reliable, and demonstrates the importance of measuring μ_s rather than relying on predictions if such uncertainties exist.

Combination	ρ (g/ml)	$n_{spheres}$	g
1	2.203	1.4584	0.9533
2	1.900	1.3700	0.9546
3	2.000	1.4600	0.9532
4	2.000	1.4300	0.9544

Table 3 *Combinations of refractive index (n) and density (ρ) of spheres that were considered, along with the value of g obtained with the value of n stated.*

6.2.3.4. Discussion

Significant microsphere aggregation in phantoms made using Method 1 was seen in OCT and x-ray microscopy images, and the unreliable calculated μ_s values were demonstrated using the spectrophotometer results and IAD programme. The increased intra-batch variability in IAD calculated μ_s values of Method 1, compared to Method 2, is due to the greater degree of aggregation seen. The number, size and morphology of aggregates is random, creating areas of higher and lower sphere concentration within the same phantom, however this does not average out to an overall sphere density when scattering is considered. The Mie theory calculations used to design the phantoms and predict the value of μ_s assume a random arrangement of spheres within the phantom volume, which is not a valid assumption when aggregation occurs. This is the cause of the large intra-batch variability. When considering phantoms made by Method 2, a decreased standard deviation compared with Method 1 provides compelling

confirmation for the reduced degree of aggregation observed using x-ray microscopy and demonstrates the reliability of Method 2 for creating phantoms with consistent optical properties.

Despite uncertainties inherent to using microspheres (manufacturers commonly give a range of $n_{spheres}$ and density values rather than one specific value - a problem previously encountered by Diao et al.[142]) when considering individual batches made using Method 2, low variability in the IAD calculated μ_s across all 4 combinations of $n_{spheres}$ and density was demonstrated (Figure 27). As the actual value (IAD calculated value) of μ_s is more important than the predicted value, this stability despite uncertainty makes them a reliable choice of phantom when the application requires the value of μ_s to be known accurately. The uncertainty associated with the values of $n_{spheres}$ and density is the likely cause of mismatch between the Mie theory predicted and IAD calculated values of μ_s observed as both values remain unknown for the brand of spheres used throughout this study. However, the ideal, i.e. when the values of μ_s obtained using both Mie theory and IAD match, falls between the range of values quoted for a commonly used brand of microspheres (Figure 27 combination 3 and 4), therefore it is feasible that the correct value of $n_{spheres}$ lies between 1.43 and 1.46 with the density of the spheres=2g/ml. If a perfectly homogeneous distribution of spheres within the silicone was obtained, then this could be a reliable method of determining the value of $n_{spheres}$, however it should be noted, that a perfect match would not be expected for either the Method 1 or Method 2 phantoms due to the presence of aggregation in differing amounts. Regardless of the combination of properties used, the pattern in intra-batch variability between Method 1 and 2 remains the same, therefore, the conclusions drawn regarding degree of aggregation and reliability of the method remain the same.

The manufacturing process involved in Method 2 has a negligible effect on the intrinsic scattering properties of the silicone rubber, evident by the low measured values of μ_s in the plain silicone phantoms. It is not possible to say that there is no effect due to the non-zero value gained for one of the phantoms, however the intrinsic scattering induced by the manufacturing process is very small compared to the values obtained by adding silica microspheres and so can be ignored when designing and making phantoms with Method 2.

The swelling and subsequent shrinkage of the silicone observed during the development of Method 2 is strong evidence that the commonly stated assumption that hexane is evaporated before curing is not correct. Further work is needed to determine whether a different solvent that does not cause swelling may be more appropriate, for example Tert-butyl alcohol (TBA)[155], however as long as the swelling and, therefore, increased silicone volume caused by the hexane is taken into account within calculations, then it will not cause problems. It may be difficult to quantify the amount of hexane remaining at the point of curing so TBA may provide greater correlation between IAD and Mie values. It is important to state that although determining the correct combination of density and $n_{spheres}$, along with the effect of hexane on the silicone volume is pivotal to designing phantoms of known μ_s, it is not greatly important in determining the IAD values, arguably the more important of the two values, as these values are the actual, rather than theoretical optical properties.

Although not explicitly considered here, the absorption coefficient (μ_a) was negligible for all phantoms. This value was simultaneously extracted from IAD calculations along with μ_s. The highest calculated value of μ_a was $1.45 \times 10^{-3} mm^{-1}$ for phantom 0c at month 0 – if considering the Beer-Lambert law, this equates to a 0.0289% reduction in beam intensity over a 0.2mm distance, and therefore can be considered negligible and the phantoms considered scattering only.

Subsequent investigations using a different brand (AngstromSphere™ - Fibre Optic Center, MA, USA) of microsphere with a stated density ($1.8 gcm^{-3}$) and range of refractive index (1.38-1.46), demonstrated that a close match between Mie predicted and IAD measured values of μ_s can be achieved by using Method 2 as previously described. In this case, two phantom thicknesses were created, one, using the cast as shown in Figure 18 (creating a phantom of minimum thickness of 0.2mm), and another, thicker cast made using two number 2 coverslips as spacers, thereby creating a phantom of minimum thickness of 0.4mm. Both phantoms had their thicknesses determined after curing, using digital callipers, and the measured thicknesses (0.41mm and 0.50mm) were used in IAD calculations. The IAD measured value fell within the range of μ_s values expected given the range of $n_{spheres}$ values given by the manufacturer, with an $n_{spheres}$ value of $n_{spheres}$=1.445 at 589nm providing an almost perfect match between

calculated and measured values. It was noted however that by using a thicker phantom size (0.50mm), the standard IAD error of 0.0001 was able to be used, as opposed to the 0.1 error used in the thinner (0.41mm) phantoms (6.2.3.2. Objective Analysis - Spectrophotometer b. Inverse Adding Doubling (IAD)), therefore giving greater confidence in the IAD values calculated from the thicker sample, therefore future phantoms should be made at least 0.5mm thick. Although an excellent match was obtained, there were no further investigations using these spheres due to difficulties in reducing large macroscopic clumping as well as issues with supply, therefore alternative microspheres (Pinfire - Gems and Colloids, Frankfurt, Germany) were used from now on.

Thickness (mm)	$n_{spheres}$	g	IAD error input value	Mie predicted μ_s (mm^{-1})	IAD calculated μ_s (mm^{-1})
0.41	1.445	0.9539	0.1	13.8	11.1
0.50			0.0001		13.6

Table 4 *predicted and measured μ_s values for phantoms of differing thickness, showing the discrepancy due to the different errors of convergence using IAD.*

Method 2 was also successfully used to create silicone phantoms containing TiO_2 powder. The concentration of scattering particles within such phantoms was significantly lower than with silica microsphere phantoms, therefore aggregation was assumed to be less of a problem, and likely overcome by the methods adopted in Method 2. Subsequent determination of optical properties of these phantoms (6.3. Results – Phantom Optical Properties Determination) demonstrated the high predictability of scattering properties, and therefore the reliability of Method 2 in incorporating an alternative scattering material with minimal aggregation.

As discussed, silicone creates phantoms with controllable optical properties with negligible optical absorption, however the x-ray absorption of such phantoms is high, therefore alternative bulk materials were investigated to create scattering phantoms of lower x-ray absorption.

6.2.4. Agarose Phantoms

Agarose, an organic hydrogel, consisting mostly of water, entrapped within a polymeric matrix, is an extensively used phantom material due to its wide availability and cost effective nature[112,113]. Despite its fragility and ability to quickly desiccate if not stored correctly, it has found use in optical phantoms, in part due to its tissue like chemical composition and comparable water content[158,159,195], which can be adjusted dependent on use. Prior to pouring into casts, agarose is a liquid with the viscosity of water, therefore it has the potential to be cast into a variety of complex shapes, however the complexity of phantom shape must be weighed up against the fragility and storage requirements.

6.2.4.1. Materials and Methods

a. Phantom Materials

Phantoms were constructed using powdered agarose (Product A9539, Sigma Aldrich, Dorset UK), which was mixed, and heated with tap water, to produce a 2% hydrogel. The refractive index of the agarose ($n_{agarose}$) was not provided by the manufacturer, therefore 1.34[181] at 589nm was used, very similar to biological tissues such as cornea[196], skin and muscle[31].

b. Manufacture Method

Agarose phantoms were constructed using the method outlined in Figure 28, with the final hydrogel made up to be 2% agarose, as lower percentages created a phantom that was too brittle and prone to breakage with very gentle handling. This was done by adding the weight of agarose that corresponds to 2% of the mass of water used.

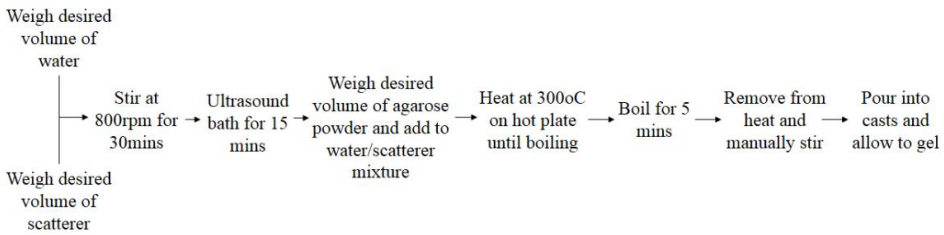

Figure 28. *Agarose phantom manufacture method.*

The low density of the agarose-water mixture, compared to the scatterers, caused the scattering particles to rapidly sink as soon as stirring ceased. This

was counteracted by adding in multiple stirring steps, as well as time in an ultrasound bath – both of which also act to break up any large aggregates.

After the final stirring step, the agarose is immediately poured into cold casts of multiple thicknesses, to encourage rapid gelation, trapping the scatterers in the matrix before they have a chance to settle out of the solution. Once manufactured, all agarose phantoms were kept at room temperature, submerged in water within sealed glass jars.

The agarose phantoms were not assessed for aggregation due to the relatively quick manufacture and fast gelation process (approximately 1 hour in total). Therefore, the discovery of aggregation would not lead to any changes in the method, as all modes of aggregation reduction had already been exhausted.

6.2.5. Gel Wax Phantoms

Gel wax is a highly cost effective and non-toxic, oil based phantom material, which does not require any specialist equipment for its preparation or storage. The organic nature of gel wax gives it a similar refractive index to tissues[177,182,197], and its optically clear nature means that all optical properties are tuned by the addition of external scatterers. Due to its relatively recent emergence as a phantom bulk material, only TiO_2 powder has been incorporated as a scatterer into gel wax[173,176,177], however there is no reason to believe that other inorganic scatterers could not be successfully incorporated. Aqueous scatterers should however be avoided as mineral oils are hydrophobic.

6.2.5.1. Materials and Methods

a. Phantom Materials

Phantoms were constructed using the mineral oil based candle wax material known as gel wax (Mindsets (UK) Ltd., Saffron Walden, UK) as the bulk material. The value of n_{gelwax}=1.4 was used, as gel wax is composed of mineral oil, which is a mixture of alkanes. Reported refractive index values at 589nm for a variety of alkanes, and their mixtures is approximately between 1.35 and 1.45[182], therefore 1.4 was used as an estimate.

b. Manufacture Method

The phantoms were manufactured using a modified version of the method presented by Maneas et al[173,174], and an outline can be seen in Figure 29. During stirring, the mixture is maintained at 250°C to prevent it from prematurely solidifying.

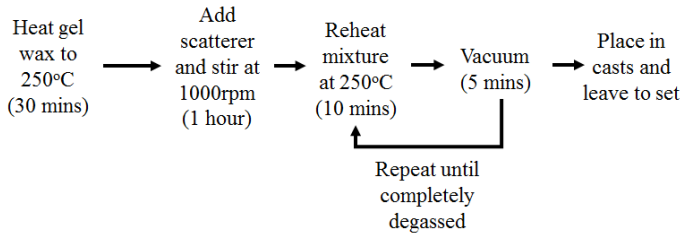

Figure 29. *Gel wax phantom manufacture method*

As with agarose phantoms, the scatterers have a high density compared to the gel wax, and therefore multiple stirring steps are incorporated into the method, to encourage homogeneous distribution of scatterers throughout the gel wax. The ultrasound bath cannot be used in this case as the gel wax immediately begins to solidify when removed from the hot plate and placed within the cooler ultrasound bath.

Gel wax phantoms were not assessed for aggregation due to the very short manufacturing process, leaving little opportunity to introduce methods to reduce aggregation. All suitable methods to reduce aggregation had already been incorporated (stirring), with use of an ultrasound bath inappropriate due to the cold temperature of the water in the bath causing instant solidification of the gel wax.

6.2.6. Casts

For each bulk material and scatterer combination, simultaneous manufacture of both x-ray phantoms of approximately 10mm, 6mm, 4mm and 2mm thickness, and multiple optical phantoms of between 0.5mm and 1mm (gel wax and silicone) or 1mm (agarose) thickness occurred. The 10mm x-ray sample was cast using a silicone ice cube tray, which had cuboid holes of 10x10mm, whereas all other x-ray casts were custom made from silicone rubber (Elastosil 601 RTV – Wacker Chemie, Munich, Germany), with the voids created using ever increasing stacks of microscope slides (approximate thickness of individual slides - 1mm) (Figure 30). The slides

were not individually measured at this point, however the thickness of all phantoms created from such casts was determined later using digital callipers, prior to x-ray or optical assessment to ensure that the accurate sample thickness could be accounted for during analysis. Once the phantom mixture had been poured into the casts, glass slides were placed on top, to create a flat surface and prevent the formation and setting of a meniscus. To enable the creation of silicone x-ray phantoms, a release spray (Ambersil Formula 5, CRC Industries UK Ltd., Somerset, UK) was used to aid release of the phantoms from the silicone casts. This was also sprayed on the slides that were placed on top of the x-ray phantoms, however this could not be used for the optical phantoms as the spray left visible marks on the phantom.

As previously described (Figure 18), the optical casts for silicone and gel wax phantoms were manufactured from two soda lime glass slides, however this time, a thicker phantom was required, therefore two stacked number 2 coverslips were used at each end as spacers between the slides. This method of casting created optical phantoms of approximate thickness between 0.5mm to 1mm, specifically designed for use within the spectrophotometer (Perkin Elmer, Lambda 750, dual beam with 100mm single integrating sphere accessory). Unlike the silicone phantoms, the gel wax optical phantoms were left between the 2 slides they were initially cast between and were not remounted due to the fragility of such a thin film of gel wax. As gel wax begins to set immediately on contact with a cool surface, the slides used for the optical phantom casts, as well as those placed on top of the x-ray phantoms to prevent meniscus formation, were heated to aid casting. Due to the brittle nature of agarose, optical phantoms were made to be approximately 1mm thick, using the custom-made silicone casts, as this gave adequate strength, without excessive thickness, which would make transmission and reflectance measurements via spectrophotometry difficult. The low viscosity of the agarose prior to curing also precludes the use of the slide-based casts.

This method of simultaneous casting, from the same batch of phantom material, created samples that were of identical scatter-bulk material composition and concentration, but specifically designed for 2 different measurement purposes.

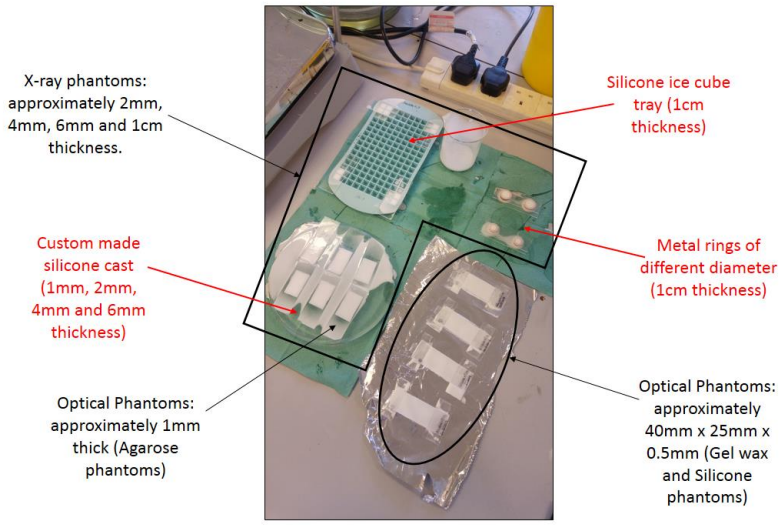

Figure 30. *Casts for creating x-ray and optical phantoms.1cm rings were explored as phantom casts, but were deemed to be an unsuitable shape, so were not considered further. Image depicts casting of silicone and TiO_2 phantoms.*

6.3. Results – Phantom Optical Properties Determination

The optical properties (primarily μ'_s) of the optically scattering phantoms created in Chapter 5, were determined at 589nm by spectrophotometry. The values of μ'_s were initially used to assess the reliability of each of the phantom making methods as well as the long-term stability of the manufactured phantoms, and latterly to refine the x-ray imaging and retrieval methodology (to be discussed in Chapter 8).

I note here that section 6.3.2. Optical Stability is based upon work I published as first author[3]

6.3.1. Spectrophotometer and the Inverse Adding Doubling Program (IAD)

The reduced scattering coefficient (μ'_s) of each of the optical phantoms was determined at 589nm using the previously described dual beam single integrating sphere spectrophotometer (Perkin Elmer® Lambda 750 Dual beam spectrophotometer) along with the IAD method (as described previously in Section 6.2.3.2. Objective Analysis - Spectrophotometer), however this time the sample reflectance and transmittance were measured over a narrower wavelength range of 580nm to 600nm. The reduced scattering coefficient was considered from here on in, rather than the

scattering coefficient. This was done firstly due to the greater relevance to biological tissues. Secondly, the use of multiple bulk material and scatterer combinations, each with different g values, made considering the directionality of scatter along with the scattering coefficient more appropriate. The wavelength of 589nm was considered, because the optical properties of both the silicone and silica microspheres were only provided by the manufacturer at this wavelength. Calibration measurements for both 100% and 0% reflectance and transmittance were made in line with recommendations from the literature[26], and dual beam corrections were applied. Due to losses during the manufacturing processes, each batch contained a variable number of phantoms within it (Table 6), however, at least 2 phantoms per batch were used to determine the final μ'_s of each scatterer concentration.

6.3.1.1. IAD Input Parameters

Table 5 states the g and n_{sample} values for each phantom type, both used as inputs to IAD, with n_{sample} estimated to be that of the phantom bulk material. The refractive index for TiO_2, gel wax and agarose are based on literature values[182,183,198], whereas the values for silica and silicone were provided by the manufacturers[180]. The precise g value for the silica and silicone phantoms, and the estimated g value for all other silica microsphere containing phantoms were calculated using Mie theory[33]. An estimate for g was used for silica microsphere and gel wax or agarose phantoms due to the uncertainty in n values for both bulk materials, therefore use of an exact g value was inappropriate. The g value for all TiO_2 containing phantoms was based partially on literature values for the same brand of TiO_2 powder embedded in silicone[199], but also estimated using Mie theory by assuming spherical particles of diameter between 1 and 5μm.

	Silica Spheres	TiO_2 powder
Silicone	g=0.9529 n_{sample}=1.409 n_{silica}=1.467	g=0.7 n_{sample}=1.409 n_{TiO2}=2.5082
Gel Wax	g=0.9 n_{sample}=1.4 n_{silica}=1.467	g=0.7 n_{sample}=1.4 n_{TiO2}=2.5082
2% Agarose	g=0.9 n_{sample}=1.34 n_{silica}=1.467	g=0.7 n_{sample}=1.34 n_{TiO2}=2.5082

Table 5. *Optical properties of each bulk material and scatterer combination, as used in IAD.*

Finally, the thickness of the fully mounted samples (i.e. the total thickness of the 'slide – sample – slide') was determined via the mean of five digital calliper measurements of each phantom, and this value (minus the thickness of 2 slides) was also used as input in the IAD. As previously discussed, (6.2.6. Casts), the individual thickness of the microscope slides used to mount the phantoms was not determined, however, error introduced into the IAD calculations was assumed to be negligible.

6.3.1.2. Sample Preparation

Gel wax and silicone phantoms do not require any additional preparation before being analysed by the spectrophotometer, as they are stored sandwiched between two glass slides. The agarose phantoms, however, require mounting between slides immediately prior to measurement. To do this, a drop of tap water was placed on the bottom slide, with the agarose sample placed on top. A further water droplet was then placed on the agarose sample, and the second slide placed on top of this. Once an air free contact was visually confirmed, the two slides were then held in place with Sellotape and labelled clearly using a permanent marker. After acquiring the measurements, the thickness of the samples was determined as previously described, and then the slides were removed to allow the sample to be submerged back in water for storage.

6.3.1.3. Results

The phantoms made using TiO_2 powder particles are unable to be modelled using Mie theory, because of the lack of accurate data regarding the refractive index of the gel wax, agarose and the TiO_2, as well as the uncertainty surrounding the size and shape of the particles. Therefore, multiple 'test phantoms' with accurately determined masses of both scatterer and bulk material were created and their μ'_s values determined via spectrophotometry (Figure 31). The quantities of scatterer used within the test phantoms was determined by visual inspection, adding a measured quantity until a suitable shade of white was obtained. The measured μ'_s was then plotted against the % scatterer by weight, with the line of best fit, and its equation, subsequently used to design phantoms of desired μ'_s (final phantoms), the value of which was confirmed via spectrophotometry.

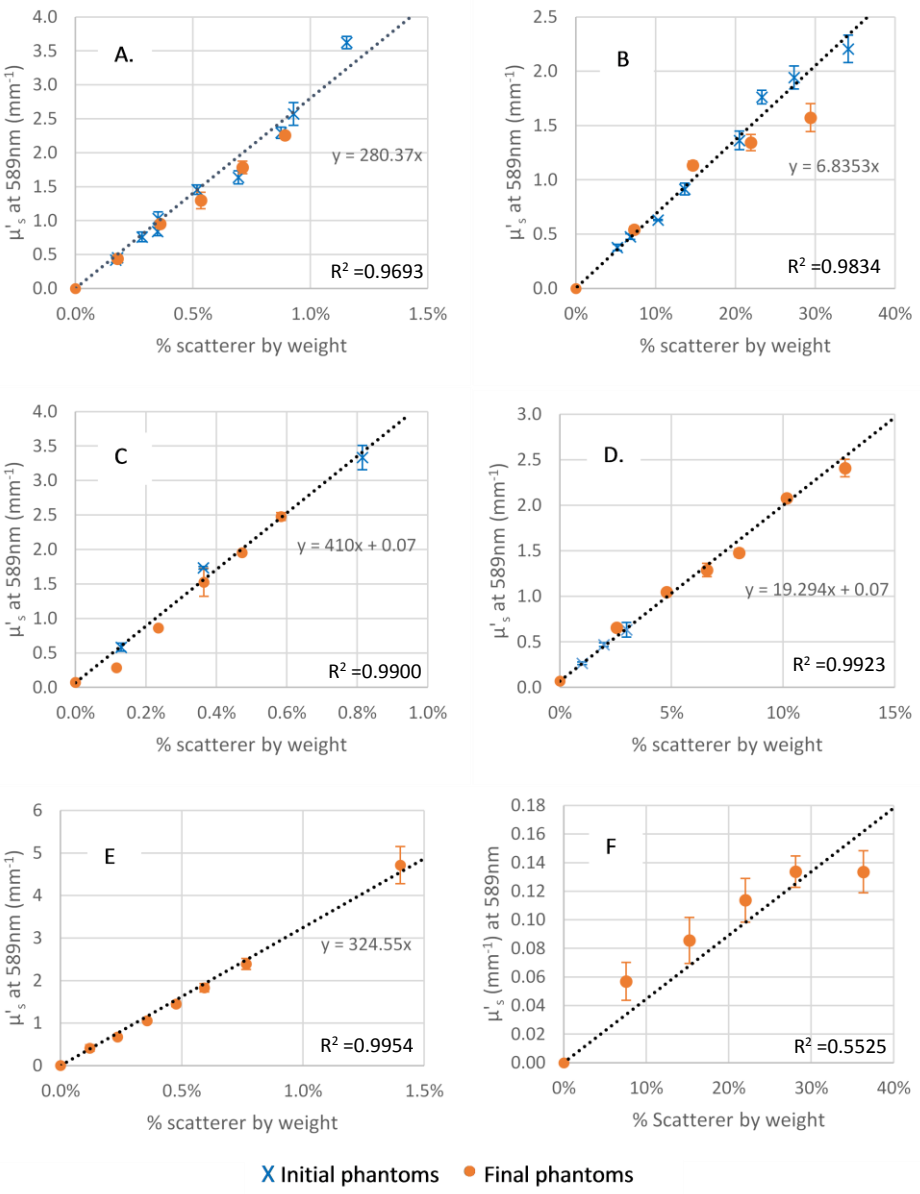

Figure 31. *The initial measured μ'_s values, created by varying the % scatterer by weight in the phantoms for A. Gel wax and TiO_2, B. Gel wax and silica microspheres, C. Agarose and TiO_2, D. Agarose and silica microspheres, E. Silicone and TiO_2 and F. Silicone and silica microspheres. Error bars show +/- 1 standard deviation. The relationship between % scatterer by weight and μ'_s that were used to design the final phantoms, are shown on the graphs, except for silica and silicone (F) as Mie theory was used to design these. No 'test phantoms' can be seen for TiO_2 and silicone (E) as the relationship was initially estimated from the most scattering phantom, and then refined with each phantom made – all phantoms made were used in subsequent x-ray and optical analysis. The R^2 values of the relationships derived from the initial 'test phantoms' are also displayed.*

The scatterer concentration was recorded as '% scatterer by weight'. This represents the ratio of the initial mass of scatterer compared to either the initial mass of silicone part A, the mass of gel wax, or the mass of water used in the manufacture of silicone, gel wax or agarose phantoms respectively. All mass measurements were made using a high precision balance (to 4 decimal places) at the start of the manufacture process, and it was assumed that the concentration remained unchanged by the phantom manufacturing process, however no attempt to verify this were made. The linear relationships seen in Figure 31 demonstrate the reproducibility of the phantom manufacturing methods, as they consistently create phantoms with μ'_s values that may be accurately predicted with knowledge of the % scatterer by weight. This reproducibility is assessed after noting the high R^2 values of greater than 0.96 for the line of best fit of all phantom combinations except those made of silicone and silica microspheres. R^2 is calculated by Matlab, known as the coefficient of determination. The coefficient of determination (R^2), is a 'goodness of fit' statistic, and is a measure of how well the linear model describes and is therefore able to predict the dependent variable (in this case μ'_s) using the independent variable (% scatterer by weight). Values closer to 1 demonstrate a good ability of the relationship to describe, and therefore predict, the μ'_s values. The reason for the lower predictability of μ'_s values for silicone and silica microsphere phantoms, as demonstrated by the low R^2 value, is currently unconfirmed, however, it is suspected in part to be due to the high concentration of scatterer required (up to 40% scatterer by weight), increasing the likelihood of electrostatic interaction due to the proximity of the particles. Furthermore, such a high concentration of scatterers may invalidate the model used to compute the value of μ'_s. It should be noted that the μ'_s value for the plain silicone and gel wax are both $0mm^{-1}$, whereas the plain agarose shows intrinsic scattering, with a μ'_s of $0.07mm^{-1}$. Silicone and gel wax are both homogeneous polymeric materials, whereas, agarose is a hydrogel, with large water filled pores within it. A 2% gel has been shown to have 100 to 200nm diameter pores[200], therefore detectable scattering is expected. The final phantoms for each phantom material combination are displayed in Table 6. The final phantoms are those which were subsequently measured for x-ray scattering.

Bulk Material	Scatterer	Batch Name	Number of optical phantoms	% scatterer by weight	Initial measured μ'_s at 589nm (mm^{-1})
Silicone	Silica Microspheres	1A	5	7.57%	5.69×10^{-2}
		1B	4	28.11%	1.34×10^{-1}
		1C	7	15.24%	8.56×10^{-2}
		1D	5	22.03%	1.14×10^{-1}
		1E	4	36.34%	1.34×10^{-1}
	TiO_2 powder	2A	5	0.12%	0.41
		2B	4	0.23%	0.68
		2C	5	0.36%	1.05
		2D	4	0.48%	1.45
		2E	4	0.59%	1.83
		2F	5	0.77%	2.39
		2G	3	1.40%	4.71
Agarose (2%)	Silica Microspheres	3A	2	2.54%	0.66
		3B	2	4.79%	0.98
		3C	2	8.03%	1.41
		3D	2	10.17%	2.08
		3E	2	12.77%	2.41
		3F	2	6.59%	1.16
	TiO_2 powder	4A	2	0.12%	0.29
		4B	2	0.24%	0.86
		4C	2	0.36%	1.53
		4D	2	0.47%	1.95
		4E	2	0.58%	2.48
Gel Wax	Silica Microspheres	5A	4	7.32%	0.54
		5B	4	14.65%	1.13
		5C	4	21.94%	1.34
		5D	4	29.42%	1.57
	TiO_2 powder	6A	4	0.18%	0.44
		6B	4	0.36%	0.95
		6C	4	0.53%	1.30
		6D	4	0.71%	1.78
		6E	4	0.89%	2.26

Silicone	None	Silicone	5	0%	0.00
Agarose (2%)		Agarose	2	0%	0.07
Gel Wax		Gel Wax	4	0%	0.00

Table 6. *Number of optical phantoms manufactured for each scatterer concentration.*

All phantoms were designed with biologically relevant μ'_s values at 589nm, and therefore were kept at a μ'_s of 5mm^{-1} or lower [20,31]. For silicone and silica microsphere phantoms, Mie theory was used to design the phantoms rather than the relationships displayed in Figure 31, however, despite the expected accuracy of Mie theory in designing these phantoms there was a mismatch between the designed, and the measured values of μ'_s (Table 7). This mismatch is suspected to be a result of phantoms not adhering to the assumptions required to employ Mie theory to calculate μ'_s. Despite the careful application of the manufacturing protocol, developed specifically to reduce the aggregation of microspheres (6.2.2.5. Method 2 – Overcoming Aggregation), it is suspected that such phantoms still contain aggregates of microspheres due to the high scatterer concentration required (up to 40%). Mie theory works to model optical scattering caused by a known concentration of discrete spheres of known refractive index and size, and therefore does not account for the suspected aggregation within these samples. Furthermore, and regardless of the aggregation status, inaccurate knowledge of the refractive index of the microspheres by the manufacturer limits the accuracy of Mie theory. Such limitations are the reason why μ'_s values are less biologically relevant for the silicone and silica microsphere phantoms. From now on, the μ'_s stated is the spectrophotometer measured value, and not the value designed using either Mie theory or the derived relationships displayed in Figure 31.

Sample Name	Mie designed μ'_s at 589nm (mm^{-1})	Spectrophotometer measured μ'_s at 589nm (mm^{-1})
1A	0.492	0.057
1B	1.659	0.134
1C	0.953	0.086
1D	1.336	0.114
1E	2.068	0.134

Table 7. *Mie designed, and spectrophotometer measured μ'_s values at 589nm for all silicone and silica microsphere phantoms.*

It should be noted that, when calculating μ'_s the standard IAD error of 0.0001 was stipulated for all phantom batches as input to the program[26], except 1A-1E and 5A (Table 6) , where 0.1 was used. A lower error was unable to be used for these phantoms due to the very high transmission and low reflectance caused by low scattering. The effect of a high IAD error value in determining the μ'_s values of low scattering phantoms was assessed by running the IAD program with five different error values, from the standard error of 0.0001 to the high error of 1 for all four 5A phantoms. The μ'_s value for each phantom at each IAD standard error was recorded, and the variation in data assessed (Table 8). The difference in calculated μ'_s for the five error values was highest for phantom 5A-1 and lowest for 5A-4 with variations of $0.035mm^{-1}$ and $0.022mm^{-1}$ respectively. These values are sufficiently low enough to assume that the effect of the high IAD error value on the calculated μ'_s is negligible, and therefore does not affect the conclusions drawn latterly for the stated low scattering phantoms. More importantly, if the value of 5A is calculated by taking the mean of all phantoms at each individual error value, the μ'_s value for 5A remains at $0.54mm^{-1}$ regardless of the error used.

IAD error value	μ'_s (mm^{-1}) at 589nm				
	5A-1	5A-2	5A-3	5A-4	Mean
1	$5.51X10^{-1}$	$5.59X10^{-1}$	$4.97X10^{-1}$	$5.66X10^{-1}$	$5.43X10^{-1}$
0.1	$5.51X10^{-1}$	$5.60X10^{-1}$	$4.98X10^{-1}$	$5.68X10^{-1}$	$5.44X10^{-1}$
0.01	$5.21X10^{-1}$	$5.82X10^{-1}$	$5.12X10^{-1}$	$5.46X10^{-1}$	$5.40X10^{-1}$
0.001	$5.17X10^{-1}$	$5.82X10^{-1}$	$5.13X10^{-1}$	$5.50X10^{-1}$	$5.40X10^{-1}$
0.0001	$5.17X10^{-1}$	$5.82X10^{-1}$	$5.24X10^{-1}$	$5.48X10^{-1}$	$5.43X10^{-1}$

Table 8. *μ'_s values calculated for different IAD error values for all phantoms consisting of silica microspheres and gel wax.*

6.3.2. Optical Stability

Results reported in this subsection of work were published in Biomedical Optics Express: Jones CJM, Munro PRT. Stability of gel wax based optical scattering phantoms. *Biomed Opt Express*. 2018;9(8):3495–3502. Published 2018 Jul 2. doi:10.1364/BOE.9.003495

To determine the temporal stability of the optical properties, the μ'_s value of the oldest batch of each of the scatterer-bulk material combination (1A, 2G, 3C, 4E, 5A and 6E - Table 6) was periodically measured over an approximate 2 year time span. The values for each of these batches was considered representative of all other phantoms of the same composition, and therefore an indication of the stability of that phantom composition. This measurement gathers importance when phantoms are designed to be used over a prolonged period, as it is imperative that their properties remain consistent.

6.3.2.1 Results

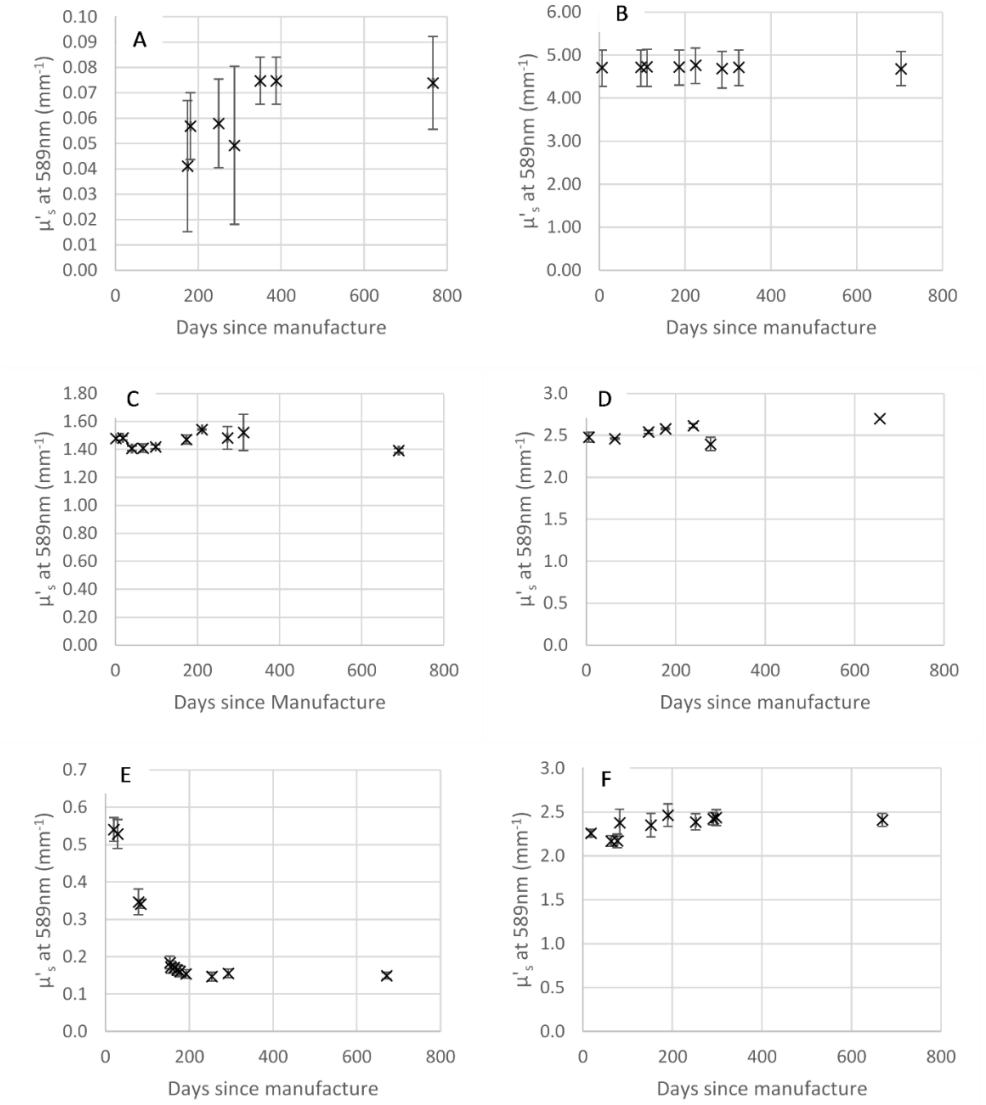

Figure 32. *μ'_s values over time for batches A. 1A (silica microspheres and silicone), B. 2G (TiO_2 powder and silicone), C. 3C (silica microspheres and agarose), D. 4E (TiO_2 powder and agarose), E. 5A (silica microspheres and gel wax), F. 6E (TiO_2 powder and gel wax). Error bars displayed are +/- 1 standard deviation.*

Figure 32 shows that for all phantom types, except for the one made of gel wax and silica microspheres (phantom 5A), the value of μ'_s remains stable over time. Although small observable differences are noted over the measurement period, these are mostly within the accepted error of +/- 1 standard deviation.

Figure 32B shows the high stability of μ'_s for phantom 2G (TiO_2 and silicone) over a prolonged period, and therefore, for the purposes of temporal scattering stability, can be considered as the 'gold standard'. The high stability of the scattering also means that these phantoms can be used as a control for the measurement technique, with significant changes in μ'_s attributed to measurement error as opposed to phantom instability.

Phantom 1A suggests a possible general upward trend in μ'_s over time. The trend however, is hard to assess due to the large uncertainty with these results, especially for values within approximately the first 300 days, demonstrated by the large error bars in Figure 32A. The instability seen was deemed acceptable, and most likely due to error within IAD rather than physical change within the phantoms - as previously discussed, the very low scattering by this batch of phantoms creates an innate error within the generated μ'_s.

Both agarose phantoms exhibit impressive stability over a prolonged time period, especially as agarose is typically considered a short term phantom material[112,113]. For the final displayed value, only one phantom was measured for batch 4E due to severe degradation of the samples. Visually, batches 3C and 4E had significantly deteriorated for the final measurement (at approximately 2 years post manufacture), with the samples having become extremely brittle. This change was attributed to evaporation of the water in which they were stored, leading to dehydration of the samples. Despite this visual assessment, the change in μ'_s from initial to final measurement was modest for both batches, and there was no discernible pattern in the change in μ'_s values over time, suggesting that the differences in measurement were due to systematic error rather than any progressive change in the samples over time.

Phantom 5A, is the only phantom which displays significant optical instability, demonstrating a significant decrease in μ'_s values of over 50% its original value over the two-year time period. To determine a trend in the instability, the μ'_s for all gel wax phantoms (batches 5A-5C and 6A-6E) was periodically determined.

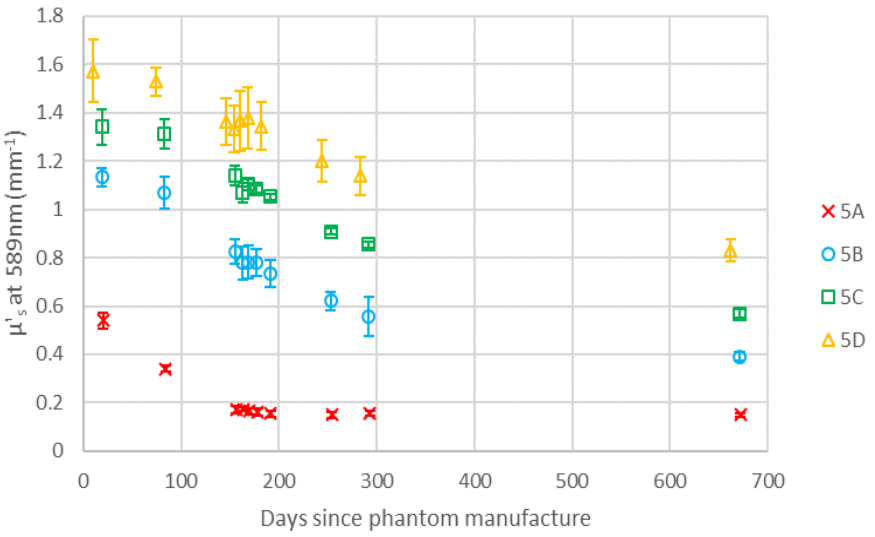

Figure 33. *μ'_s value over time for all gel wax and silica microsphere phantoms. Error bars show +/- 1 standard deviation.*

Figure 33 shows that μ'_s decreases over the period studied for all gel wax and silica sphere phantoms, regardless of their scatterer concentration. It can be observed that the scattering coefficient of the phantom with lowest concentration of spheres (5A) plateaued after approximately 150 days post manufacture, however the final μ'_s value is over half that of the initial value. All other phantoms with higher sphere concentrations (5B, 5C, 5D) continue to decrease, with (for example) the measured μ'_s value of 5B decreasing to approximately 65% of its initial measurement over the 671 days since manufacture. On visual inspection there were no obvious signs of degradation (for example discolouration), however clumping was visible from 10 months, however this observation is subjective.

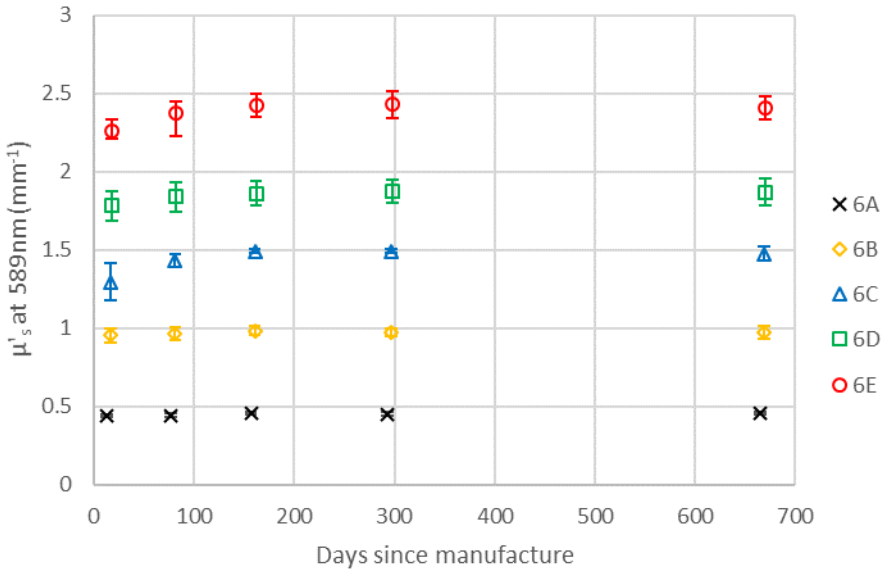

Figure 34. *μ'_s values of gel wax and TiO_2 powder phantoms over time. Error bars show +/-1 standard deviation.*

Figure 34 shows that the μ'_s values remain stable for gel wax and TiO_2 phantoms of all scatterer concentrations over the time measured. There are observable differences with each measurement, however these differences are small, and, as with other phantom material combinations (Figure 32) are mostly within the accepted uncertainty (+/- 1 standard deviation) of the previous measurement, however the phantoms are not as stable as the gold standard of silicone and TiO_2 previously discussed. The value of μ'_s slightly increases from the initial to the final measurement, with this increase most apparent over the first 100 days, especially in the 3 highest concentration phantoms (6E, 6D and 6C). The greatest increases are seen with phantoms 6C and 6E, which show an approximate 14% and 7% increase respectively, from the initial to the final measurement. All other phantoms show an increase of less than 5%, well within the estimated uncertainty of the measurements.

6.3.3. Discussion

The silicone and silica microsphere phantoms should be simple to design due to the ability to model microspheres using Mie theory. Modelling relies on the accurate knowledge of the refractive index of both the silicone and spheres, as well as the diameter and size distribution of the microspheres, all of which can often (but not always) be obtained from the manufacturer.

However, uncertainty in these values can occur due to the method by which they were measured, which is often unknown. In this case the uncertainty in the silica microsphere refractive index value is the cause of the discussed mismatch between Mie designed, and spectrophotometer measured μ'_s values – thus highlighting the importance of measuring the μ'_s rather than using the Mie calculated values. This problem has been previously noted in section 6.2.3.4. Discussion, where it was discussed with respect to earlier manufactured phantoms

With regards to the potential instability of phantom batch 1A, although the final measurement demonstrates a 79% increase on the initial value of μ'_s, this represents an actual increase of 0.033mm^{-1} from 0.041mm^{-1} to 0.074mm^{-1}. This is insignificant in terms of scattering properties, and within the difference displayed by the 'gold standard', 2G, which varies by a maximum of 0.083mm^{-1} over the 2-year period, with the final measurement of 2G showing a 0.032mm^{-1} increase from the start.

Although agarose is typically considered a short-term phantom material, it has the potential to be used long term with appropriate, but not specialist, storage conditions, such as complete submersion in water. Although all agarose phantoms were kept in sealed containers, submerged in tap water, evaporation from the non-air tight containers caused the water level to drop below the phantoms leaving them susceptible to dehydration. As the water content of the agarose reduces, the refractive index of the bulk material of the phantoms is likely to change, therefore potentially affecting the scattering properties of the final phantoms, however, even with this dehydration, the change in μ'_s over time was modest. The reason for this modest change could also be in part explained by the difficulty in mounting the agarose samples for spectrophotometry. The air free contact between the agarose and the overlying glass slides is maintained by water, the thickness of which is unable to be controlled, and will vary from measurement to measurement. The addition of an unknown volume of water during mounting also creates two, instead of one boundary of refractive index mismatch (i.e. slide to water then water to phantom instead of slide to phantom seen with all other bulk materials). Both issues can explain the small, and unpredictable, variation in μ'_s seen over time, and therefore the stability of agarose phantoms can be considered acceptable and due to systematic error. Finally, it is suggested

that, with proper storage to prevent dehydration, the long-term use of agarose phantoms is precluded by their fragility, and gradual destruction from handling for repeated measurements rather than the instability of their optical properties. The benefits of repeat measurement must be balanced against the disadvantage of gradual phantom destruction, and due to the fragile nature of the phantoms, it was decided that it was appropriate to continue to monitor the stability of agarose phantoms using batches 3C and 4E, and only redefine the μ'_s values for all other batches if a clear change in μ'_s was seen, which did not occur over the measurement period considered.

The structure and precise chemical composition of gel wax is unknown, however it is known that it is composed of a mineral oil (for example paraffin oil) along with polymer resin, which allows the normally liquid oil, to set into a soft gel material. It is therefore proposed that the mechanism by which μ'_s reduces over time in the gel wax and silica microsphere phantoms is due to the non-polar, semi-solid/gel like nature of the gel wax allowing the charged silica spheres to migrate through the matrix over time. Silica spheres have a predisposition to clumping due to electrostatic charge interactions between them[141]. When held in a solid matrix such as silicone, the particles are unable to move, and remain homogeneously dispersed throughout, evident by the reasonable stability seen with the silicone-silica microsphere phantoms, however, when the viscosity of the mixture is reduced (as with gel wax), the spheres can slowly move towards each other, and this aggregation therefore worsens over time.

The gel wax and silica sphere phantoms with the lowest concentration of spheres (5A) reached a plateau with their μ'_s value after approximately 150 days. As the concentration of spheres increases, the likelihood of aggregation also increases since the spheres are much closer to each other, and therefore, are more likely to undergo a charge interaction and aggregate. It would be expected that, eventually, aggregation will reach a maximum due to the distance between neighbouring spheres increasing as spheres migrate, and aggregation occurs, therefore leading to the value of μ'_s plateauing for all the sphere concentrations. However, after almost 2 years, this time has not yet been reached for phantoms of higher scatterer concentration.

Titanium dioxide particles tend towards aggregation due to Van der Waals forces[201] that can form between them when they come into close proximity. The '% scatterer by weight' values for gel wax and TiO_2 are below 1% for all phantoms, therefore the physical distance between the TiO_2 particles means that the likelihood of such Van der Waals interactions and therefore aggregation is low. If the concentration of TiO_2 were to be significantly increased, then a similar decrease in μ'_s may be observed, however, at concentrations required to obtain tissue realistic scattering coefficients, they appear to be reasonably temporally stable, although silicone and TiO_2 phantoms continue to be the gold standard in terms of long-term optical stability.

Due to the instability of scattering properties in the gel wax and silica sphere phantoms, it is therefore not appropriate to repeatedly use the same gel wax and silica microsphere phantoms over a prolonged period, without re-measuring the optical properties. Although gel wax and TiO_2 phantoms offer much greater optical stability, it would still be prudent to determine the optical properties before each use, as there is a small variation in measured values over time.

Monitoring the six chosen representative batches provides a time effective method of monitoring the optical properties of each of the phantom mixtures. It also strikes a balance, by providing the peace of mind that the μ'_s values can still be considered that of the initial measurement, whilst increasing the life of the phantoms by minimising handling, and therefore potential damage.

6.4. Conclusion

The correlation between the designed and measured μ'_s values for phantoms of all bulk material-scatterer combinations (except those of silica microspheres and silicone) demonstrates the excellent reproducibility and reliability of the presented manufacturing methods. Silicone and silica microsphere phantoms should be able to be designed using Mie theory, however lack of correlation between predicted and measured μ'_s demonstrate the uncertainties of using such a method, therefore Mie theory should not be relied upon to design such phantoms when uncertainties in the physical properties of the sample exist.

One of the design criteria for imaging phantoms may be their stability over a period of weeks to years. Gel wax is an affordable and simple phantom material, however the temporal instability of silica microsphere containing phantoms may preclude its use if long term stability is a key requirement of phantom design. Silicone and TiO_2 phantoms provide the greatest stability and should be considered the current gold standard when temporally stable optical phantoms are required, however all other phantom types show good long-term stability, and adequate stability for the purposes of the work presented in this thesis.

7. Optical Measurement of Biological Tissues

7.1. Optical Coherence Tomography (OCT)

7.1.1. Introduction

To this point, the combination of a spectrophotometer and IAD have been used to calculate the optical properties of the phantoms. However, this method requires the samples to be relatively thin, of uniform thickness and large enough to cover the transmittance and reflectance ports on the spectrophotometer's integrating sphere. Biological samples may be difficult to cut into such thin slices, therefore an alternative method, capable of use with irregular, thick samples that will not require specialist mounting techniques was developed. Optical coherence tomography (OCT) has been used previously to determine the scattering properties of biological tissues, for example human burn scars[9], axillary lymph nodes[10] and the cervix[202], and therefore this method was explored as a way to obtain accurate optical properties from *ex vivo* animal tissues. This method also provides a simple method to measure a spatially varying scattering coefficient, irrelevant in homogeneous scattering phantoms, but of importance when heterogeneous biological tissues are considered.

7.2. Materials and Methods

7.2.1. Data acquisition method

A Thorlabs Telesto II Spectral Domain OCT Imaging system (Thorlabs GmbH, Munich, Germany), with central wavelength of 1300nm was used to obtain the OCT images. The sample was placed on the sample stage, which is capable of fine movement in the x, y and z directions, and the x and y position adjusted until the image was centred on an area of interest. The fine and coarse focus was adjusted so that the focal plane was just below the upper surface of the sample, and the reference arm position was adjusted so that the upper surface of the sample was at the top of the displayed image. A C-scan was acquired, consisting of 500 x 500 A scans, with the total A-scan depth over which signal was obtained dependent on the sample being imaged, but typically being in the region of a few millimetres. To enable subsequent imaging of multiple samples, ideally the reference arm position, as well as the fine and coarse focus would be left in position, and samples

would be brought into focus by adjusting the z position of the sample stage. This is to ensure that the focal plane remains constant, and therefore the effects of the system can be corrected for adequately via the use of a low scattering 'calibration phantom'. This was performed for all biological samples as well as the 'irregular phantom', however the z translational sample stage was not available prior to this, and therefore for the silicone and TiO_2 phantoms, the reference arm length was kept constant between samples, and the fine and coarse focus adjusted so that the focal depth was kept as consistent as possible throughout.

7.2.2. Calibration phantom design

Previous methods required the use of a very low scattering calibration phantom, to correct for parameters inherent within the OCT system, such as the confocal response[9,10], therefore a calibration phantom was adopted here. The phantoms are required to be scattering only, and also have a low μ'_s value, therefore phantom batch 2A, which was constructed of silicone and 0.12% TiO_2 powder by weight (Table 6), and had a μ'_s and μ_t values of 0.42mm^{-1} and 1.322mm^{-1} respectively, and estimated g=0.7, all measured at 1300nm, was initially used. Latterly, where a lower scattering sample was required, a liquid phantom consisting of Polybead® polystyrene microspheres (Cat. Number 07307-15, Polysciences, Inc., Hirschberg an der Bergstrasse, Germany) suspended in water was used. The microspheres were of mean diameter 0.51μm +/- standard deviation of 0.01μm and had a coefficient of variance 2%. The purchased concentration of 2.6% solids, corresponding to a μ_t of 9.47mm^{-1} and g of 0.4849 at 1300nm, was diluted with distilled water to reach the desired concentration of spheres, creating a μ'_t of approximately 0.1mm^{-1}, as calculated using Mie theory. The phantom mixture was made on the same day as the imaging was to take place to help ensure that the microspheres did not have time to aggregate, however, the spheres were always vigorously pipetted into the imaging vessel to mix the sample. The calibration phantom was imaged immediately prior to imaging the samples, with the same system parameters used during image acquisition.

7.2.3. Data analysis method

Data analysis was performed in line with previously published methods[9,10],

with modifications to enable analysis of samples with irregular surfaces as follows. The data obtained directly from the OCT system for both the sample and calibration phantom is converted from dB to Intensity (I_{sample} and $I_{phantom}$ respectively). Irregular samples are unable to be physically aligned in a way that means the upper surface runs perfectly along the top of the OCT image. Therefore, the obtained data in which the surface of the sample is seen to be at different depths across the B scan, is subsequently processed to artificially align it prior to analysis. This is done by locating the peak of the strong backscatter created by the surface of the sample and discarding all superficial data prior to this point (Figure 35).

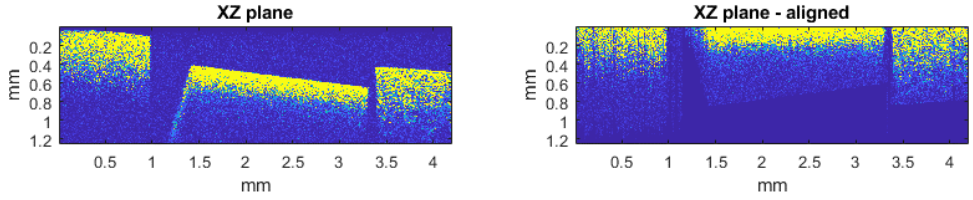

Figure 35. *Example of aligning an irregular sample to the top of the image. The image on the left shows the raw intensity data, and the right-hand image displays the aligned image, where the top of the sample now sits along the top of the image. Both images show 500 adjacent A scans.*

Once aligned, the image can be cropped to the area of interest, and the mean of all A scans within that area taken to create the sample profile *(I)*. All 500 x 500 A scans of the calibration phantom are used to create a single 'calibration profile', which is then used to create a 3D calibration image consisting of identical multiple (x by y, where x and y are the number of A scans of the sample in the x and y direction) copies of the calibration profile. The 3D calibration image is then adjusted so that the same number of superficial data points are discarded as the corresponding pixel's A scan in the sample image. This adjusted calibration image can then be cropped to the same area of interest as the image, and a mean taken to create the calibration profile *(I_0)*. The calibration profile can then be used to correct the sample profile

$$\log_e\left(\frac{I}{I_0}\right) = -2(\mu_t - \mu_0)z + C, \qquad \textit{Equation 36}$$

Where μ_t is the attenuation coefficient at 1300nm of the sample, and μ_o is the attenuation coefficient at 1300nm of the correction phantom as determined

by Mie theory (water and polystyrene spheres) or spectrophotometer and IAD (silicone and TiO_2 powder). The attenuation coefficient describes both the absorption and scattering of the sample and defines how light travels through the sample. If $\log_e\left(\frac{I}{I_0}\right)$ is plot against the A scan depth (z), which is corrected for the refractive index of the sample, then the gradient of the linear portion of the profile is equal to $-2(\mu_t - \mu_0)$, and the value of μ_t can be calculated. The fit is performed at a depth where the assumption of single scattering is valid.

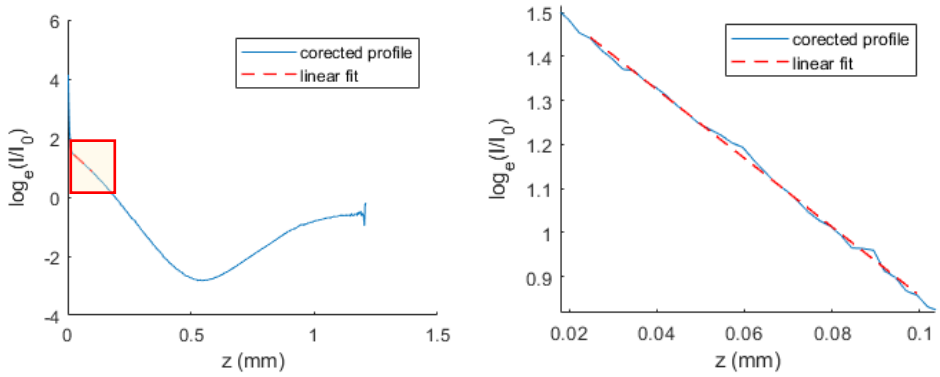

Figure 36. *Example profile, aligned to the top of the image, and corrected using the calibration phantom. The graph on the right depicts the linear fit to the boxed area of the left graph.*

To enable comparison between OCT and spectrophotometer or published data, the value of μ_t is converted to μ_s via previously published methods[10,60], with the calculated μ_s value similar to, but not identical to the μ_t value extracted directly from the OCT images. The value of μ_s is slightly higher than μ_t due to forward scattered light, which does not contribute to the OCT signal (and therefore the μ_t value), but is accounted for when converting the value to μ_s[10,60]. Finally, μ_s is converted to μ'_s via the relationship $\mu'_s = \mu_s(1-g)$.

In all OCT applications it is assumed that μ_t is dependent on μ_s within the single scattering region, and this has previously been validated by Almasian et al[203]. In the multiple scattering regime, the value of μ_t gains a dependence on the direction of scatter and therefore g, but is not identical to μ'_s (i.e. it is a more complex dependency on g), and this has also previously been validated[204].

7.3. Results

7.3.1. Silicone and TiO_2 phantoms

To validate the data collection and analysis methods, previously manufactured silicone and TiO_2 phantoms were imaged using the OCT system (samples 2B-2G - Table 6), with phantom 2A used as the low scattering calibration phantom. The $10mm^3$ phantoms, initially designed for x-ray imaging, were used, and the A scan depth was corrected for the refractive index of silicone[205] at 1300nm, which was estimated as 1.397. These samples have very flat upper surfaces, and therefore, this surface is grossly aligned to the top of the image during acquisition, meaning that minimal alignment is required during the analysis procedure. The fit was performed over a depth of at least 50 pixels (a region of at least 110µm) in the single scatter region for each phantom, estimated by taking the inverse of the spectrophotometer measured μ'_s. The value of μ'_s was also determined, as previously described, via spectrophotometer and IAD at 1300nm, with an estimated g of 0.7.

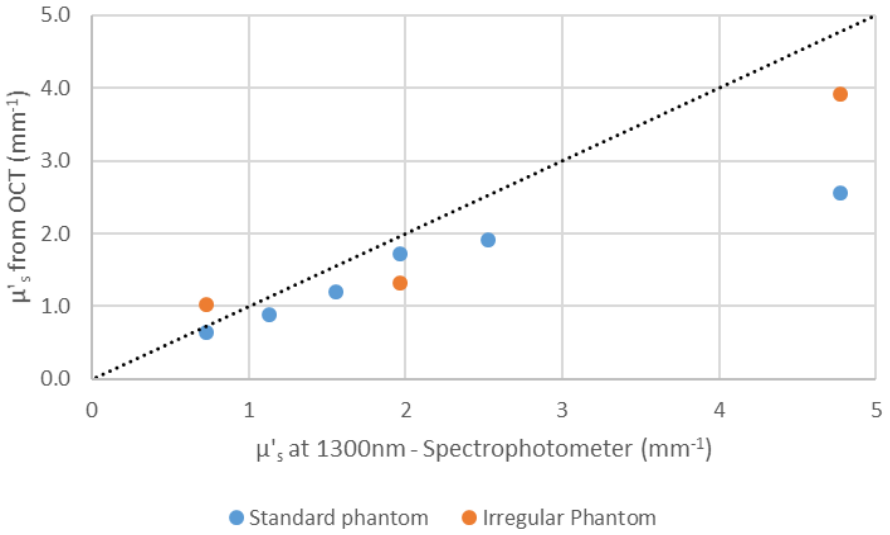

Figure 37. *Comparison of scattering properties as calculated from spectrophotometer, and OCT at 1300nm.*

Figure 37 shows that there is reasonable correlation between the μ'_s values obtained from both OCT and spectrophotometer for the lower scattering phantoms with μ'_s of less than $3mm^{-1}$. The highest scattering phantom shows a much greater deviation from the expected values as determined by

spectrophotometer, and this may be because the single scattering assumption does not hold in higher scattering samples. Most biological tissues have a μ'_s value of below 2mm^{-1}, therefore the accuracy of the OCT method at values below this, is of greatest importance moving forward.

7.3.2. Uneven surface phantoms

To assess the ability of the analysis method to calculate the value of μ'_s in samples that have irregular upper surfaces rather than the perfectly flat surfaces of the phantoms, an 'irregular phantom' made from small pieces of phantoms 2B, 2E and 2G (Table 6) was created (Figure 38). The phantom was imaged and analysed as previously described, with the beam focused below the surface of the smallest part of the phantom. Again, the 10mm^3 2A phantom was used as the calibration phantom.

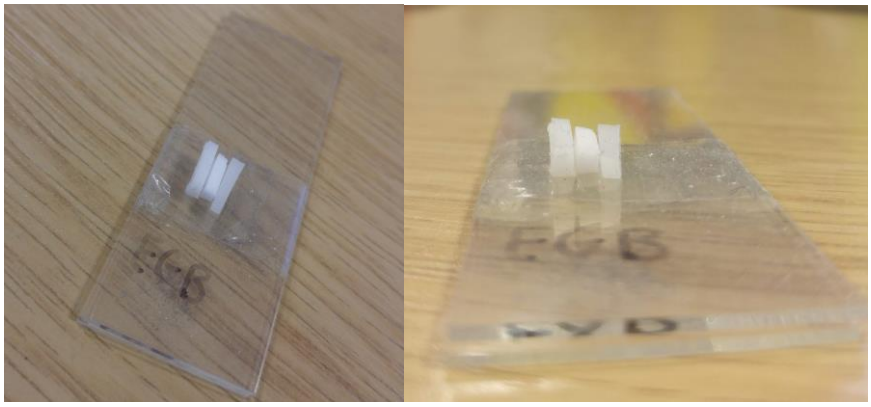

Figure 38. *Irregular phantom made from small pieces of phantoms (Left to right) 2E, 2G and 2B*

The fit was performed over a depth of 76.88µm, starting at approximately 24.8µm from the aligned upper surface, and μ_t values were converted to μ'_s for comparison with spectrophotometer results at 1300nm. Figure 37 shows that the optical scattering of the irregular phantom can be measured with reasonable accuracy from the aligned A scans, therefore demonstrating the reliability of the analysis method.

7.3.3. Porcine muscle and fat

To confirm the suitability of this method of analysis of biological samples, a piece of porcine muscle and fat tissue were imaged, again, using phantom 2A as a calibration phantom. The value of g and refractive index of the tissue were estimated as 0.9 and 1.4 at 1300nm respectively[31], with the A scan

depth corrected for the latter. The A scans were aligned, so the top of the sample was at the top of the image (Figure 39), and the fit was performed over a depth of 126.48µm, at 49.6µm and 99.2µm from the aligned upper surface for muscle and fat respectively.

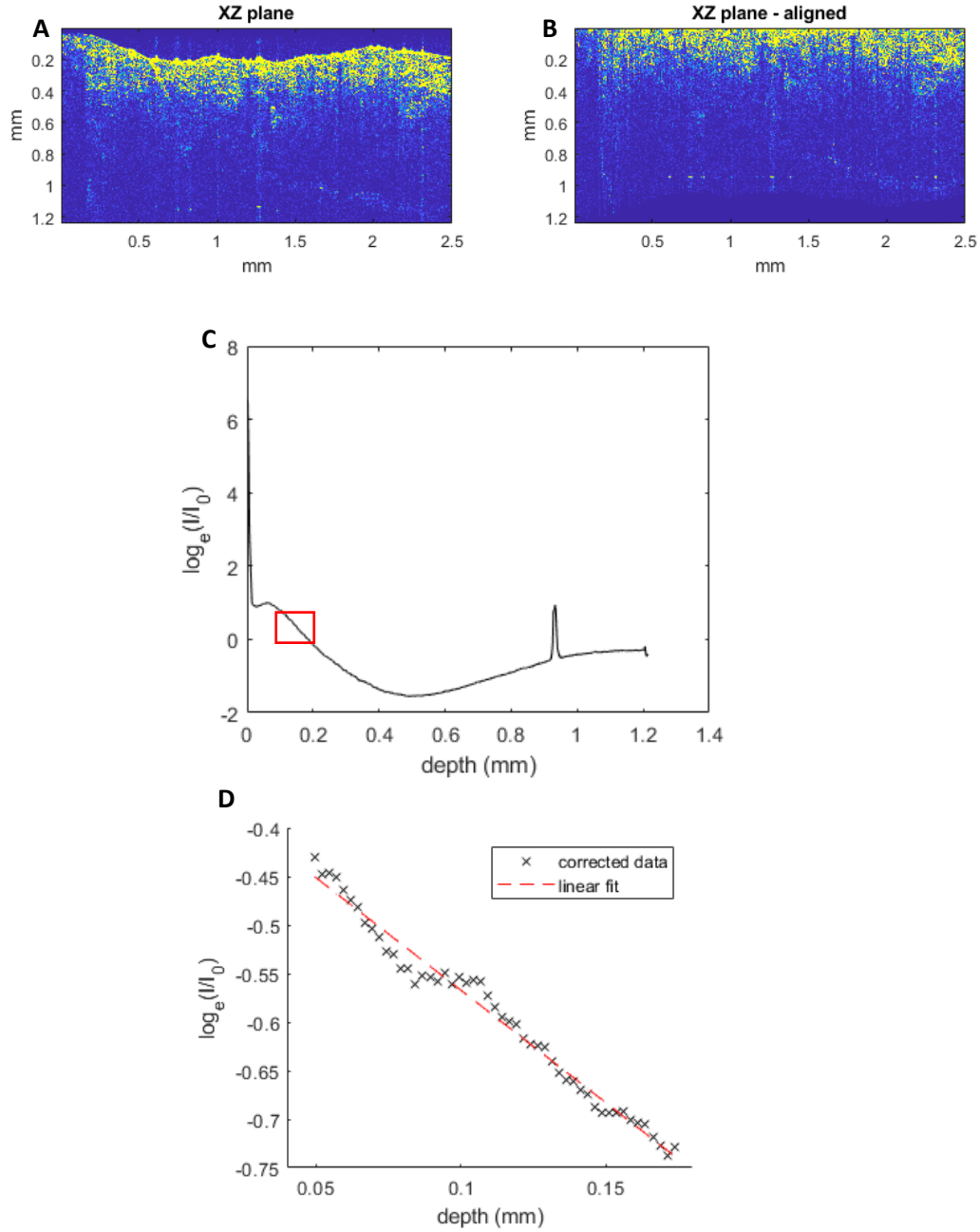

Figure 39. *Porcine muscle A. unaligned data, and B. the same data aligned to the top surface of the image, prior to correction and fitting. The aligned profile is corrected using the calibration phantom (C), and the data in the single scattering region within the highlighted area, is fit with a linear model (D).*

Three areas of each sample were imaged, and the values calculated were averaged to give the final values of μ_t and μ'_s (Table 9). The experimentally corrected data, as seen by the black crosses in Figure 39 shows a deviation from the linear fit due to the surface roughness of the sample which is known to invalidate the exponential relationship from which μ_t is derived. [206]. Furthermore, tissue also has resolvable inhomogeneity which causes a variable signal decay over the depth of the sample. After following similar protocols to previously published studies, comparable signals and noise levels are seen in the measured data[9,10].

Sample	μ_t (mm^{-1})	μ'_s (mm^{-1})
Porcine muscle	2.53	0.34
Porcine fat	6.02	0.80

Table 9. *OCT calculated optical scattering coefficients.*

The calculated values of μ'_s were comparable to the values stated in literature of between 0.07 and 0.54mm^{-1} for muscle, and 0.64 to 1.49mm^{-1} for fat[20]. The μ'_s and μ_t for muscle is approximately half that of fat, which was expected, based on literature values, therefore confirming the data acquisition and analysis method as suitable for subsequent use with uneven biological tissues.

7.4. Conclusions

The optical scattering properties of thin agarose, gel wax and silicone phantoms can be determined via spectrophotometry and IAD, however measurement is dependent on the samples being uniformly thin – a condition unobtainable with biological tissues due to resulting desiccation and fragility. OCT provides a reliable and alternative method of determining the scattering properties of thick tissue volumes *ex vivo* with the reliability demonstrated using phantoms and via comparison with literature values for biological tissues.

8. Quantitative X-ray Scattering Measurement

8.1. Introduction

Dark field x-ray phase contrast imaging using the edge illumination (XPCi-EI) method relies on differences in delta values between sub pixel structures and their surrounding material. This difference causes refraction which varies on a subpixel scale, the direction of which is thus unable to be resolved. The resulting 'scattering' signal has been used as a complementary source of diagnostic information when imaging breast samples[102] and emphysematous murine lungs[107]. The signal is typically retrieved by measuring the increase in the width of the beamlet profile as a sample is placed in the field of view, with a single Gaussian used to approximate each beamlet profile[106] both before and after sample placement. Unfortunately, due to the EI masks' incomplete absorption, and therefore the inability to create truly "dark field" conditions, the existing method of retrieval can be problematic. This chapter describes the development of a novel 'three Gaussian Method' of retrieval, which enables the retrieval of very small scattering signals in highly absorbing samples, overcoming the problems with sample absorption, beam hardening and incomplete mask absorption. Finally, the scattering signal is decoupled from the thickness of the sample, analogous with the scattering coefficient in the optical wavelengths, enabling the comparison of materials and tissues of different thickness.

8.2. Materials and Methods

8.2.1. X-ray phantom design

For the gel wax and silicone samples, the x-ray phantoms were created by permanently mounting a small piece of each phantom for a range of thicknesses (approx. 10mm, 6mm, 4mm and 2mm) onto a glass slide, using epoxy resin (Figure 40). The agarose samples were stored, submerged in water, and mounted in the same configuration, but in a non-permanent manor using double sided tape, however, this was done immediately prior to measurement. The thickness of the phantoms was determined by digital callipers, and the agarose samples were placed back into water immediately after use to preserve their hydration. All phantoms were imaged, however retrieval data for sample 2G is not presented due to an error in acquiring the data.

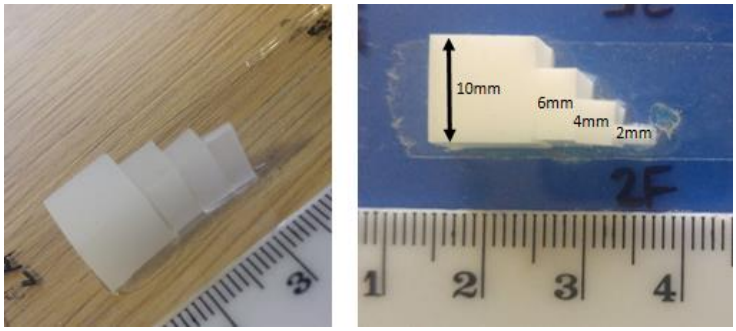

Figure 40. *X-ray samples mounted on a glass slide using epoxy resin.*

8.2.2. Edge Illumination (EI-XPCi) system

Images were acquired using the previously described EI system[102] (Figure 41), with a Mo source operated at 40kV and 30mA, along with a Pixirad (Pixirad Imaging Counters s.r.l., Italy) photon counting detector with pixel size of 62 x 62µm^2. The masks were manufactured by Creatv MicroTech (Potomac, MD, USA). The sample and detector masks had a pitch of 48µm and 59µm, and aperture width of 12 and 17µm, respectively. The source to detector distance was 1.26m, and the sample and detector masks were placed so as the magnified periods of both masks were equal to the pixel size of the detector, at 0.98m and 1.20m from the source respectively. The IC was generated using 15 sample mask positions with subsequent flat field and object images acquired using 33 sample mask positions distributed symmetrically about mask position 17, the point of maximum pixel exposure.

8.2.3. Flat field Image acquisition

The flat field image was either:

1. An image in the absence of a sample (standard flat field) or,

2. An image in the presence of plain bulk material (either silicone, gel wax or agarose) – homogeneous, assumed non-scattering sample (alternative flat field),

With the second approach being used to compensate for the beam hardening effect associated with highly absorbing phantoms. The object image is obtained with the same system parameters as the flat field except for the presence of the scattering phantom. The exposure time for the IC, flat field and object image at each mask position was 250ms to eliminate the possibility of pixel saturation, and a total of 16 frames per mask position were taken. For analysis, all 16 frames per sample mask position were summed

to improve the signal to noise ratio. The alternative flat fielding method was unable to be performed on sample 1D, due to error in sample positioning during data acquisition.

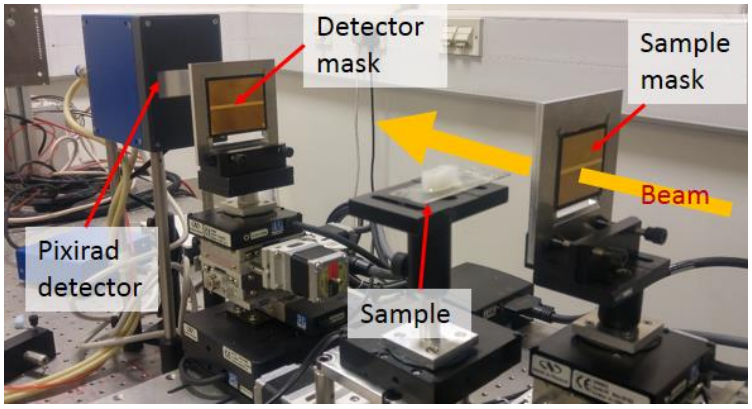

Figure 41. *Edge illumination system with sample in place. The sample can be seen in place on the sample stage, and the direction of imaging is shown by beam.*

8.3. Retrieval

8.3.1. 1 Gaussian retrieval

Signal retrieval was performed on an 81 x 13 pixel area of the image where the phantom was present. The retrieval was performed by fitting a single Gaussian with an offset to the data in a pixel by pixel basis, via a previously published method[106], from here on in known as the '1 Gaussian retrieval'. Flat fielding was initially performed using both the standard, and alternative flat field methods.

8.3.1.1. Retrieval Method

Retrieval was performed locally via use of the illumination curve (IC). A Gaussian with an offset (represented by d in the following equations) was fitted to the 15 illumination points for each pixel, creating a pixel by pixel IC:

$$y_{IC}(x) = a\frac{e^{\left(\frac{-(x-b)^2}{2c^2}\right)}}{\sqrt{2\pi(c^2)}} + d \qquad \textit{Equation 37}$$

Where $y_{IC}(x)$ is the recorded IC intensity in each pixel, and x is the position of the sample mask. From this fit, a set of unique coefficients (a, b, c and d) were obtained and stored for each pixel. The offset is necessary due to the imperfect absorption by the mask septa, meaning that when both masks are

completely misaligned with respect to each other, the intensity at the detector is not 0.

Using these coefficients, a Gaussian with an offset was then fit to the 33 points obtained for each pixel in both the flat field and sample image:

$$y_{object}(x) = t\left(a\,\frac{e^{\left(\frac{-(x-b-r)^2}{2c^2+s}\right)}}{\sqrt{2\pi(c^2+s)}}\right) + d \quad + t_0 \qquad \textit{Equation 38}$$

Where $y_{object}(x)$ is the recorded intensity in each pixel of either the flat field or sample image, and x is the position of the sample mask. The coefficients t, r and s are obtained for each pixel, for both the flat field (t_{flat}, r_{flat}, s_{flat}) and sample image (t_{object}, r_{object}, s_{object}), and correspond to the decrease in peak intensity, shift in the position of the maximum along the x axis and broadening of the Gaussian, respectively. The t_0 parameter is an additional transmission parameter, added to try to counteract the effects of absorption and beam hardening. For retrieval of the scattering sample, accurate knowledge of the intensity distribution over the entire range of sample mask positions for the object and flat field data is required for modelling and fitting of the Gaussian, therefore the curve is heavily over sampled, using 33 mask positions. This precision is less important with the IC, therefore a compromise between scan speed and mask positions was sought, and fewer mask positions were used to enable a faster acquisition, whilst maintaining adequate sampling intervals.

To obtain the transmission (t_{image}), refraction (r_{imaage}) and scattering (s_{image}) images, the following equations can be used on a pixel-by-pixel basis:

$$t_{image} = \frac{t_{object}}{t_{flat}}, \qquad \textit{Equation 39}$$

$$r_{image} = r_{object} - r_{flat} \text{ , and,} \qquad \textit{Equation 40}$$

$$s_{image} = s_{object} - s_{flat}, \qquad \textit{Equation 41}$$

with t_{image} a unit-less quantity (decrease of the height of the Gaussian peak compared to the height of the peak from the flat field image), r_{image} carrying units of distance (distance of lateral translation of the peak of the Gaussian when compared with that of the flat field), and s_{image} carrying units of distance squared (the difference in variance of the flat field and sample image Gaussians). The s_{image} value is therefore an indirect measure of

scattering and is a measure of how much the beamlet has been broadened by the scattering structures within the sample and is not only defined by the sample being imaged, but also the system used to obtain the data. The current understanding of x-ray scattering is based on the assumption that in the absence of a sample, the beam is well modelled by a Gaussian. A sample that contributes to scattering can also be modelled as a Gaussian, and therefore the scattering signal measured by such a sample is the convolution of these two Gaussians, and this has been well validated[4,102,106]. How the s_{image} value relates to the underlying structure of the scattering sample is currently subject to ongoing investigation but appears to be related to both the magnitude and directionality of the scatterers (PRT Munro 2019, personal communication, 10th October). The choice to use mm^2 (variance) as opposed to mm (standard deviation) to define the scattering by a sample is of personal choice, however it was decided to follow the standard as set by previous publications on EI-XPCi scattering retrieval[102] and therefore mm^2 was adopted. Finally, the background values of t_{image}, r_{image} and s_{image}, calculated from an area without sample present, are all subtracted (r_{image} and s_{image}) or divided (t_{image}) from the sample, so that all areas without sample are made equal to zero (r_{image} and s_{image}) or one (t_{image}).

8.3.1.2. Results

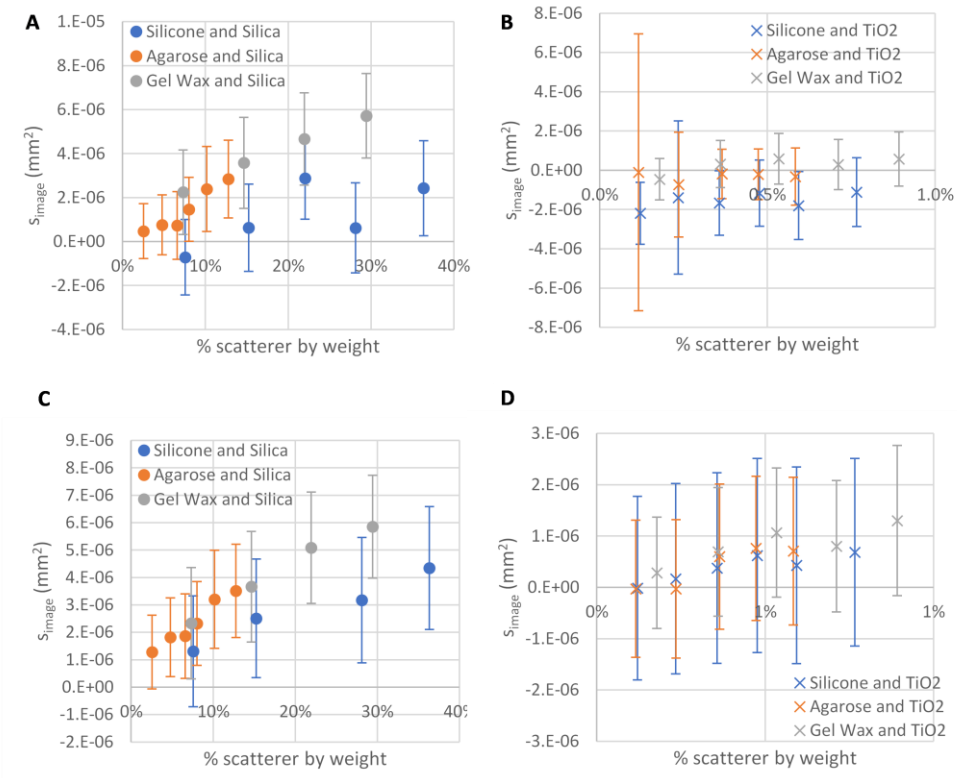

Figure 42. *Variation of s_{image} values with the concentration of scatterer for all phantoms. Graphs A and B show retrieval using the standard flat fielding method for silica and TiO_2 containing phantoms respectively, and graphs C and D show retrieval using the alternative flat fielding method for silica microsphere and TiO_2 powder containing phantoms respectively. Error bars show +/- 1 standard deviation.*

Figure 42A and B demonstrate the inability to detect a scattering signal when the '1 Gaussian retrieval' is used with the standard flat fielding method, due to the high noise level. The high noise level is caused by poor modelling of the tails and slopes of the beamlets, when using a single Gaussian (Figure 43) causing poor consistency in fitting over the area of the phantom, and therefore wide variation of s_{image} values. Accurate modelling of the slopes and tail of the beamlet are essential in scattering retrieval, as the microstructure of the sample causes broadening of the beam, which is observed in these areas of the beam profile. The values considered for x-ray scattering are very small (in the region of 1 x 10^{-6}mm^2), therefore even small errors or uncertainties in the modelling have the ability to negatively affect the retrieved signal or render it impossible to retrieve.

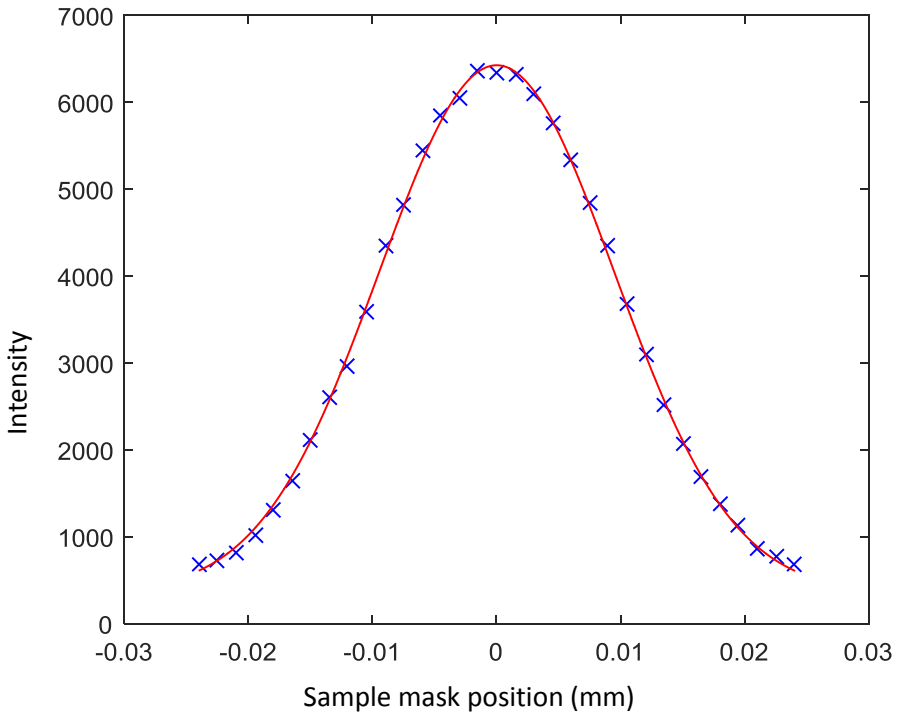

Figure 43. *An example Gaussian fit from one pixel. The experimentally acquired data points are shown as blue crosses, and the 1 Gaussian fit shown in red.*

In over half of all the phantoms, and all but one of the TiO_2 containing phantoms, the mean s_{image} value is smaller than the measured error value. Furthermore, almost all the TiO_2 based phantoms cause an unexpected narrowing of the beamlet profile, resulting in a negative scattering signal. The highly absorbing silicone and silica microsphere phantoms also have almost undetectable scattering, despite high scatterer concentrations. If the alternative flat fielding method is employed, then scattering above the noise level is detectable in the silica microsphere containing phantoms (Figure 42C), however, the signal is still completely undetectable in TiO_2 powder containing phantoms, which have much lower scatterer concentrations of below 1% (Figure 42D).

Although the alternative flat fielding method enables the detection of scattering in some of the phantoms, the detection of weak scattering signals is still elusive. Strong X-ray absorption prevents the accurate retrieval of scattering signal and causes the negative scattering signals. It is known that the phantom masks are not 100% absorbing, and this also effects the ability to fit a single Gaussian accurately to the data, as both tails are strongly

perturbed by transmission through the mask. If scattering from relatively low scattering biological tissues is to be made possible, then a retrieval method which overcomes beam hardening and partial mask absorption is required.

8.3.2. 'Three Gaussian retrieval'

Results reported in this subsection regarding the development of the 'three Gaussian retrieval' method have been published in: Charlotte J. Maughan Jones, Fabio A. Vittoria, Alessandro Olivo, Marco Endrizzi, and Peter R. T. Munro, "Retrieval of weak x-ray scattering using edge illumination," Opt. Lett.43, 3874-3877 (2018). https://doi.org/10.1364/OL.43.003874

A new method of retrieval for quantitative determination of very weak x-ray scattering signal was developed to overcome the problems caused by beam hardening, which were encountered using previously described methods[102,106] (Figure 44). Previous retrieval methods consider a single independent Gaussian per pixel to represent the illumination curve (IC) before the introduction of a sample, which is reduced in amplitude, shifted along the direction of phase gradient sensitivity and broadened by attenuation, refraction and scattering effects of the sample, respectively[102] . It is well known that the mask columns are, however, partially transmitting[106] , therefore the ICs in adjacent pixels are not independent from each other because the beamlet incident on each pixel, contributes not only to the signal in the pixel itself, but also to the signal recorded by its neighbours. The following retrieval method ('three Gaussian retrieval') also accounts for such interactions between pixel signals.

Signal retrieval was performed on the same 81 x 13 pixel area of each image where the phantom was present. The same pixels were used for the IC, object and flat field image for each scatterer concentration. Three overlapping Gaussians separated by the sample mask period of 48μm were fitted to the IC data from three horizontally adjacent and non-independent pixels to gain the coefficients a_i, b_i and c_i, unique to each set of three pixels:

$$y_{IC}(x) = \sum_{i=-1}^{1} a_i \frac{e^{\left(\frac{-(x-b_i+i\Delta)^2}{2{c_i}^2}\right)}}{\sqrt{2\pi({c_i}^2)}}, \qquad \textit{Equation 42}$$

Where y_{IC} is the recorded number of counts at each sample mask position, Δ=0.048mm (sample mask period), and x is the sample mask position in mm.

The fitting process continues, moving one pixel in the horizontal direction until each group of three horizontally adjacent pixels are assigned nine coefficients in total. Only the three coefficients corresponding to the central pixel are retained to contribute to the retrieved image.

Three overlapping Gaussians separated by the sample mask period are subsequently fitted to the experimental data obtained when a sample is in place in the system. Utilizing the parameters gained from the IC fitting, the values of t_i, r_i and s_i are obtained:

$$\boldsymbol{y_{object}(x) = \sum_{i=-1}^{1} t_i \left(a_i \frac{e^{\left(\frac{-(x-b_i-r_i+i\Delta)^2}{2(c_i^2+s_i)} \right)}}{\sqrt{2\pi(c_i^2+s_i)}} \right)}, \qquad \textit{Equation 43}$$

Where y_{object} is the recorded number of counts at each sample mask position (x). The parameters t_i, r_i and s_i (maxima, position of the maxima and standard deviation of the IC respectively) are kept for the central pixel (i=0) and discarded for the pixels on the left and right (i=1 and i=-1), leaving one set of parameters (t_{object}, r_{object}, s_{object}) per pixel. This process (Equation 43) is repeated for the flat field image to obtain a further set of parameters (t_{flat}, r_{flat}, s_{flat}) per pixel.

To obtain the final attenuation (t_{image}), refraction (r_{image}) and scattering (s_{image}) images, equations 39, 40 and 41 can be used on a pixel by pixel basis. This method can be used to retrieve the attenuation, refraction and scattering signal from a sample, however only the scattering signal shall be presented and discussed with respect to the phantoms described.

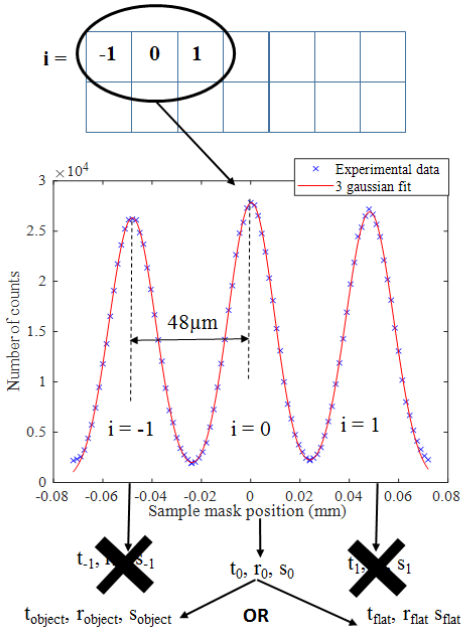

Figure 44. *Schematic of the 'three Gaussian retrieval' on an image (7 x 2 pixels), including an example of the fit obtained using experimental data, to gain either the object or flat field parameters (t, r and s).*

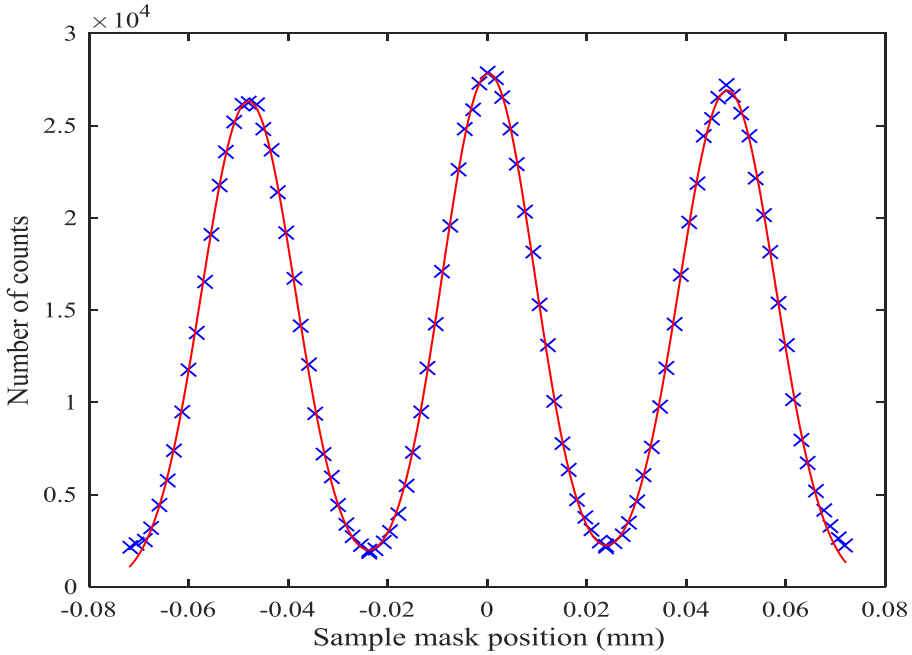

Figure 45 *Example 'three Gaussian retrieval' for signals from three adjacent pixels.*

Figure 45 shows an example of the Three Gaussian fit for data from three horizontally adjacent pixels. The experimentally obtained data is shown using blue crosses and the fit from Equation 43 is shown with a red line.

Although the modelling of the tails of the data from the two outermost pixels is visibly imperfect and does not account for the offset and adjacent pixel interaction caused by imperfect sample mask absorption, the modelling of the data from the central pixel appears subjectively to be excellent.

8.3.3. Sample mask position uncertainty

Ideally, the fitting of the Gaussians should be completely stable, so that small errors in the measurement of the sample mask position do not affect the retrieved absorption, scattering and refraction signals. If complete stability is not possible, then the uncertainty in the fit should be as small as possible to ensure confidence in the values generated. There is known uncertainty in the mask positions, with the manufacturer of the precision stages on which they are mounted quoting an error of +/- 0.3μm from the recorded position[207]. The experimental data is fit using the least squares method, which does not account for errors in the sample mask position (x-axis), and therefore the performance of the fitting method under conditions of known error must be evaluated.

To assess the stability of the fitting method, 33 data points per Gaussian were generated using the fit from a single pixel in the background region of sample 4E, where all 33 points formed a perfect Gaussian. A randomly allocated 'error' within a specified maximum error, was added or subtracted from the sample mask position of each of the 33 points, with the number of counts remaining unchanged. Using the new sample mask positions with error added to them, either one Gaussian (equation 38), or three Gaussians (equation 43) were fit to the data, and the s_{object}, t_{object} and r_{object} values recorded. This was repeated 10,000 times, with different random errors added to the original data points before each round of fitting. The difference between the maximum and minimum s_{object}, t_{object} or r_{object} values generated by the 10,000 fittings was considered the uncertainty of each retrieved value. Uncertainty values were generated for multiple maximum errors, and the closer the value to 0, the greater the stability of the fitting method when there is uncertainty in the sample mask position.

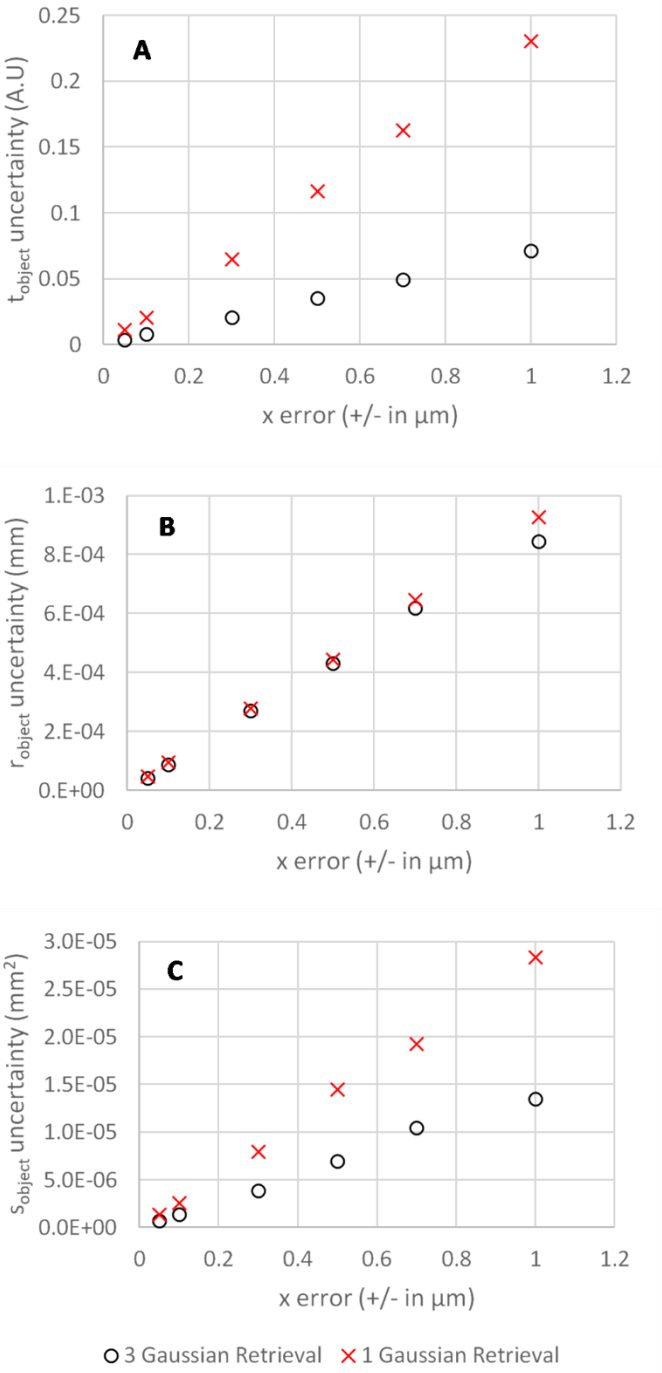

Figure 46. *Uncertainty in the retrieved value of A.* t_{object}*, B.* r_{object} *and C.* s_{object} *for different maximum errors in mask position (x error) for data from a background pixel from sample 4E. For the three Gaussian retrieval, the absolute values of* t_{object}*,* r_{object} *and* s_{object} *for this pixel were 1.00 A.U., -1.80x10^{-4}mm and -7.49=10^{-7}mm^2 respectively, and 1.03 A.U., -1.79x10^{-4}mm, 1.87x10^{-6}mm^2 respectively for the 1 gaussian retrieval.*

Figure 46 shows that neither of the retrieval methods offers complete stability when an error in the mask position is introduced, however the three Gaussian

retrieval method demonstrates a much lower uncertainty for all x-axis error values in t_{object} and s_{object} values, and a small decrease in uncertainty for r_{object} values. The three Gaussian retrieval method can therefore be considered more robust with regards to uncertainty in the sample mask position compared to retrievals using only 1 Gaussian, therefore errors in mask placement have a lesser effect on the final retrieved values.

8.4. Results

To enable direct comparison between samples, the values of s_{image} were corrected by the background so that all areas of the image without a sample present have a value of 0. The background value of s_{image} was calculated from the mean of a 76 x 13 pixel retrieved area where no sample was present, and this value was subtracted from every pixel within the image. The values of s_{image} presented were calculated from the mean of all the pixels in the retrieved area, and the standard deviation calculated from the same pixels. From here on, the s_{image} values are retrieved using the 'three Gaussian method' of retrieval.

8.4.1. % Scatterer by weight vs. s_{image}

All s_{image} values were calculated for the 10mm thick sample, due to the greater uniformity in thickness between samples, therefore allowing more accurate cross phantom comparison compared to the other thicknesses. Figure 47 shows that if the standard flat fielding method is used, the s_{image} values are negative for many of the phantoms, however if the values are rigidly translated so that phantoms with 0% scatterer concentration (i.e. plain silicone, gel wax or agarose) are assigned values of s_{image}=0mm^2 ('translated standard flat field'), then, not only do all the values become positive, but they follow the trend seen when using the alternative flat fielding method. This is true for all the bulk material-scatterer combinations. Prior to result translation, negative values arise because of absorption properties of the sample, which reduces the width of the IC, whereas positive values arise due to scattering from sub pixel features within the sample, broadening the width of the IC. Negative s_{image} values are therefore more commonly seen in very low scattering, but highly absorbing samples, where the broadening by scattering is not enough to counteract the narrowing by absorption.

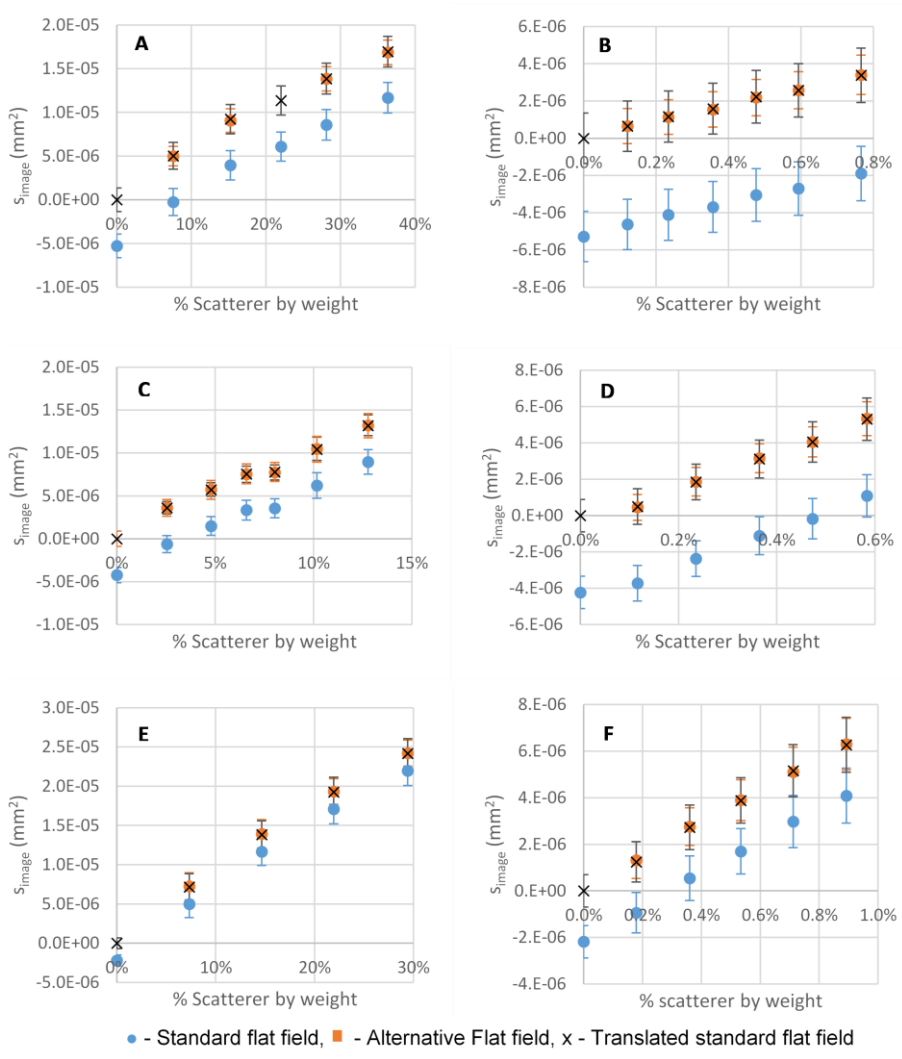

Figure 47. *% scatterer by weight vs. s_{image} values for each of the flat fielding methods. A. Silicone and silica microspheres, B. Silicone and TiO_2 powder, C. Agarose and silica microspheres, D. Agarose and TiO_2 powder, E. Gel wax and silica microspheres, F. Gel wax and TiO_2 powder. Error bars show +/- 1 standard deviation from the mean.*

Due to the interest in the fit to the central pixel's data only, goodness of fit statistics are not appropriate in this case to assess the accuracy of the method or to provide a comparison with the one Gaussian retrieval, as these would account for the fit over all three pixels, and not just the central one. Alternative methods of assessing the performance of the fitting model must be used. As this is predominantly an image retrieval method for non-resolvable features, the resolution is not an appropriate measure, however assessing the standard deviation of the signals provides a way of determining the performance of the fitting models. A lower standard deviation

(or noise) confers with a reliable and consistent fit over all pixels of interest within the sample, where as a larger standard deviation shows that the model is not able to accurately fit to the data. This analysis is only appropriate for homogeneously scattering samples such as the phantoms discussed here, where the s_{image} signal retrieved from each pixel should be the same, or very similar over the region of interest. Furthermore, retrieval using the three Gaussian retrieval method retrieves the expected linear relationship between s_{image} values and % scatterer by weight for phantoms of the same thickness, therefore demonstrating the accuracy of the fit compared to the one Gaussian method, where the relationship for many of the phantom combinations is clearly not linear. Assessment of the standard deviation of the three Gaussian retrieval forms the basis of the analysis within the publication describing the three Gaussian retrieval[4].

When results in Figure 47 are compared to the results obtained from the one Gaussian retrieval in Figure 42, it is clear that the standard deviation of the retrieved signal is much smaller for the three Gaussian retrieval method. This demonstrates the accuracy of the model as it is able to assign s_{image} values of greater similarity over the entire area of the phantom compared to the one Gaussian method. The signal to noise ratio (SNR) here has been defined as the ratio of the mean signal to the standard deviation of that signal over the area of interest and is displayed in Figure 48. It is clear that the three Gaussian retrieval method is associated with a higher signal to noise ratio for all samples, meaning it outperforms the one Gaussian method for all phantom compositions.

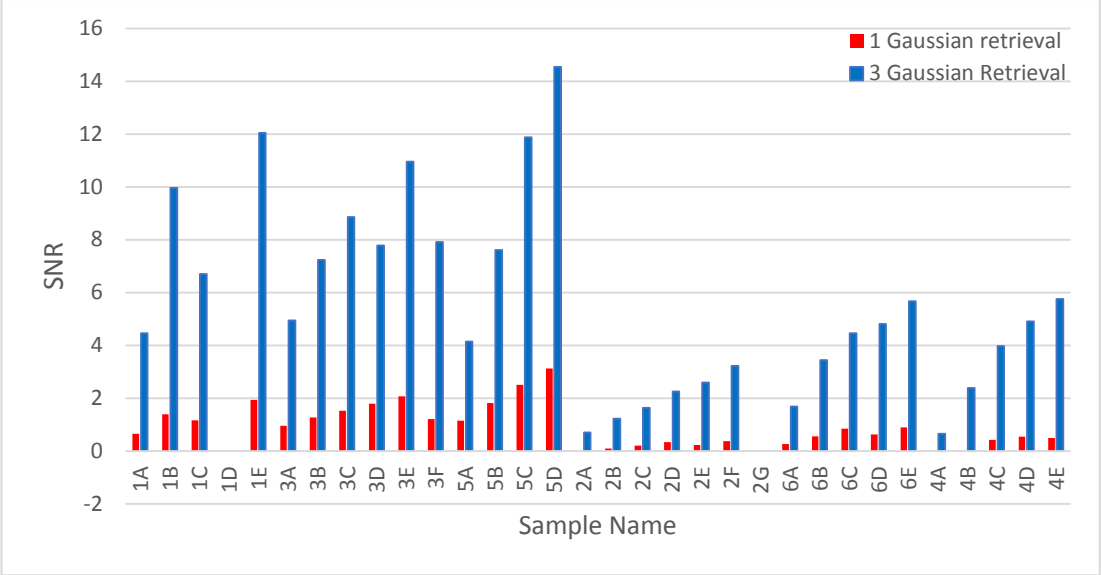

Figure 48. *The SNR for each phantom, for both the one and three Gaussian retrievals. The values have been calculated from the alternative flat fielding method in both cases. The SNR is defined in this case as the ratio between the mean* s_{image} *values to the standard deviation of the* s_{image} *values, both obtained from the same area of the image.*

8.4.2. Reduction in number of IC points sampled

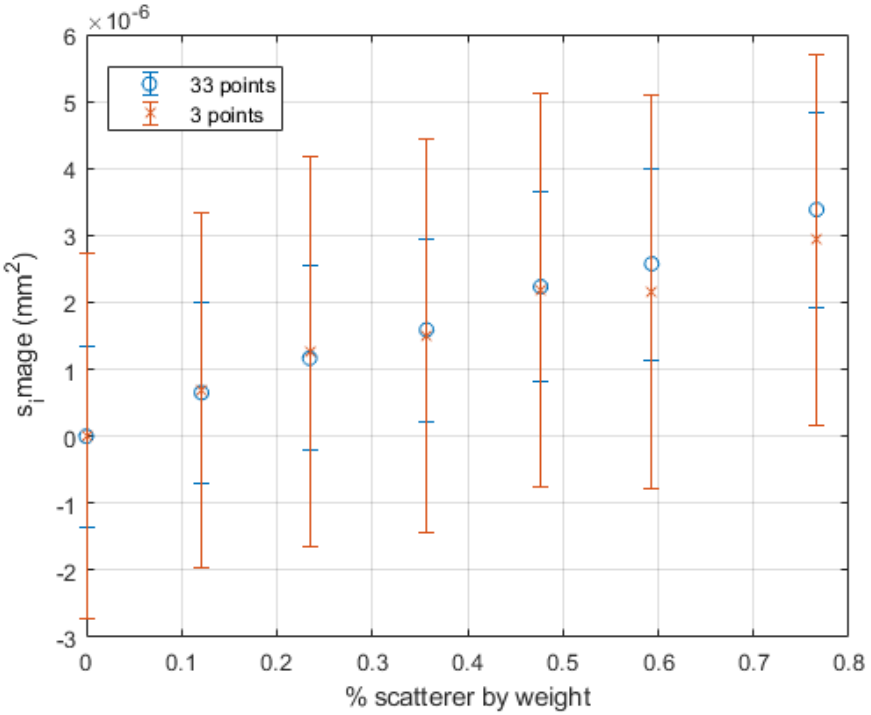

Figure 49. *The effect of reducing the number of sample mask positions from 33 to 3 per pixel on the retrieved scattering signal for all silicone* TiO_2 *phantoms.*

If the number of positions of the sample mask is reduced from 33 to 3 for both the object and flat field images, to make the imaging acquisition protocol similar to those already described[106], then although the noise increases, the mean values of s_{image} remain relatively unchanged, and within the standard deviation of the original value. The 3 points used in these calculations corresponded to maximum pixel illumination (centre of the IC) and to approximately 50% pixel illumination of either side of the IC (FWHM of IC).

8.4.3. Thickness of sample vs s_{image}

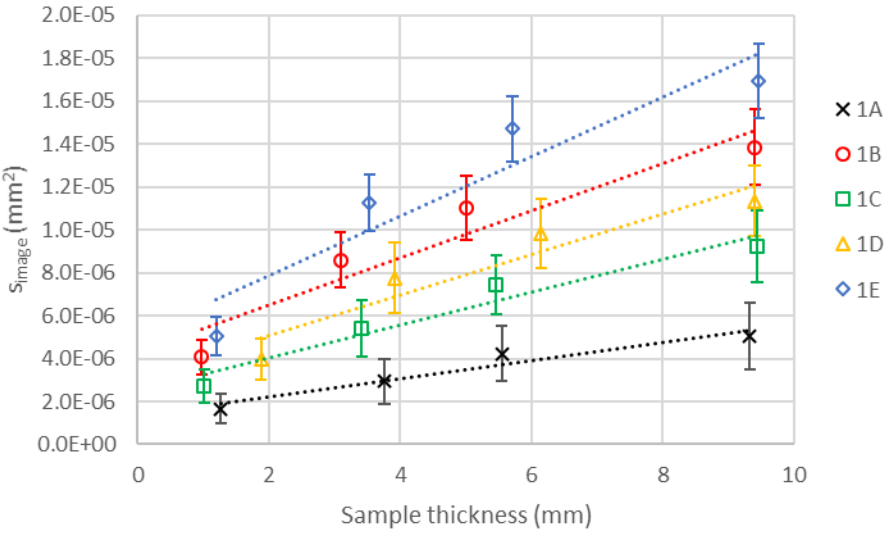

***Figure 50**. The effect of sample thickness on s_{image} for all concentrations of silicone and silica microsphere phantoms. Displayed s_{image} values are of the translated standard flat field to ensure positive values.*

Regardless of the concentration of the scatterer within the phantom, as the thickness of the sample increases, so does the s_{image} value. Although silicone and silica phantoms have been chosen as an example, if the translated standard flat field method is applied, then the same pattern is seen for all phantoms.

8.4.3.1. Thickness independent scattering parameter

The scattering value is highly dependent not only on the phantom composition, and scatterer concentration, but also the sample thickness. To enable comparison of scattering between samples of different thickness, the scattering sample must be decoupled from the thickness, in such a way as the scattering coefficient is within the optical wavelengths. To do this, the

s_{image} value for each of the phantom concentrations was plotted against the thickness of the sample, with a line of best fit calculated for each sample concentration as in Figure 50, with the gradient of this fit noted. Although the samples were designed to be approximately 2mm, 4mm, 6mm and 10mm, the actual thickness in the direction of beam transmission was determined by digital callipers. The gradient was then compared to the s_{image} value retrieved from the 10mm thick sample of the phantom using the standard translated flat fielding method. This thickness was chosen rather than others as it was more uniform between samples, therefore the values were more directly comparable to each other. The gradients were calculated using both the standard and standard translated flat fielding method.

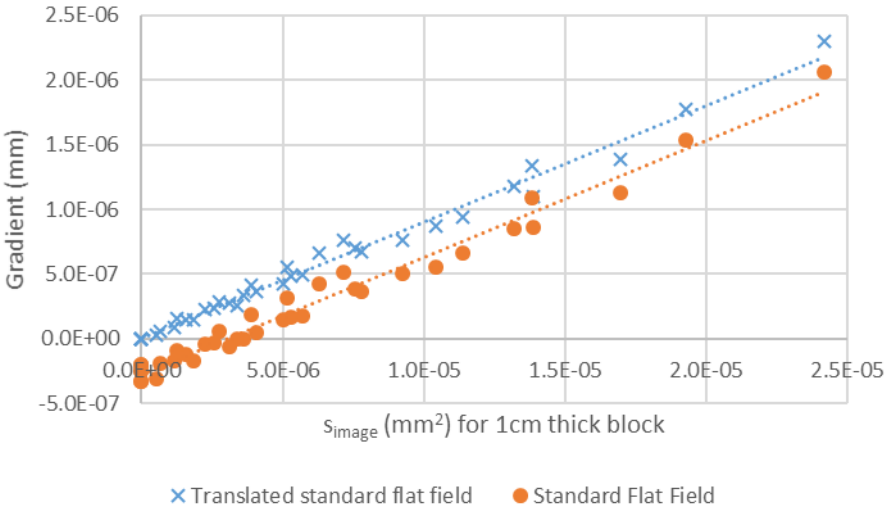

Figure 51. *The correlation between the gradient of the thickness data and the s_{image} value of the 10mm thick portion of each phantom. The s_{image} values were obtained via the translated flat fielding method. Each point represents a different phantom.*

There is a strong linear correlation between the measured s_{image} value for a 10mm block, and the extracted gradient, regardless of whether the standard flat field data is translated or not (Figure 51), demonstrating the gradient's usefulness in predicting the x-ray scattering properties. All samples, regardless of their composition or scatterer concentration follow this trend, and the thickness of the sample is no longer a factor in the value.

8.5 Analyser Based Imaging (ABI)

8.5.1. Materials and Methods

The previously described x-ray phantoms were subsequently imaged in the biomedical beam line (ID17) at the ESRF synchrotron facility, with up to 7 phantoms mounted on the sample stage in a staggered configuration, at one time. The staggering allowed each phantom to be imaged individually, with this method of sample mounting adopted as the crystals must be realigned after each system intervention, so mounting multiple samples at one time increases system stability. The sample to detector distance was approximately 2m, and the sample to monochromator and analyser crystal distances, 85cm and 55cm respectively. The detector pixel size had an area of 47μm^2.

The beam had a photon energy of 51keV, and the silicon crystals were used in the 111 configuration. The flat field image was taken without a sample in place, and was taken immediately before, and after each group of samples were imaged, with a mean of both images used during retrieval. The exposure time was set to 300ms for all silicone samples (1A-1E and 2A-2G) as well as the gel wax and silica sphere phantoms (5A-5D) along with their corresponding rocking curves, however due to the intensity of the beam decreasing during the acquisition time, the exposure time was increased to 600ms for all other phantoms (3A-3F, 4A-4E and 6A-6E). A total of 60 points on the rocking curve were taken for sample and flat field images, with steps of 0.094μrad between each point. The full width half maximum of the RC was approximately 6μrad.

8.5.2. Results

The scattering signal was retrieved using a previously published method[84], with retrieval performed on a 51 x 20 pixel area of the 10mm thick portion of the phantom. Due to instability of the rocking curve over the area of the detector, retrieval was only able to be performed on this small area. To enable comparison between ABI and EI scattering results, the signal was corrected for the background by subtracting the scattering signal obtained from a 50 x 40-pixel area without sample in it. The previously described ‘translated standard flat field’ was used.

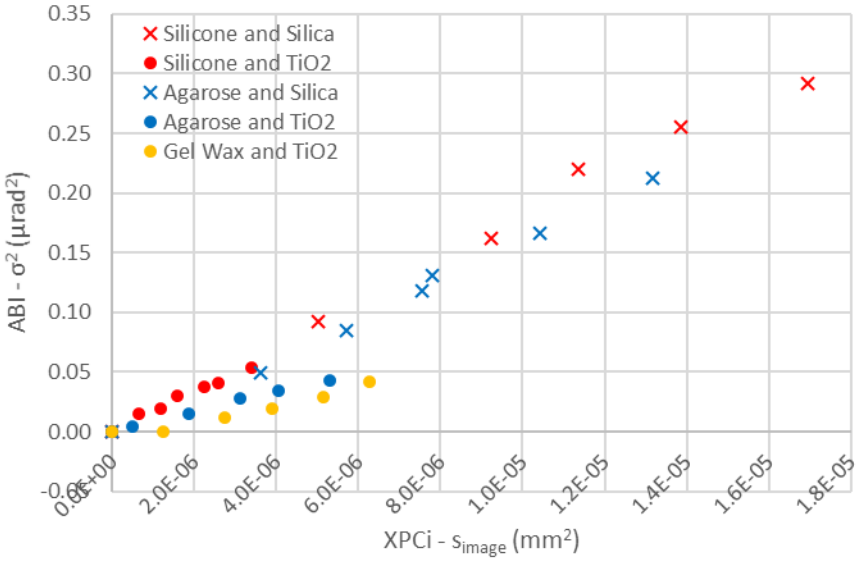

Figure 52. *X-ray scattering signals as retrieved from both ABI and EI x-ray phase contrast imaging methods. The values displayed were retrieved from the 10mm thick sample of each phantom except phantoms 5A-5D, and the standard flat field method was used with results translated to zero based on the non-scattering samples, as previously described.*

If each phantom type is considered individually, then an almost perfect linear correlation between the ABI and EI-XPCi scattering results exist for all silicone phantoms as well as those made of agarose and silica microspheres. Overall, there is a positive correlation between the scattering signal retrieved from the ABI and EI-XPCi methods (Figure 52), when data from all phantoms except those made of silica microspheres and gel wax (5A-5D) are considered together. The decision to exclude these phantoms was made due to their previously determined optical instability, suggesting that the x-ray scattering properties may also not be temporally stable. As the EI data was collected approximately two and a half months prior to the ABI data, it was reasonable to assume that the x-ray scattering could have significantly changed within that time frame, and therefore the results would not be comparable.

8.6. Discussion

The detection of weak scattering signals in highly absorbing materials is made possible via the three Gaussian retrieval methods presented. When embedded within silicone, a concentration of TiO_2 powder as low as 0.1% (% scatterer by weight) creates a small, but retrievable signal. This is akin to the

relatively low x-ray scattering that would be expected from biological tissues, where the difference in delta is small between bulk material (for example, extra cellular matrix) and the scatterers that reside within it (for example, cells or cellular organelles). Previously reported scattering values for neoplastic breast tissues are approximately between 100 to 900μrad^{2,} , with calcifications demonstrating values above this[102]. The surrounding normal breast tissue demonstrating values of below 100μrad^2 [102]. The samples considered in this study all demonstrate scattering below 100μrad^2, therefore can be considered similar to normal biological tissues.

To increase the accuracy of signal retrieval from the central pixel, then data from an additional number of adjacent pixels, up to the total width of the detector, could be considered rather than just three. Whilst this may marginally increase the accuracy of the method in modelling the experimental data, it is unlikely to significantly change the outcome, or retrieved s_{image} values, as the signal contribution to the central pixel from distant pixels is negligible. The reason for the interaction between adjacent pixels, as modelled by the three Gaussian method, is due to the imperfect absorption of the mask rather than pixel crosstalk, therefore this effect is only apparent in pixels directly underlying the absorbing septa of the masks.

Although not explicitly considered here, the silicone phantoms are the most highly absorbing, with those embedded with TiO_2, absorbing between 83.3% and 83.7% of the primary x-ray beam, therefore significant beam hardening would be expected, and the negative s_{image} values are expected. Although gel wax is the lowest absorbing of all the bulk materials, with plain gel wax absorbing only 34.8% of the primary beam, significant IC profile narrowing is still observed, and therefore s_{image} values are also negative. This demonstrates the importance of the three Gaussian method in not only correcting for beam hardening and absorption effects in highly absorbing, materials, but also in lower, but still significantly absorbing organic materials, which can be considered closer in chemical composition to biological soft tissues.

Beam hardening is considered a hindrance to accurate quantitative scattering retrieval due to the beam, now with a higher average energy, being able to penetrate the absorbing columns of the detector mask, therefore artificially increasing the width of the observed IC when a sample is in place

from what it would have been if the sample did not cause hardening. The effect also acts to increase the noise of the image to the point of rendering the scattering signal unobservable. The three Gaussian retrieval method is able to overcome the effects of beam hardening on the scattering signal, producing retrievable scattering signals, typically above the observed noise of the imaging system, even in high absorbing and low scattering samples. The three Gaussian retrieval is superior to a single Gaussian because the partial transmission of the masks leads to a poor fit when a single Gaussian is used. The mismatch between the fit and experimental data, especially at the tails of the Gaussian, is significant enough to prevent the fit from sensing subtle changes in the IC width.

For translation into the biomedical field, close attention to the dose received by the patient is required. In previous scattering retrieval methods using edge illumination, 3 sample mask positions have been used[102,106,109,208] . It has been demonstrated that this new retrieval method can retrieve the scattering signal from 3 such sample mask positions per pixel, without losing significant accuracy. The limitation of reducing the number of sample mask positions per pixel appears to be the noise level, which increases, however the mean remains stable, which is important when quantitative retrieval is required.

Whilst using phantoms, a non-scattering sample (plain silicone, gel wax or agarose) can be manufactured alongside the scattering ones. This enables the translation to 0 if standard flat fielding is performed (translated standard flat field) and facilitates the retrieval if alternative flat fielding is performed. Tissue is a heterogeneous material, and there are no biological tissues which could be considered as a ‘non-scattering sample’. To translate this method to biological tissues, a non-scattering, and non-biological ‘test material’ of approximately similar elemental composition and attenuation to the tissue of interest could be used, for example tissue equivalent plastics, or PMMA[209] – both of which have been used as tissue mimicking x-ray phantom materials[210]. Alternatively, if absolute values of scattering are not required, and relative scattering between different tissue types in a field of view is sufficient, then ‘local scattering contrast’ could be obtained, by comparing the signal from regions of a sample with similar thicknesses. Such approaches may lead to reduced sensitivity to scattering, however, it is anticipated that the three Gaussian retrieval will remain superior to the single Gaussian.

The thickness independent scattering parameter, or gradient, enables the uncoupling of the sample thickness from the s_{image} values. For example, the 1.73mm thick 3E sample, composed of agarose and silica microspheres, and 9.85mm thick 2F sample composed of silicone and TiO_2 powder, both have almost indistinguishable s_{image} values at $3.83 \times 10^{-6} mm^2$ and $3.38 \times 10^{-6} mm^2$ respectively, despite having strikingly different compositions and thicknesses, with the influence of each of these factors unknown. When the gradient for both samples is compared, then they can easily be distinguished (2.56×10^{-7} and 1.13×10^{-6}mm for 2F and 3E respectively), with the gradient value now revealing information solely about the sample composition, rather than physical dimensions. *In vivo* tissues are irregular shapes, and therefore comparison of the scattering signal between tissues of different thickness needs to be made possible for quantitative analysis. To determine the gradient for *ex vivo* tissues, samples of multiple thickness can be imaged and then the gradient determined as above, however with *in vivo* tissue, this is not possible. Tissues of irregular thickness exist within the body, and the retrieved scattering values, along with estimated sample thicknesses maybe used to determine the relationship with thickness.

Validation of the accuracy and reliability of the three Gaussian retrieval method would ideally be required to preclude its continued use, and the lower SNR seen, along with the overall correlation between the ABI retrieved results and s_{image} goes some way to confirming this. There is no known reason as to why all silicone, along with the agarose and silica sphere phantoms offer a greater correlation than all other phantoms, as no clear similarities between the structures or composition of the three phantom types was found. On analysis, it was noted that the rocking curve during the ABI acquisition was not stable over time, meaning that the rocking curve at the start and the end of the data acquisition time varied. Furthermore, the raw data was noisier than anticipated, therefore the retrieved results can only be used to suggest a correlation, and further investigations would be required to confirm and explain such relationships.

The greater accuracy of the s_{image} results, along with the ability to retrieve very small scattering signals, with much lower noise levels than was previously possible[102,106] mean that the three Gaussian method should replace existing methods as the ongoing gold standard for scattering retrieval for EI-XPCi data.

9. Comparison of X-ray and Optical Scattering

After determining the optical and x-ray scattering properties of the phantoms created in chapter 6, via spectrophotometry and within the EI-XPCi system respectively, the results can be compared to determine whether a correlation can be seen. The predominant purpose of the phantoms was to refine the respective methods for measuring the scattering properties, therefore, to investigate the central hypothesis of this thesis, the correlation between optical and x-ray scattering for biological samples must be determined. This correlation was tested using porcine tissues which were imaged using OCT and EI-XPCi. OCT was used to extract spatially resolved optical scattering and the previously developed three Gaussian retrieval method was used to obtain the x-ray scattering values. Finally, the correlation between the x-ray and optical scattering properties for biological tissues was evaluated to determine whether XPCi offered a viable method for determining the optical scattering properties of a sample.

9.1. Phantoms

The methods used to measure both the optical and x-ray scattering signals for the phantoms, along with detailed discussion on the results are contained within 6.3. Results – Phantom Optical Properties Determination, and 8. Quantitative X-ray Scattering Measurement, of this thesis, respectively.

9.1.1. Results

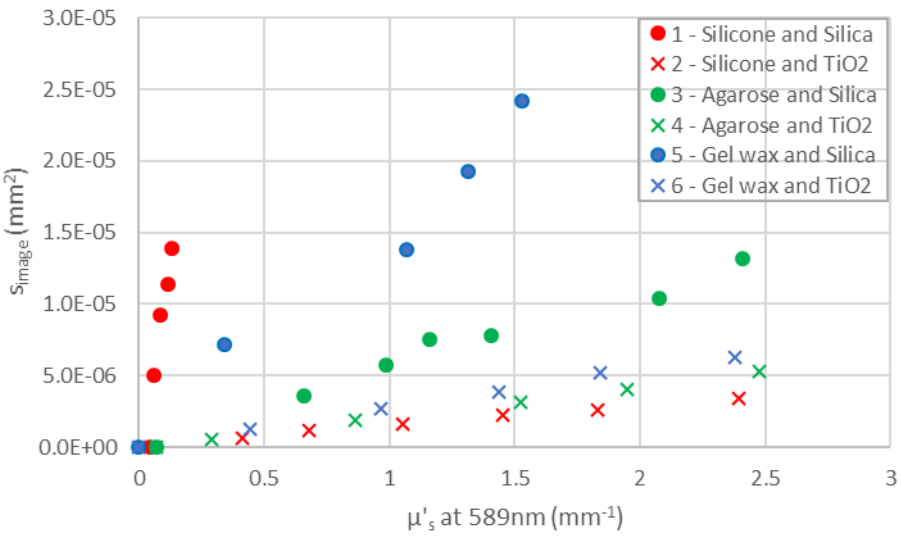

***Figure 53**. Relationship between the optical (μ'_s) and x-ray (s_{image}) scattering properties for all phantoms.*

The s_{image} values presented in Figure 53 are those acquired using the translated standard flat fielding technique for the 10mm thick phantom. If each of the phantom bulk material – scatterer combinations are considered in isolation, then as the optical scattering increases, so does the retrieved x-ray scattering, however if all samples are considered together then there is no clear correlation.

9.1.2. Discussion

There is no correlation between the optical and x-ray scattering values when all phantoms are considered, showing, that where artificial materials are concerned, the s_{image} values cannot be used to determine the μ'_s values. The scatterers used within the phantoms contain atoms of higher atomic number than are typically found within biological tissues, which are predominantly composed of Hydrogen, Oxygen, Nitrogen and Carbon[158,159]. Therefore, the δ values of the phantom materials are higher than would be expected for organic matter. Furthermore, the difference in δ values between scatterer and bulk material is quite large in the phantoms. In contrast, intracellular organelles, along with intra and extracellular fluids and matrices are composed primarily of a combination of these four atoms, along with very

small quantities of other trace elements, and therefore the differences in δ values between the *in vivo* scatterers, and the fluids in which they bathe in, would be expected to be considerably smaller than those produced by the phantoms. The same can be said for the difference in optical refractive index values (n). It is therefore reasonable to assume that a lack of correlation with phantom data, does not necessarily mean that a correlation does not exist with biological tissues. Despite the lack of correlation, phantoms with controlled scatterer concentration and geometry, as well as long term stability were essential to the development of the optical and x-ray experimental methods that are required for the subsequent evaluation of biological tissues.

Although the phantoms are unable to fully address the central hypothesis of this thesis, they have been useful in enabling development of the 'three Gaussian retrieval', an essential requirement for retrieval of the scattering signal from biological tissues. Reflecting on the design criteria of the phantoms, in order to contribute towards the proof of the central hypothesis, it may have been more appropriate to allocate greater importance to the tissue mimicking properties within the x-ray wavelengths. By creating phantoms that displayed both optical and x-ray tissue realistic properties, the relationship between x-ray and optical scattering within such phantoms may have given a better indication as to whether a correlation exists within biological tissues. As refraction, and therefore the scattering signal from the EI-XPCi system is at least partially dependent on differences in refractive index (δ), which, in turn is dependent on the electronic density of the material, choosing materials with similar, or identical chemical composition to biological tissues (carbon, oxygen, nitrogen and hydrogen) may infer a more tissue realistic scattering signal. Considering commonly used and available optical phantom materials (5. Introduction to Biomedical Phantoms), Intralipid, milk or leucocytes may have offered a more tissue realistic scattering medium in both optical and x-ray wavelengths, either embedded in agarose, or in their native liquid form. It should however be remembered that as the exact combination of properties that work to create a retrievable scattering signal in biological tissue are unknown, there is no guarantee that such organic materials would create any more of a tissue realistic x-ray signal than the materials considered within this thesis. Further work regarding the factors affecting the S_{image} value would be required before a truly tissue realistic x-ray scattering phantom may be made.

9.2. Biological samples

It should be noted that a manuscript is in preparation containing work presented in this subsection pertaining to the comparison of x-ray and optical scatter in biological tissues.

9.2.1. Materials and Methods

9.2.1.1. Samples

Samples of porcine kidney, liver, muscle, fat and skin were obtained from a butcher for imaging. Porcine tissue was chosen above other post mortem abattoir tissues due to the well-developed use of pigs as large animal models for human disease and physiology[211,212]. Skin and fat were chosen due to their high optical scattering, as reported in the literature[20,31], with liver, kidney and muscle chosen due to their commercial availability, and known ability to cause measurable optical scattering[20]. All tissue types also contain microscopic features (for example, skin – collagen fibres, fat - adipocytes, liver - hepatocytes and portal triad, kidney - glomeruli containing efferent and afferent arterioles, and muscle - muscle fibres) that have the potential to cause x-ray scattering when found at subpixel size. Prior to imaging, the upper surface of the sample was marked, to ensure that the tissue was orientated in the same direction for both optical and x-ray imaging. Samples were purchased from a butcher 24 hours prior to imaging, were stored in air tight containers in a refrigerator, and transported in a cool bag with ice blocks to maintain their freshness. For OCT imaging, a large piece of tissue, which was deemed to be representative of the organ which it was taken from, was placed on a glass slide, which was then directly placed onto the OCT sample stage (Figure 54).

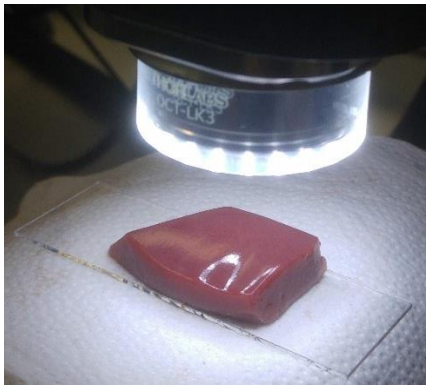

Figure 54*. Porcine kidney sample placed on a glass slide, on OCT sample stage.*

For use within the x-ray system, 3 thicknesses were created by either cutting a step shape into the tissue (kidney, liver and fat), placing 3 pieces of tissue of differing thickness next to each other (muscle), or layering the tissue on top of itself (skin) (Figure 55).

Figure 55. *(Left) Kidney, (Centre) Muscle and (right) fat tissue mounted on glass slides ready for x-ray imaging.*

9.2.1.2. OCT imaging

A liquid phantom consisting of Polybead® polystyrene microspheres (Cat. Number 07307-15, Polysciences, Inc., Hirschberg an der Bergstrasse, Germany) suspended in water was used as the calibration phantom. The microspheres were of mean diameter 0.51μm +/- standard deviation of 0.01μm and had a coefficient of variance 2%. The purchased concentration of 2.6% solids, corresponding to a μ_t of 9.47mm^{-1} and g of 0.4849 at 1300nm, was diluted with distilled water to reach the desired concentration of spheres to create a μ_t of 0.1024mm^{-1}, as calculated using Mie theory. The phantom mixture was made on the same day as the imaging was to take place to help ensure that the microspheres did not have time to aggregate, however, the spheres were vigorously pipetted into the imaging vessel to mix the sample.

The previously described Thorlabs Telesto II Spectral Domain OCT Imaging system (Thorlabs GmbH, Munich, Germany) was used to image the samples (7.1 Optical Coherence Tomography (OCT)). The focal plane was set at a depth of approximately 0.4mm from the top of the image on the OCT system, and a total of 500 x 500 A scans which corresponded to an area of 3.25mm x 3.90mm were obtained. The total A scan depth for all samples was 1.24mm, which was calculated assuming a refractive index of tissue[20,23,31,213]: $n_{tissues}$=1.4. The signal depth was corrected for using the refractive index of tissues, during analysis, but also on the OCT system, whilst obtaining the images. The sample was repositioned 4 times to obtain A scans from 4 different areas of the same tissue. The μ_t value was calculated for each of the 4 data sets for each tissue, with the mean of these 4 values used as the final value of μ_t for each tissue type. As tissue is scatter dominant, it is assumed that the value of μ_t is dominated by scattering, with negligible contribution by absorption, therefore μ_t was considered for biological tissues. Throughout the imaging of all samples, the reference arm position, as well as the fine and coarse focus were kept stationary, and samples were brought into focus by adjusting the axial position of the sample stage. The calibration phantom was imaged immediately after the tissue samples using the same imaging protocol, with the mean of all 4 areas used to create the calibration profile.

9.2.1.3. EI-XPCi

The previously described EI-XPCi system[102] at UCL was also used to obtain images of the biological samples. A molybdenum source operated at 40kV and 20mA was used along with the Hamamatsu C9732DK-11 detector (Hamamatsu Photonics, Hamamatsu City, Japan). Pixel size was 50μm^2, with a total field of view of 2400 x 2400 pixels over an area of 120mm^2. The sample and detector mask were manufactured by Creatv MicroTech (Potomac, MD, USA), with a pitch of 38μm and 48μm respectively, and aperture width of 12μm and 20μm, respectively. The IC was generated using 15 sample mask positions each with an exposure time of 1.2s. Sample and flat field images were acquired using 4 frames at 39 sample mask positions, each with an exposure time of 1.2s. The points were distributed symmetrically about the central mask position (the point of maximum pixel exposure), each 1μm apart, therefore covering the whole width of the

detector pixel. In this case, flat field images were obtained with no sample in place, and these alone were used during the analysis.

9.3. Results

9.3.1. OCT

All sample data was analysed using the methods previously described (7.2.3. Data analysis method), with linear fitting occurring over a 151.3µm depth (61 pixels). The depth at which this fitting occurred varied for each and, within each, sample, however fitting always occurred within the suspected single scattering region for each tissue type[10], with the single scattering region estimated from the inverse of the previously reported μ'_s values for biological tissues. Figure 56 shows average values of μ_t for each tissue type considered. The figure shows that muscle is the least scattering of the tissues considered, with fat the most scattering.

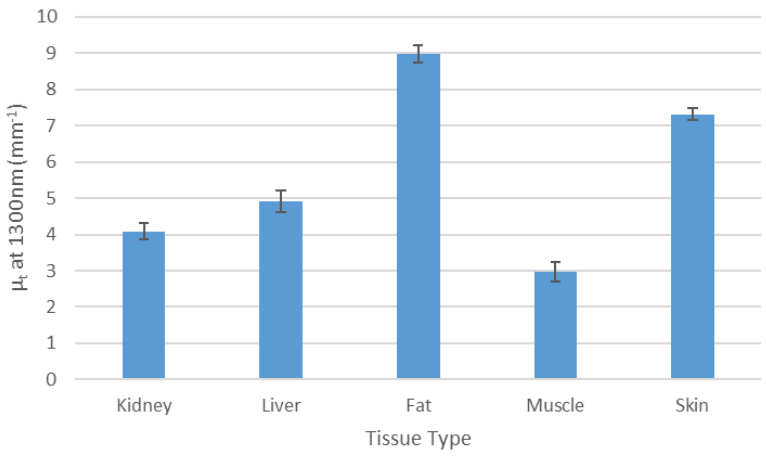

Figure 56. *Calculated μ_t value for each tissue type considered, as calculated via OCT. Error bars represent +/- 1 standard deviation*

If the g value of tissue is assumed to be 0.9, based on values reported in literature at 1300nm[20], then the values of μ'_s calculated from μ_t obtained from OCT, are similar to the values stated within literature for the tissue types considered[20,31].

9.3.2. EI-XPCi

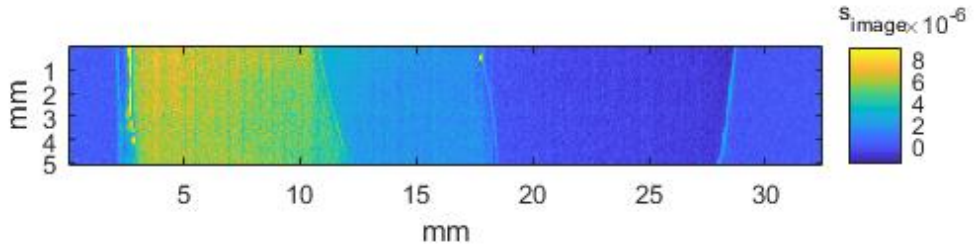

Figure 57. *Retrieved s_{image} map for kidney. The sample is orientated so that the thickest portion is on the left and the thinnest on the right. Areas with no sample ($s_{image} \approx 0 mm^2$) are visible both to the left and right of the image.*

The s_{image} value for each of the thicknesses of each tissue were retrieved using the previously developed standard flat fielding method of the 'three Gaussian Retrieval' method (8.3.2. 'Three Gaussian retrieval') with the detector area covered by each thickness determined from the retrieved s_{image} map (Figure 57). The thickness values were determined by taking the mean of 5 consecutive measurements, obtained using digital callipers. The s_{image} values quoted from now on are the mean value of all retrieved pixels for each thickness.

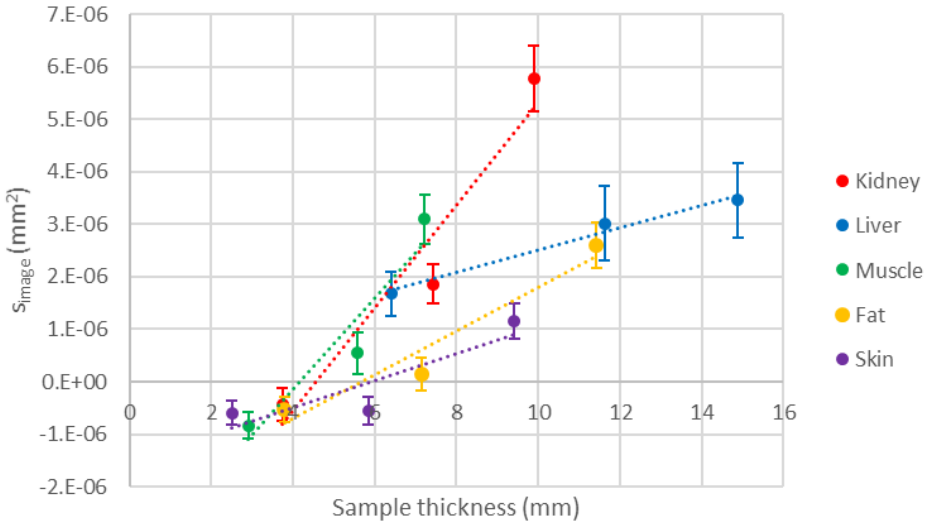

Figure 58. *s_{image} values retrieved for all thicknesses for each tissue type, along with the lines of best fit from which the gradients are calculated. Error bars are +/- 1 standard deviation.*

The thickness independent scattering value (i.e. gradient) of each tissue type was obtained as previously described, (8.4.3.1. Thickness independent

scattering parameter) by plotting the s_{image} value against the thickness of the sample. Table 10 shows that liver produces the lowest x-ray scattering, whist kidney produces the highest.

Sample	Gradient (mm)
Kidney	9.79×10^{-7}
Liver	2.14×10^{-7}
Muscle	8.72×10^{-7}
Fat	4.17×10^{-7}
Skin	2.56×10^{-7}

Table 10. *Thickness independent scattering value (i.e. gradient) for each tissue type, determined using the graph in Figure 58.*

9.3.3. X-ray vs. Optical Scattering

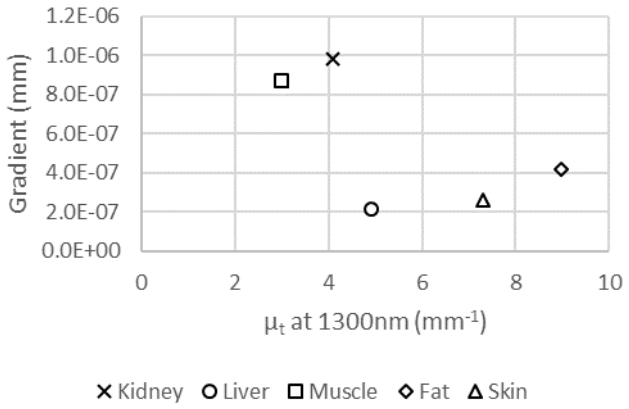

Figure 59. *Comparison of optical (μ_t) and x-ray (gradient) scattering in biological tissues*

The is no correlation between the optical and x-ray scattering, with the two mostly highly scattering tissues, as measured by EI-XPCi, being the two least scattering as measured by OCT. Although both x-ray and optical scatter are both caused by microscopic variations in refractive index, the scattering at both wavelengths appears not to be linked.

9.4. Discussion

As the g value of the considered tissue types was not directly measured, the μ_t values were used for analysis as they are unaffected by tissue anisotropy. Knowledge of g is required for accurate calculation of $\mu'_s{}^{10}$, therefore this value will contain error associated with estimation of g. Fat and skin are

typically reported as some of the highest optically scattering biological tissues,[20] a result replicated here. Skin is commonly higher scattering than fat[20], however results generated here demonstrate a higher μ_t for fat than skin. The value of μ_t represents both the absorption and scattering by a sample, with fat being one of the main chromophores within biological tissues[214]. Therefore, a tissue with a high concentration of fat may demonstrate non-negligible absorption. If the μ_a of fat is known, then the pure scattering component of the sample can be calculated from μ_t. The inability to accurately correct for sometimes non-negligible absorption is another reason why μ_t is considered for analysis rather than trying to convert to μ'_s.

There are no previous reports of the quantitative x-ray scattering values of the tissues within this chapter using the EI-XPCi system, therefore, although it is assumed that subpixel differences in δ exist, the cause of these differences, and therefore the reason for the different scattering values remains unexplored. The x-ray scattering signal occurs as a result of subpixel inhomogeneities in delta value, and structures that are known to cause optical scattering, such as whole cells, organelles such as nuclei and mitochondria, and cell membranes[20] are also likely sources of x-ray scatter, as well as other subpixel structures within the tissue. Liver parenchyma is relatively homogeneous, with hepatocytes making up 80% of the tissue bulk[215]. The portal triad is an important functional unit of the liver, and consists of a bile duct, portal vein and hepatic artery. These structures are potential sources of x-ray scatter, however are not always found to be subpixel size[216,217], and are only found at a relatively low concentration[217] of 0.8 portal triads per mm^2 of liver. The cortex of the kidney was imaged due to the macroscopic homogeneity of the tissue. The kidney cortex contains hundreds of thousands of densely packed glomeruli at a high concentration[218] of approximately 100 per $0.6mm^2$. Glomeruli are tight knots of blood vessels, arranged as such for the ultrafiltration of blood. Glomerular capillaries have diameters smaller than the size of the pixels[219,220] and are therefore a potential source of scattering. The liver and kidney tissue demonstrate the lowest and highest x-ray scatter, respectively. The relatively low and high concentration of subpixel structures other than intracellular organelles in liver and kidney, respectively, explains the calculated gradient value, and therefore x-ray scattering noted in both tissue types.

The gradient value, which was previously validated using the scattering phantoms (8.4.3.1. Thickness independent scattering parameter), has been calculated here using three different tissue thicknesses, however for greater accuracy, it would be prudent to image a greater range of thicknesses. Unfortunately, the field of view of the x-ray system (approximately 4cm^2) limits the width of a sample, and therefore the range of thicknesses, that can be concurrently imaged. Concurrent imaging is not necessary, however by enabling imaging of multiple thicknesses at the same time, it would reduce the number of exposures required to obtain a full data set of all required thicknesses. A feasible alternative method for determining the gradient parameter would be to cut a wedge shape of tissue as in Figure 60, and then determine the gradient from the lateral profile of the retrieved s_{image} values. This method, however, relies on the accurate and smooth cutting of a wedge shape, and so it likely to be technically more difficult than cutting the shapes shown in Figure 55. Furthermore, the fragile nature of biological tissues may make the tip of such a wedge prone to damage and desiccation. This is however, a method of tissue preparation that could be explored to improve the accuracy of the derivation of the gradient parameter.

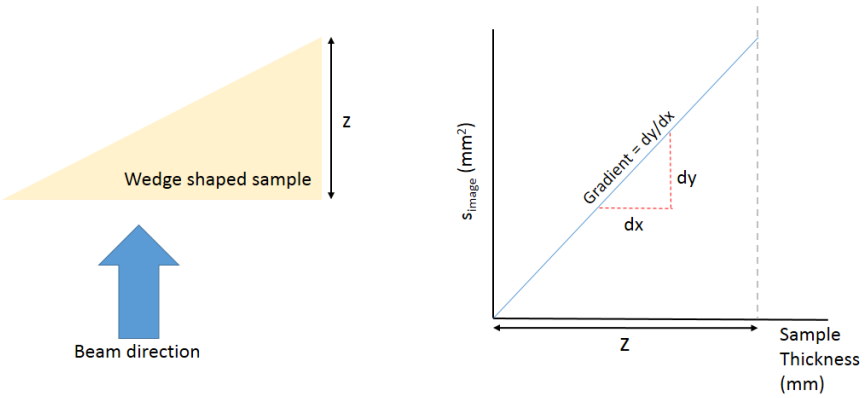

Figure 60. *Possible future method of determining the gradient parameter with greater accuracy. An example signal is displayed, along with the method for obtaining the gradient parameter.*

If all samples are considered together, there is no correlation between x-ray and optical scatter in biological tissues, with the two lowest optically scattering tissues demonstrating the highest x-ray scatter, therefore the initial hypothesis has been disproven and the null hypothesis cannot be rejected. Despite this lack of direct correlation, based on the limited sample data available, there are two groups (group 1 consists of kidney and muscle, and

group 2 consists of skin, fat and liver) of tissue which are potentially distinguishable when x-ray and optical properties are considered, and these two groups, individually, show correlations between x-ray and optical scattering. Although this suggested correlation could be present when specific tissue types are considered, care should be taken not to draw conclusions of this sort from only 5 data points. To confirm whether such tissue groups exist, further tissue types should be considered, and each sample should be sent for histopathological analysis to determine the size and type of subpixel structures present.

The reasons for lack of correlation between optical and x-ray scattering signals in biological tissue may be multifactorial but remains largely unexplored within this body of work. As discussed in previous chapters, scattering at both wavelengths is due to micron scale variations in refractive index, with the refractive index being the sum of electronic scattering from within a sample – the same mechanism regardless of the wavelength considered. Electronic scattering is dependent on both the electron density (non-wavelength dependent) and resonant frequencies (function of wavelength) of the atoms within a sample, with the former assumed to be a significant factor in determining the optical and x-ray scattering. The results here may suggest that this assumption is not correct, and the resonant frequencies of the atoms within biological tissues are in fact relevant in determining scattering. Further reason for the lack of correlation may be a fundamental error in the assumption that the structures that cause scattering within biological tissues are the same for both wavelengths. The structures known to cause optical scattering are well defined (for example nuclei or collagen fibres)[20], however those that cause x-ray scattering in the EI-XPCi system remain unknown, as discussed above. Further work required to determine the cause of the x-ray scattering signal, and therefore further understand the lack of correlation seen here, with ideas for future work explored in the subsequent chapter 10.6 Suggestions for Future Work.

Finally, correlation may not be present due to tissue handling and storage artefacts. As discussed previously, the optical scattering of *ex vivo* tissues vary from the *in vivo* values for the same tissue type (2.3.2. *ex vivo* measurements). Due to the exposure to radiation, and the ethical considerations this would entail, the use of live animals and therefore the

collection of *in vivo* data would not be possible within the EI-XPCi system. Focus should therefore be on obtaining as fresh a tissue sample as possible, preferably multiple samples from the same animal to ensure that the physiological conditions of the tissues were all the same prior to euthanasia. Post mortem tissues obtained from a butcher were used within this study due to the ease of sourcing samples in this way, therefore uncertainty in both the optical and x-ray scattering values was introduced due to this. It is unknown how the retrieved x-ray scattering values are affected by the freshness of the tissue, however if scattering is, as suggested, a result of cellular structures, then cells may dehydrate and shrink over time, with the reduced water content also affecting the δ value. Both the size of the scattering structure and the δ value are important in determining the scattering signal, therefore the retrieved values may differ from *in vivo* tissues. This limitation in itself is enough to prevent the null hypothesis from being rejected, and further work must be performed to determine the effect of tissue handling and storage on the x-ray scattering properties (10.6 Suggestions for Future Work), and to confirm or dispute the lack of correlation seen within this thesis.

9.5. Conclusion

The results presented in this chapter go some way to rejecting the hypothesis that there is a correlation between the optical and x-ray scattering signals of biological tissues. Limitations of the experimental design, such as phantom design, tissue handling, tissue freshness and a limited data set preclude the definitive rejection or acceptance of the hypothesis, however the suggested lack of correlation has provided an excellent starting point for further investigations into the origin of the x-ray scattering signal which will enable in depth understanding of the relationship between scattering in the two different wavelengths.

10. Conclusions and Future Work

The work presented within this thesis explores whether the scattering signal retrieved from x-ray phase contrast imaging can be used to estimate the optical scattering within biological tissues. Accurate knowledge of the scattering properties of tissues are required to make imaging methods such as photoacoustic tomography fully quantitative. However, there is currently no reliable way of obtaining, either through measurement or the use of reference data, three-dimensional distributions of the optical scattering coefficient in thick sections of biological tissues. If the edge illumination x-ray phase contrast imaging method (EI-XPCi) was able to be used to acquire such three-dimensional distributions of the optical scattering coefficient, then whole small animals could be quantitatively imaged *in vivo*, creating scattering maps of all tissues within the sample. This would enable the further development of functional and molecular imaging techniques that are reliant on accurate quantitative knowledge of optical scattering within relevant tissues. This chapter outlines the conclusions drawn from this thesis, highlighting where advancements in the field or novel work has been performed. Finally, further work required to confirm the conclusions drawn within this thesis are discussed.

10.1. Multimodal Phantom Manufacture

Gel wax, agarose and silicone were used as phantom bulk materials, embedded with either SiO_2 microspheres or TiO_2 powder, to create optical scattering phantoms. Phantoms were developed to enable refinement of both optical and x-ray scattering measurement methods, therefore their stability and reproducibility was paramount. Silicone and agarose both have extensive histories of use within phantom manufacture[112,113], however gel wax is a newer, novel, paraffin wax based material, which has only recently been suggested as a suitable optical phantom material[174,221,222]. Methods for the manufacture of silicone, agarose and gel wax phantoms were developed to reduce aggregation of scattering particles to ensure a homogeneously scattering phantom.

The method used to create silicone phantoms was more complex than both the agarose and gel wax manufacturing methods. This is in part due to the difficulty in achieving silicone phantoms free from scatterer aggregates,

notable when 1μm diameter silica microspheres were used as the scatterer. However, the complexity of the method is also because of steps taken to reduce aggregation causing associated problems with adsorption and phantom shrinkage. The manufacturing protocol developed within this thesis has been shown to create decreased scatterer aggregation compared to the initially investigated method, and reliably and reproducibly manufactures silicone phantoms with silica microspheres or TiO_2 powder as scatterers. The work pertaining to the improvement in manufacturing method, along with the associated data demonstrating the reduction in scatterer aggregation was published: Charlotte J. Maughan Jones, Peter R. T. Munro, "Development of a reliable and reproducible phantom manufacturing method using silica microspheres in silicone," J. Biomed. Opt. 22(9) 095004 (18 September 2017).

The presented methods for gel wax, agarose and silicone phantoms were also reliable and reproducible, and created phantoms with predictable and biologically relevant optical scattering. Finally, each phantom material combination was able to be cast in a variety of shapes, with phantoms of approximately 1mm thick made for optical imaging purposes, and those of approximately 2, 4, 6 and 10mm for x-ray imaging, demonstrating the flexibility to use such phantom materials for a variety of imaging purposes.

10.2. Phantom Stability

The repeated use of phantoms over a prolonged time requires them to be stable with respect to their optical scattering properties. To assess this, phantoms of each scatterer and bulk material combination were measured periodically over an approximate two-year period using spectrophotometer and IAD. Results for all phantoms except for those composed of gel wax and silica microspheres showed good stability over the period considered. Gel wax and silica microsphere phantoms, of all scatterer concentrations, all showed a decrease in μ'_s, of between 47% and 72% from their initial μ'_s values. This is thought to be due to migration of the charged silica microspheres within the semi-solid gel wax matrix. The work presented on gel wax phantom instability was published as follows: Charlotte J. Maughan Jones and Peter R. T. Munro, "Stability of gel wax based optical scattering phantoms," Biomed. Opt. Express 9, 3495-3502 (2018)

Agarose phantoms are typically considered to have a short life span, of the order of days to weeks[112,113], due to their predisposition to dehydration when not stored adequately, however, unexpected results presented here demonstrate that if stored submerged in tap water at room temperature, agarose phantoms do not significantly degrade with respect to their μ_s' values over a two year time period. Their prolonged use in optical imaging techniques is only precluded by their fragility and subsequent degradation due to repeat handling, therefore agarose has now been shown to be a viable long-term phantom option.

10.3. X-ray Scattering Retrieval

To obtain the pure scattering component of an image obtained using the edge illumination x-ray phase contrast (EI-XPCi) system at UCL, signal retrieval must be performed. Previous methods involve tracking the broadening of the so called beamlets (and therefore illumination curve (IC)) as they traverse a sample. The IC is commonly modelled as a single Gaussian curve[102,106], however such an approach was unable to detect scattering within the 10mm thick phantom samples, especially in those considered highly absorbing (silicone phantoms) or low scattering (all containing TiO_2 as a scatterer), with negative scattering values or values below the noise level of the system obtained. The origin of such values was absorption and beam hardening caused by the sample, as well as incomplete detector mask absorption, therefore a novel method of retrieval was developed, which overcame these issues.

10.3.1. Three Gaussian Retrieval

The three Gaussian retrieval method fits Gaussians to data from each of three adjacent pixels, which allows for accurate modelling of the tails of the beamlets, accounting for adjacent pixel interaction due to incomplete mask absorption. Correcting for the sample absorption and associated beam hardening can also be done, by utilising the alternative flat fielding method – using the non-scattering sample to perform the flat fielding corrections. Alternatively, a standard flat fielding method can be applied, and the results rigidly translated so that a sample with no scatterers, has a retrieved x-ray scattering value of $0mm^2$. Both the alternative and standard translated flat fielding methods produce identical results, therefore either method has been shown to be valid. It has also been shown, that if only 3 sample mask

positions per pixel are used (i.e. a total of 9 points over the three Gaussians), then the x-ray scattering values are comparable to those obtained with 33 points per Gaussian – important in reducing dose if dose sensitive samples are to be imaged. Previous retrieval methods[102,106] were unable to successfully retrieve a quantitative scattering value from low scattering and highly absorbing samples, such as those composed of silicone and TiO2 powder, however, the x-ray scattering (s_{image}) value from samples of very low scattering and high absorption were successfully retrieved using the three Gaussian retrieval method.

The work presented regarding the development of the novel three Gaussian method, demonstrating its use in low scattering and high absorbing samples was published as follows: Charlotte J. Maughan Jones and Peter R. T. Munro, "Stability of gel wax based optical scattering phantoms," Biomed. Opt. Express 9, 3495-3502 (2018)

10.3.2. Thickness Independent Scattering Parameter

Work on developing the three Gaussian method was performed on 10mm thick x-ray phantom samples, however, scattering by the approximately 2, 4 and 6mm thick samples was used to decouple the scattering value (s_{image}) from the physical thickness of the sample. As the thickness of the sample increases, then the s_{image} value also increases when the standard translated flat field is considered for each phantom, therefore demonstrating the s_{image} dependence on sample thickness. This novel value, known as the 'thickness independent scattering value' (or 'gradient'), was calculated by plotting the retrieved s_{image} value against the corresponding thickness of the sample from which it was retrieved, applying a line of best fit, and calculating the gradient of this line. The gradient is subsequently used as the thickness independent scattering parameter. This was performed for each scatterer concentration of each bulk material-scatterer combination, to obtain a thickness independent scattering value for each phantom, which is dependent solely on the composition and scatterer concentration of the sample, and not the physical dimensions. This value is of most use when imaging biological tissues, where the retrieved s_{image} values between 2 different organs of different thickness would not be comparable.

10.3.3 Analyser Based Imaging (ABI)

The biomedical beam line at the ESRF facility was employed to image 10mm thick x-ray phantoms using analyser-based imaging. The scattering values were retrieved using a previously published method[84], and the values compared to s_{image} retrieved from the EI-XPCi system, for each 10mm thick sample. An overall positive correlation can be seen between the retrieved scattering from both methods. However, due to a two-month period between collecting the two sets of data as well as instability in the ABI system, the results are suggestive of, rather than confirmatory of a correlation between the two methods. Further investigations would therefore be required to confirm and explain such a relationship. Direct quantitative comparison between retrieved results from the two different XPCi systems had not previously been performed.

10.4. Optical Coherence Tomography

Optical coherence tomography (OCT) has a well published history of use in the determination of tissue optical properties, with methods based on monitoring the optical signal decay over the depth of the sample. Many established methods exist for data analysis, therefore modifications were made to an existing method of optical property measurement[10] to allow analysis of biological tissues in the OCT system available at UCL (Thorlabs Telesto II Spectral Domain OCT Imaging system (Thorlabs GmbH, Munich, Germany)). The method was initially developed via the use of previously designed phantoms, and latterly confirmed for its biological suitability, by using porcine muscle and fat. Modifications were introduced to process the image to allow the imaging of, and subsequent determination of the attenuation coefficient (μ_t) of, multiple irregular biological tissue samples. The surface of the object was located by determining where the peak created by the strong back scatter at the air-tissue interface was. The top of the sample was then moved to the top of the image for all areas of the sample, making averaging all A scans within the C scan volume possible, and therefore analysis more reliable. The depth profile of intensity was subsequently corrected for system constants, using a low scattering correction phantom, and a linear model fit to the data to enable calculation of the sample μ_t. To analyse the accuracy of the modified method, the μ_t values obtained from the OCT system were converted to μ'_s. The μ'_s values of the scattering phantoms,

were found to be comparable to those obtained at 1300nm using spectrophotometry, and those of porcine fat and muscle were found to be within the range of previously published results[20], demonstrating the reliability of the method.

10.5. X-ray and Optical scattering comparison

Porcine muscle, fat, skin, liver and kidney tissue were all obtained from a butcher for both quantitative OCT and EI-XPCi imaging, with both imaging modalities performed on the same day. Tissues were all obtained 24 hours prior to imaging and were kept chilled to maintain the freshness of the samples as much as possible.

Samples were initially imaged using the OCT system and their μ_t values calculated. The reliability of the analysis method was again demonstrated by converting the obtained μ_t to μ'_s, and noting that the values for each tissue type were comparable to those reported in the literature at the same wavelength[20] (1300nm, the central wavelength of the OCT system). X-ray images using the edge illumination system were subsequently obtained using samples of three different thickness. X-ray scattering values were retrieved using the three Gaussian retrieval, and the thickness independent scattering value (also known as the Gradient) calculated, showing that kidney was the most, and liver the least scattering of the considered tissues in the x-ray wavelengths.

Finally, the optical and x-ray scattering properties were compared for both the previously manufactured phantoms and the biological tissues to determine whether a correlation exists. For the phantoms, the s_{image} (x-ray – EI-XPCi) and μ'_s at 589nm (optical – spectrophotometer) were compared, and for the biological tissues, the thickness independent scattering value (x-ray – EI-XPCi) and μ_t (optical – OCT) at 1300nm were compared. Despite scattering in both the x-ray and optical wavelengths being due to microscopic variations in refractive index, no correlation could be seen between the scattering values with either the scattering phantoms or the biological tissues.

A manuscript is currently in preparation containing the results of the comparison of x-ray and optical scattering in biological tissues as presented in Chapter 8 of this thesis.

10.6 Suggestions for Future Work

Now that the optical stability of all bulk material and scatterer combinations has been determined, with the instability of gel wax and silica microspheres clearly presented, if such phantoms are to continue to be applied in x-ray imaging, then their x-ray stability should also be determined. As the samples are not dose sensitive, repeat imaging can be performed without fear of destruction, and the x-ray stability can be determined over a similarly prolonged time period as was the optical stability.

The work presented within this thesis goes some way to confirming that there is no correlation between optical and x-ray scattering in biological tissues, however manufacture of phantoms which have both tissue realistic x-ray and optical properties could further confirm this result. As discussed in 9.1.2. Discussion, phantoms composed of organic materials, for example Intralipid, could be employed to assess the relationship further. As discussed in section 9.4. Discussion, although there is no overall correlation between optical and x-ray scattering, 2 different identifiable tissue groups possibly exist, however with the small sample size of 5 different tissue types, conclusive evidence either way is not yet available. To investigate this further, multiple different fresh tissues should be imaged using both the OCT and EI-XPCi systems, to explore any potential correlation further. In the absence of available human tissue, porcine tissue should continue to be used due to its close physiological and anatomical similarity to human tissue, but also due to its wide availability as abattoir material, therefore reducing the ethical considerations of using animal or human tissues (complying with the 3R's principle of animal research). Subsequently, tissues from different species could be investigated to identify any differences in x-ray scattering signal or confirm any correlation. Only after optically and x-ray imaging multiple different tissue types can it be confirmed whether any correlation involving different tissue groups exists.

Multiple different methods to perform x-ray phase contrast imaging are available[8,74], however a quantitative comparison of the scattering retrieval from different imaging has not yet been performed for ABI and EI-XPCi. Preliminary evidence of a correlation between ABI and EI-XPCi scattering has been presented within this thesis however, as discussed, due to the instability of the ABI rocking curve during image acquisition, the correlation

between the two imaging methods is suggested, rather than confirmed, therefore efforts should be focused on repeating this experiment. To ensure the resulting data sets are as comparable as possible, and to prevent any errors related to natural degradation of the samples, the two imaging methods should be performed as close in time as possible on the same sample. Due to the different geographical location of the two systems, imaging on the same day may not be possible, unless the edge illumination system could be taken to the synchrotron, however, if this was not possible, then performing the experiments within a week of each other should be feasible.

Prior to repeating the above experiments, the effect of tissue handling and storage on the x-ray scattering properties should be determined. To do this, fresh tissue samples should be obtained as soon after euthanasia as possible. Tissue should then be immediately refrigerated, and the scattering signal obtained from the EI-XPCi system. Images of the same tissues can then be obtained, and scattering signal retrieved every 24 hours for a week (or until putrefaction precludes further use). The comparison of s_{image} obtained over time from the same tissue sample will aid the design of future experimental protocols and the understanding of results obtained. This may also be expanded by storing tissue samples from the same animal in a variety of ways (for example, fixed in formalin, frozen, refrigerated or left at room temperature) and comparing the x-ray scattering properties, therefore determining a gold standard method of tissue handling with regards to EI-XPCi imaging.

The edge illumination system at UCL has already been used in a variety of applications, including biomedical imaging of breast[103] and lung tissue[107], as well as industrial purposes such as composite material testing[109] and security scanning[223], however this thesis is the first presentation of comparative scattering values of multiple tissues from the same species. To further this body of work, it would be suggested to image and retrieve the scattering values from multiple other tissue types, and from different species to enable a body of values to be established. By obtaining the different scattering values for different tissue types, it would also further the knowledge of the subpixel structure of such tissues and would allow greater understanding of the origin of the scattering signal from biological tissues. If fresh tissues are imaged within the EI-XPCi system, and then fixed and stained ready for

histopathological examination, then the microscopic structure, along with, for example, the mitochondrial or nuclear density (two organelles that could possibly cause x-ray scattering) could be compared to the scattering signal, to understand which structures within the tissues are the most important, when predicting x-ray scattering. Understanding the origin of the x-ray scattering signal in biological tissues would also aid in the understanding of the differences in the origin of, and proposed lack of correlation between x-ray and optical scattering. Furthermore, modelling of scattering within the EI-XPCi system would be required, along with experimental results, to link measured signals to the underlying cellular ultrastructure. If the main causes of scattering in tissue can be determined, then EI-XPCi may be used in biomedical research imaging involved in human diseases where, for example, decreases in mitochondrial number are pathognomonic, such as Alzheimer's disease[224–226], or economically important animal diseases, such as polysaccharide storage myopathy in equine patients[227].

Bibliography

1. C. J. Maughan Jones and P. R. T. Munro, “Development of a reliable and reproducible phantom manufacturing method using silica microspheres in silicone,” *J. Biomed. Opt.* **22**(09), 1–5 (2017) [doi:10.1117/1.JBO.22.9.095004].

2. S. Bohndiek, “Addressing photoacoustics standards,” *Nat. Photonics* **13**(5), 298–298 (2019) [doi:10.1038/s41566-019-0417-3].

3. C. J. Maughan Jones and P. R. T. Munro, “Stability of gel wax based optical scattering phantoms,” *Biomed. Opt. Express* **9**(8), 3495 (2018) [doi:10.1364/boe.9.003495].

4. C. J. Maughan Jones et al., “Retrieval of weak x-ray scattering using edge illumination,” *Opt. Lett.* **43**(16), 3874 (2018) [doi:10.1364/ol.43.003874].

5. P. Beard, “Biomedical photoacoustic imaging.,” *Interface Focus* **1**(4), 602–631 (2011).

6. B. Cox et al., “Quantitative spectroscopic photoacoustic imaging: a review.,” *J. Biomed. Opt.* **17**(6), 061202 (2012).

7. B. Cox, J. Laufer, and P. Beard, “The challenges for quantitative photoacoustic imaging,” *Proc. SPIE, Photons Plus Ultrasound Imaging Sens.* **7177**, 1–9, SPIE-INT SOC OPTICAL ENGINEERING (2009).

8. A. Olivo and E. Castelli, “X-ray phase contrast imaging: From synchrotrons to conventional sources,” *Riv. del Nuovo Cim.* **37**(9), 467–508 (2014).

9. P. Gong, “Assessment of human burn scars with optical coherence tomography by imaging the attenuation coefficient of tissue after vascular masking,” *J. Biomed. Opt.* **19**(2), 021111 (2013) [doi:10.1117/1.jbo.19.2.021111].

10. L. Scolaro et al., “Parametric imaging of the local attenuation coefficient in human axillary lymph nodes assessed using optical coherence tomography,” *Biomed. Opt. Express* **3**(2), 366 (2012) [doi:10.1364/boe.3.000366].

11. A. G. Bell, “Production of Sound by Radiant Energy,” *Science (80-.).* **2**(49), 242–253 (1881).

12. A. G. Bell, “Upon the production and reproduction of sound by light,” *J. Soc. Telegr. Eng.* **9**(34), 404–426 (1880).

13. R. A. Kruger, “Photoacoustic ultrasound,” *Med. Phys.* **21**, 127 (1994).

14. R. O. Esenaliev et al., “Laser optoacoustic imaging for breast cancer diagnostics: limit of detection and comparison with x-ray and ultrasound imaging,” in Proc. of SPIE **2979**, pp. 71–82 (1997) [doi:10.1117/12.280213].

15. A. A. Oraevsky et al., “Laser optoacoustic tomography for medical diagnostics: principles,” in SPIE Proceedings **2676**, pp. 22–31 (1996) [doi:10.1117/12.238786].

16. R. Li et al., “Label-free in vivo imaging of peripheral nerve by multispectral photoacoustic tomography,” *J. Biophotonics* **9**(1–2), 124–128 (2016).

17. L. Lin et al., “In vivo photoacoustic tomography of myoglobin oxygen saturation,” *J. Biomed. Opt.* **21**(6), 061002 (2015).

18. X. Liu et al., “Optical coherence photoacoustic microscopy for in vivo multimodal retinal imaging,” *Opt. Lett.* **40**(7), 1370–1373 (2015).

19. D.-K. Yao et al., “Photoacoustic measurement of the Grüneisen parameter of tissue.,” *J. Biomed. Opt.* **19**(1), 17007, International Society for Optics and Photonics (2014).

20. S. L. Jacques, “Optical properties of biological tissues: a review.,” *Phys. Med. Biol.* **58**(11), R37–R61 (2013) [doi:10.1088/0031-9155/58/11/R37].

21. P. R. T. Munro, “Coherent X-ray imaging across length scales,” *Contemp. Phys.* **7514**, 1–20, Taylor & Francis (2017).

22. J. Stritzel, M. Rahlves, and B. Roth, “Refractive-index measurement and inverse correction using optical coherence tomography,” *Opt. Lett.* **40**(23), 5558 (2015).

23. G. J. Tearney et al., “Determination of the refractive index of highly scattering human tissue by optical coherence tomography,” *Opt. Lett.*

20(21), 2258 (1995).

24. J. C. Hebden et al., “A soft deformable tissue-equivalent phantom for diffuse optical tomography.,” *Phys. Med. Biol.* **51**(21), 5581–5590 (2006).

25. J. R. Lorenzo, “Chapter 2. Scattering and Absorption,” in Principles of Diffuse Light Propagation, pp. 53–88, World Scientific Publishing Co Pte. Ltd. (2012).

26. S. A. Prahl, “Everything I think you should know about inverse adding doubling,” 2011, <http://omlc.ogi.edu/software/iad>.

27. M. S. Wróbel et al., “Measurements of fundamental properties of homogeneous tissue phantoms,” *J. Biomed. Opt.* **20**(4), 045004 1-10 (2015).

28. D. Fukutomi, K. Ishii, and K. Awazu, “Determination of scattering coefficient considering wavelength and absorption dependence of anisotropy factor measured by polarized beam for biological tissues,” *Opt. Rev.* **9792**, 97920T, The Optical Society of Japan (2015).

29. J. R. Lorenzo, “Chapter 1. Light Absorbers, Emitters and Scatterers: The Origins of Color in Nature,” in Principles of Diffuse Light Propagation, pp. 3–51, World Scientific Publishing Co Pte. Ltd. (2012).

30. Jacques, Alter, and Prahl, “Angular dependence of HeNe laser light scattering by human dermis,” in Lasers Life Sci **1**, pp. 309–333 (1987).

31. A. N. Bashkatov, E. A. Genina, and V. V. Tuchin, “Optical Properties of Skin, Subcutaneous, and Muscle Tissues: a Review,” *J. Innov. Opt. Health Sci.* **04**(01), 9–38 (2011).

32. S. J. Matcher, M. Cope, and D. T. Delpy, “In vivo measurements of the wavelength dependence of tissue-scattering coefficients between 760 and 900 nm measured with time-resolved spectroscopy,” *Appl. Opt.* **36**(1), 386, Optical Society of America (1997) [doi:10.1364/AO.36.000386].

33. S. A. Prahl, “Mie Scattering Calculator,” 2007,

<http://omlc.ogi.edu/calc/mie_calc.html>.

34. M. Firbank, M. Oda, and D. T. Delpy, “An improved design for a stable and reproducible phantom material for use in near-infrared spectroscopy and imaging,” *Phys.Med.Biol.* **40**, 955–961 (1995).

35. I. S. Saidi, S. L. Jacques, and F. K. Tittel, “Mie and Rayleigh modeling of visible-light scattering in neonatal skin.,” *Appl. Opt.* **34**(31), 7410–7418 (1995).

36. M. Xu, T. T. Wu, and J. Y. Qu, “Unified Mie and fractal scattering by cells and experimental study on application in optical characterization of cellular and subcellular structures,” *J. Biomed. Opt.* **13**(2), 024015 (2008).

37. C. F. Bohren and D. M. Huffman, *Absorption And Scattering of Light By Small Particles*, in Absorption And Scattering of Light by Small Particles, Wiley Interscience, New York (1983).

38. H. Liu et al., “Dependence of Tissue Optical Properties on Solute-Induced Changes in Refractive Index and Osmolarity,” *J. Biomed. Opt.* **1**(2), 200–211 (1996).

39. S. L. Jacques, “Origins of tissue optical properties in the UVA, Visible, and NIR regions,” in OSA TOPS on Advances in Optical Imaging and Photon Migration **2**, pp. 364–371 (1996).

40. J. L. Sandell and T. C. Zhu, “A review of in-vivo optical properties of human tissues and its impact on PDT.,” *J. Biophotonics* **4**(11–12), 773–787 (2011) [doi:10.1002/jbio.201100062].

41. E. Salomatina and a N. Yaroslavsky, “Evaluation of the in vivo and ex vivo optical properties in a mouse ear model.,” *Phys. Med. Biol.* **53**, 2797–2807 (2008).

42. J. W. Pickering et al., “Double-integrating-sphere system for measuring the optical properties of tissue.,” *Appl. Opt.* **32**(4), 399–410 (1993).

43. S. A. Prahl, M. J. C. van Gemert, and A. J. Welch, “Determining the optical properties of turbid media by using the adding-doubling method.,” *Appl. Opt.* **32**(4), 559–568 (1993).

44. P. Lemaillet et al., “Double-integrating-sphere system at the National Institute of Standards and Technology in support of measurement standards for the determination of optical properties of tissue-mimicking phantoms,” *J. Biomed. Opt.* **20**(12), 121310 (2015).

45. Z. Fujiwara et al., “Measurement of Scattering Coefficient in PMMA with SiO2 Particles By Optical Coherence Tomography,” in 17th Microoptics Conference, The Japan Society of Applied Physics, Sendai, Japan (2011).

46. V. M. Kodach et al., “Determination of the scattering anisotropy with optical coherence tomography.,” *Opt. Express* **19**(7), 6131–6140 (2011) [doi:10.1364/OE.19.006131].

47. K. Takada et al., “New measurement system for fault location in optical waveguide devices based on an interferometric technique,” *Appl. Opt.* **26**(9), 1603 (1987) [doi:10.1364/ao.26.001603].

48. R. C. Youngquist, S. Carr, and D. E. N. Davies, “Optical coherence-domain reflectometry: a new optical evaluation technique,” *Opt. Lett.* **12**(3), 158 (1987) [doi:10.1364/ol.12.000158].

49. G. Vizzeri et al., “Agreement between spectral-domain and time-domain OCT for measuring RNFL thickness,” *Br. J. Ophthalmol.* **93**(6), 775–781 (2009) [doi:10.1136/bjo.2008.150698].

50. D. Thomas and G. Duguid, “Optical coherence tomography - a review of the principles and contemporary uses in retinal investigation,” *Eye* **18**, 561–570 (2004) [doi:10.1038/sj.eye.6700729].

51. D. Turbert and R. H. Janigian Jr, “What conditions can OCT help to diagnose? - American Academy of Ophthalmology,” 2018, <https://www.aao.org/eye-health/treatments/what-does-optical-coherence-tomography-diagnose> (accessed 10 May 2019).

52. A. Invernizzi, M. Cozzi, and G. Staurenghi, “Optical coherence tomography and optical coherence tomography angiography in uveitis: A review,” *Clin. Experiment. Ophthalmol.* **47**(3), 357–371, John Wiley & Sons, Ltd (10.1111) (2019) [doi:10.1111/ceo.13470].

53. A. Day et al., “The Royal College of Ophthalmologists - Ophthalmic Services Guidance Ophthalmic Imaging” (2016).

54. D. P. Popescu et al., “Optical coherence tomography: Fundamental principles, instrumental designs and biomedical applications,” *Biophys. Rev.* **3**(3), 155–169 (2011) [doi:10.1007/s12551-011-0054-7].

55. W. Drexler et al., “In vivo ultrahigh-resolution optical coherence tomography,” *Opt. Lett.* **24**(17), 1221–1223 (1999).

56. Z. Yaqoob, J. Wu, and C. Yang, “Spectral domain optical coherence tomography: a better OCT imaging strategy.,” *Biotechniques* **39**(6 Suppl) (2005) [doi:10.2144/000112090].

57. O. Ejofodomi, “Measurement of Optical Scattering Coefficient of the Individual Layers of the Human Urinary Bladder Using Optical Coherence Tomography,” *ISRN Biomed. Imaging* **2014**, 1–4 (2014) [doi:10.1155/2014/591592].

58. Y. Yang et al., “Optical scattering coefficient estimated by optical coherence tomography correlates with collagen content in ovarian tissue,” *J. Biomed. Opt.* **16**(9), 090504 (2011) [doi:10.1117/1.3625247].

59. L. Thrane et al., “Extraction of tissue optical properties from optical coherence tomography images for diagnostic purposes (Invited Paper),” 139 (2005) [doi:10.1117/12.634767].

60. D. Levitz et al., “Quantitative characterization of developing collagen gels using optical coherence tomography,” *J. Biomed. Opt.* **15**(2), 026019 (2010) [doi:10.1117/1.3377961].

61. C. Lau et al., “Early detection of high-grade squamous intraepithelial lesions in the cervix with quantitative spectroscopic imaging.,” *J. Biomed. Opt.* **18**(7), 76013, SPIE-SOC PHOTO-OPTICAL INSTRUMENTATION ENGINEERS, 1000 20TH ST, PO BOX 10, BELLINGHAM, WA 98225 USA (2013).

62. M. Mesradi et al., “Experimental and analytical comparative study of optical coefficient of fresh and frozen rat tissues.,” *J. Biomed. Opt.* **18**(11), 117010 (2013).

63. A. Roggan et al., “Effect of preparation technique on the optical parameters of biological tissue,” in Applied Physics B: Lasers and

Optics **69**(5), pp. 445–453 (1999).

64. Y. Tomita et al., “Ultrastructural changes during in situ early postmortem autolysis in kidney, pancreas, liver, heart and skeletal muscle of rats,” *Leg. Med.* **6**(1), 25–31 (2004).

65. K. V. Larin et al., “Noninvasive Blood Glucose Monitoring With Optical Coherence Tomography: A pilot study in human subjects,” *Diabetes Care* **25**(12), 2263–2267 (2002).

66. M. Friebel et al., “Influence of oxygen saturation on the optical scattering properties of human red blood cells in the spectral range 250 to 2000 nm,” *J. Biomed. Opt.* **14**(3), 034001, International Society for Optics and Photonics (2009) [doi:10.1117/1.3127200].

67. J. C. Finlay et al., “In vivo determination of the absorption and scattering spectra of the human prostate during photodynamic therapy,” *Proc SPIE* **5315**(215), 132–142, SPIE-INT SOC OPTICAL ENGINEERING, 1000 20TH ST, PO BOX 10, BELLINGHAM, WA 98227-0010 USA (2004).

68. G. Zonios et al., “Diffuse reflectance spectroscopy of human adenomatous colon polyps in vivo.,” *Appl. Opt.* **38**(31), 6628–6637 (1999).

69. I. Carneiro et al., “Kinetics of optical properties of human colorectal tissues during optical clearing: a comparative study between normal and pathological tissues,” *J. Biomed. Opt.* **23**(12), 1, International Society for Optics and Photonics (2018) [doi:10.1117/1.JBO.23.12.121620].

70. P. Flecknell, *Laboratory Animal Anaesthesia*, Elsevier Science (2015).

71. K. Yoshida et al., “Multispectral imaging of absorption and scattering properties of in vivo exposed rat brain using a digital red-green-blue camera.,” *J. Biomed. Opt.* **20**(5), 051026, SPIE-SOC PHOTO-OPTICAL INSTRUMENTATION ENGINEERS, 1000 20TH ST, PO BOX 10, BELLINGHAM, WA 98225 USA (2015).

72. T. S. Curry III, J. E. Dowdey, and R. C. Murry Jr., “Basic Interactions Between X Rays and Matter,” in Christensen’s Physics of Diagnostic

Radiography, 4th Editio, Lippincott Williams and Wilkins (1990).

73. J. Als-Nielsen and D. McMorrow, *Elements of Modern X-Ray Physics*, Second Edi, John Wiley & Sons, Inc. (2011) [doi:10.1002/9781119998365].

74. A. Bravin, P. Coan, and P. Suortti, “X-ray phase-contrast imaging: from pre-clinical applications towards clinics.,” *Phys. Med. Biol.* **58**(1), R1-35 (2013).

75. P. R. Munro et al., “The relationship between wave and geometrical optics models of coded aperture type x-ray phase contrast imaging systems,” *Phys. Med. Biol* **49**(16), 3573–3583 (2004).

76. W. C. Röntgen, “On a new kind of rays,” *Nature* **53**, 274–277 (1896).

77. C. Muehleman et al., “In-laboratory diffraction-enhanced X-ray imaging for articular cartilage,” *Clin. Anat.* **23**(5), 530–538 (2010) [doi:10.1002/ca.20993].

78. P. Suortti, J. Keyriläinen, and W. Thomlinson, “Analyser-based x-ray imaging for biomedical research,” *J. Phys. D. Appl. Phys.* **46**(49) (2013) [doi:10.1088/0022-3727/46/49/494002].

79. F. Arfelli et al., “Analyzer-based imaging system performance in a synchrotron clinical environment: A feasibility study,” *J. Instrum.* **12**(2) (2017) [doi:10.1088/1748-0221/12/02/C02062].

80. D. Chapman et al., “Diffraction enhanced x-ray imaging,” *Phys. Med. Biol.* **42**(11), 2015–2025 (1997) [doi:10.1088/0031-9155/42/11/001].

81. L. Rigon et al., “A new DEI algorithm capable of investigating sub-pixel structures,” *J. Phys. D. Appl. Phys.* **36**(10A), A107–A112 (2003).

82. M. N. Wernick et al., “Multiple-image radiography.”

83. L. Rigon, F. Arfelli, and R. H. Menk, “Generalized diffraction enhanced imaging to retrieve absorption, refraction and scattering effects,” *J. Phys. D. Appl. Phys.* **40**(10), 3077–3089 (2007) [doi:10.1088/0022-3727/40/10/011].

84. E. Pagot et al., “A method to extract quantitative information in analyzer-based x-ray phase contrast imaging,” *Appl. Phys. Lett.*

82(20), 3421–3423 (2003) [doi:10.1063/1.1575508].

85. P. C. Diemoz et al., “Absorption, refraction and scattering in analyzer-based imaging: comparison of different algorithms.,” *Opt. Express* **18**(4), 3494–3509 (2010).

86. M. Marenzana et al., “Synchrotron- and laboratory-based X-ray phase-contrast imaging for imaging mouse articular cartilage in the absence of radiopaque contrast agents.,” *Philos. Trans. A. Math. Phys. Eng. Sci.* **372**(2010), 20130127 (2014).

87. C. Liu et al., “X-ray diffraction-enhanced imaging of uterine leiomyomas.,” *Med. Sci. Monit. Int. Med. J. Exp. Clin. Res.* **11**(5), MT33-T38 (2005).

88. M. E. Kelly et al., “Diffraction-enhanced imaging of a porcine eye,” *Can. J. Ophthalmol.* **42**(5), 731–733, Canadian Ophthalmological Society (2007) [doi:10.3129/I07-132].

89. X. Zhang et al., “Visualising liver fibrosis by phase-contrast X-ray imaging in common bile duct ligated mice,” *Eur. Radiol.* **23**(2), 417–423 (2013) [doi:10.1007/s00330-012-2630-z].

90. G. Aulakh et al., “Multiple image X-radiography for functional lung imaging,” *Phys. Med. Biol.* **63**(1) (2018).

91. A. Olivo et al., “An innovative digital imaging set-up allowing a low-dose approach to phase contrast applications in the medical field,” *Med. Phys.* **28**(8), 1610 (2001).

92. A. Olivo and R. Speller, “A coded-aperture technique allowing x-ray phase contrast imaging with conventional sources,” *Appl. Phys. Lett.* **91**(7) (2007).

93. C. K. Hagen et al., “Low-dose phase contrast tomography with conventional x-ray sources.,” *Med. Phys.* **41**(7), 070701 (2014) [doi:10.1118/1.4884297].

94. P. R. T. Munro et al., “A simplified approach to quantitative coded aperture X-ray phase imaging,” *Opt. Express* **21**(9), 11187–11201 (2013).

95. P. C. Diemoz and A. Olivo, “On the origin of contrast in edge

illumination X-ray phase-contrast imaging.," *Opt. Express* **22**(23), 28199–28214 (2014).

96. P. C. Diemoz et al., "X-ray phase-contrast imaging with nanoradian angular resolution," *Phys. Rev. Lett.* **110**(13), 1–5 (2013).

97. P. C. Diemoz et al., "Sensitivity of laboratory based implementations of edge illumination X-ray phase-contrast imaging," *Appl. Phys. Lett.* **103**(24) (2013).

98. P. C. Diemoz et al., "Angular sensitivity and spatial resolution in edge illumination X-ray phase-contrast imaging," *Nucl. Instruments Methods Phys. Res. Sect. A Accel. Spectrometers, Detect. Assoc. Equip.* **784**, 538–541, Elsevier (2015).

99. P. C. Diemoz, F. a Vittoria, and A. Olivo, "Spatial resolution of edge illumination X-ray phase-contrast imaging.," *Opt. Express* **22**(13), 15514–15529 (2014).

100. G. K. Kallon et al., "A laboratory based edge-illumination x-ray phase-contrast imaging setup with two-directional sensitivity," *Appl. Phys. Lett.* **107**(20) (2015).

101. P. R. T. Munro et al., "Phase and absorption retrieval using incoherent X-ray sources," *Proc. Natl. Acad. Sci.* **109**(35), 13922–13927 (2012).

102. M. Endrizzi et al., "Hard X-ray dark-field imaging with incoherent sample illumination," *Appl. Phys. Lett.* **104**(2) (2014).

103. A. Olivo et al., "Low-dose phase contrast mammography with conventional x-ray sources," *Med. Phys.* **40**(9), 090701 (2013).

104. F. A. Vittoria et al., "Beam tracking approach for single-shot retrieval of absorption, refraction, and dark-field signals with laboratory x-ray sources," *Appl. Phys. Lett.* **106**(22) (2015).

105. P. C. Diemoz et al., "Single-image phase retrieval using an edge illumination X-ray phase-contrast imaging setup," *J. Synchrotron Radiat.* **22**(4), 1072–1077, International Union of Crystallography (2015).

106. M. Endrizzi and A. Olivo, "Absorption, refraction and scattering

retrieval with an edge-illumination-based imaging setup," *J. Phys. D. Appl. Phys.* **47**(50), 505102 (2014).

107. P. Modregger et al., "Small angle x-ray scattering with edge-illumination," *Sci. Rep.* **6**, 1–8, Nature Publishing Group (2016).

108. M. Endrizzi et al., "X-ray Phase-Contrast Radiography and Tomography with a Multiaperture Analyzer," *Phys. Rev. Lett.* **118**(24), 1–5 (2017) [doi:10.1103/PhysRevLett.118.243902].

109. M. Endrizzi et al., "Edge-illumination X-ray dark-field imaging for visualising defects in composite structures," *Compos. Struct.* **134**, 895–899, Elsevier Ltd (2015).

110. E. A. Miller et al., "Phase contrast X-ray imaging signatures for security applications," *IEEE Trans. Nucl. Sci.* **60**(1), 416–422 (2013).

111. T. P. Millard et al., "Quantification of microbubble concentration through x-ray phase contrast imaging," *Appl. Phys. Lett.* **103**(11), 16–20 (2013).

112. B. W. Pogue and M. S. Patterson, "Review of tissue simulating phantoms for optical spectroscopy, imaging and dosimetry," *J. Biomed. Opt.* **11**(4), 041102 1-16 (2006) [doi:10.1117/1.2335429].

113. G. Lamouche et al., "Review of tissue simulating phantoms with controllable optical, mechanical and structural properties for use in optical coherence tomography.," *Biomed. Opt. Express* **3**(6), 1381–1398 (2012) [doi:10.1364/BOE.3.001381].

114. R. G. Jensen, "The composition of bovine milk lipids: January 1995 to December 2000.," *J. Dairy Sci.* **85**(2), 295–350, Elsevier (2002).

115. B. Aernouts et al., "Effect of ultrasonic homogenization on the Vis/NIR bulk optical properties of milk," *Colloids Surfaces B Biointerfaces* **126**, 510–519, Elsevier B.V. (2015).

116. M. C. Michalski, V. Briard, and F. Michel, "Optical parameters of milk fat globules for laser light scattering measurements," *Lait.* **81**, 787–796 (2001).

117. M. C. Ambrose Griffin and W. G. Griffin, "A simple turbidimetric method for the determination of the refractive index of large colloidal

particles applied to casein micelles," *J. Colloid Interface Sci.* **104**(2), 409–415 (1985).

118. C. Lopez, "Focus on the supramolecular structure of milk fat in dairy prod- ucts.," *Reprod. Nutr. Dev.* **45**(4), 497–511 (2005).

119. S. T. Flock et al., "Optical properties of intralipid: A phantom medium for light propagation studies," *Lasers Surg. Med.* **12**(5), 510–519 (1992).

120. H. J. van Staveren et al., "Light scattering in Intralipid-10% in the wavelength range of 400-1100 nm.," *Appl. Opt.* **30**(31), 4507–4514 (1991).

121. C. Gallegos, P. Partal, and J. M. Franco, "Droplet-size distribution and stability of lipid injectable emulsions," *Am. J. Heal. Pharm.* **66**(2), 162–166 (2009).

122. P. Di Ninni, F. Martelli, and G. Zaccanti, "Intralipid: towards a diffusive reference standard for optical tissue phantoms.," *Phys. Med. Biol.* **56**(2), N21–N28 (2011).

123. S. L. (Oregon M. L. C. Jacques, "Optical Properties of Intralipid, an aqueous suspension of lipid droplets.," 1998, <http://omlc.org/spectra/intralipid/> (accessed 8 April 2016).

124. V. N. Du Le et al., "Measurements of extrinsic fluorescence in Intralipid and polystyrene microspheres.," *Biomed. Opt. Express* **5**(8), 2726–2735 (2014).

125. L. Spinelli et al., "Determination of reference values for optical properties of liquid phantoms based on Intralipid and India ink," *Biomed. Opt. Express* **5**(7), 2037 (2014).

126. N. Bodenschatz et al., "Surface layering properties of Intralipid phantoms," *Phys. Med. Biol.* **60**(2014), 1171–1183, IOP Publishing (2014).

127. S. Avtzi et al., "Fabrication and characterization of a 3-D non-homogeneous tissue-like mouse phantom for optical imaging," *Proc. SPIE* **9032**, 903206:1-6 (2013).

128. B. F. Kennedy et al., "Fibrin phantom for use in optical coherence

tomography," *J. Biomed. Opt.* **15**(3), 030507 (2010).

129. J. R. Cook, R. R. Bouchard, and S. Y. Emelianov, "Tissue-mimicking phantoms for photoacoustic and ultrasonic imaging.," *Biomed. Opt. Express* **2**(11), 3193–3206 (2011).

130. D. Wang, Y. Chen, and J. T. Liu, "A liquid optical phantom with tissue-like heterogeneities for confocal microscopy," *Biomed Opt Express* **3**(12), 3153–3160 (2012).

131. C.-E. Bisaillon et al., "Deformable and durable phantoms with controlled density of scatterers.," *Phys. Med. Biol.* **53**(13), N237–N247 (2008) [doi:doi:10.1088/0031-9155/53/13/N01].

132. P. Krauter et al., "Optical phantoms with adjustable subdiffusive scattering parameters," *J. Biomed. Opt.* **20**(10), 105008 (2015).

133. C. Böcklin et al., "Mixing formula for tissue-mimicking silicone phantoms in the near infrared," *J. Phys. D. Appl. Phys.* **48**(10), 105402, IOP Publishing (2015) [doi:10.1088/0022-3727/48/10/105402].

134. J. R. Devore, "Refractive Indices of Rutile and Sphalerite," *J. Opt. Soc. Am.* **41**(6), 416 (1951).

135. M. J. Dodge, I. H. Malitson, and a I. Mahan, "A special method for precise refractive index measurement of uniaxial optical media.," *Appl. Opt.* **8**(8), 1703–1705 (1969).

136. I. H. Malitson, "Refraction and Dispersion of Synthetic Sapphire," *J. Opt. Soc. Am.* **52**(12), 1377 (1962).

137. M. Firbank and D. T. Delpy, "A design for a stable and reproducible phantom for use in near infra-red imaging and spectroscopy," *Phys. Med. Biol.* **38**(6), 847–853 (1993).

138. G. Beadie et al., "Refractive index measurements of poly(methyl-methacrylate) (PMMA) from 0.4–1.6μm," *Appl. Opt.* **54**(31), F139–F143 (2015).

139. N. Sultanova, S. Kasarova, and I. Nikolov, "Dispersion properties of optical polymers," *Acta Phys. Pol. A* **116**(4), 585–587 (2009).

140. I. H. Malitson, "Interspecimen Comparison of the Refractive Index of

Fused Silica," *J. Opt. Soc. Am.* **55**(10), 1205 (1965).

141. Bangs Laboratories Inc. Indiana. USA., "TechNote 202 - Microsphere Aggregation," 2003, <http://www.bangslabs.com/support/technical-support/technotes>.

142. D. Y. Diao et al., "Durable rough skin phantoms for optical modeling.," *Phys. Med. Biol.* **59**(2), 485–492 (2014) [doi:10.1088/0031-9155/59/2/485].

143. M. R. N. Avanaki et al., "Two applications of solid phantoms in performance assessment of optical coherence tomography systems.," *Appl. Opt.* **52**(29), 7054–7061 (2013) [doi:10.1364/AO.52.007054].

144. O. a Ejofodomi, V. Zderic, and J. M. Zara, "Tissue-mimicking bladder wall phantoms for evaluating acoustic radiation force-optical coherence elastography systems.," *Med. Phys.* **37**(4), 1440–1448 (2010).

145. K.-B. Sung et al., "Accurate extraction of optical properties and top layer thickness of two-layered mucosal tissue phantoms from spatially resolved reflectance spectra.," *J. Biomed. Opt.* **19**(7), 77002, International Society for Optics and Photonics (2014).

146. J. Baxi et al., "Retina-simulating phantom for optical coherence tomography.," *J. Biomed. Opt.* **19**(2), 021106 (2014) [doi:10.1117/1.JBO.19.2.021106].

147. S. Kleiser et al., "Comparison of tissue oximeters on a liquid phantom with adjustable optical properties," 43–55 (2015).

148. F. Martelli et al., "Optimal estimation reconstruction of the optical properties of a two-layered tissue phantom from time-resolved single-distance measurements.," *J. Biomed. Opt.* **20**(11), 115001 (2015).

149. S. Del Bianco et al., "Liquid phantom for investigating light propagation through layered diffusive media," *Opt. Express* **12**(10), 2102–2111 (2004).

150. R. R. LeVier et al., "What is silicone?," *J. Clin. Epidemiol.* **48**(4), 513–

517 (1995).

151. R. B. Saager et al., “Multilayer silicone phantoms for the evaluation of quantitative optical techniques in skin imaging,” in Proc. SPIE 7567, Design and Performance Validation of Phantoms Used in Conjunction with Optical Measurement of Tissue II **756706**, R. J. Nordstrom, Ed., pp. 756706 1-8, San Francisco, California (2010) [doi:10.1117/12.842249].

152. R. Bays et al., “Three-Dimensional Optical Phantom and Its Application in PDT,” *Lasers Surg. Med.* **21**(3), 227–234 (1997).

153. A. K. Dąbrowska et al., “Materials used to simulate physical properties of human skin.,” *Ski. Res. Technol.* **22**(1), 3–14 (2015).

154. A. Curatolo et al., “Quantifying the influence of Bessel beams on image quality in optical coherence tomography,” *Sci. Rep.* **6**, 23483, Nature Publishing Group (2016) [doi:10.1038/srep23483].

155. J. H. Koschwanez, R. H. Carlson, and D. R. Meldrum, “Thin PDMS films using long spin times or tert-butyl alcohol as a solvent,” *PLoS One* **4**(2), 2–6 (2009) [doi:10.1371/journal.pone.0004572].

156. M. S. Wróbel et al., “Nanoparticle-free tissue-mimicking phantoms with intrinsic scattering,” *Biomed. Opt. Express* **7**(6), 2088 (2016).

157. E. M. Ahmed, “Hydrogel: Preparation, characterization, and applications: A review,” *J. Adv. Res.* **6**(2), 105–121, Cairo University (2015).

158. D. R. White et al., “The composition of body tissues (ii) Fetus to young adult,” *Br. J. Radiol.* **64**(758), 149–159 (1991).

159. H. Q. Woodard and D. R. White, “The composition of body tissues.,” *Br. J. Radiol.* **59**(708), 1209–1218 (1986).

160. A. M. De Grand et al., “Tissue-Like Phantoms for Near-Infrared Fluorezcence Imaging System Assessment and the Training of Surgeons,” *J. Biomed. Opt.* **11**(1), 1–21 (2006).

161. G. Wagnières et al., “An optical phantom with tissue-like properties in the visible for use in PDT and fluorescence spectroscopy.,” *Phys. Med. Biol.* **42**(7), 1415–1426 (1997).

162. T. J. Hall et al., “Phantom Materials for Elastography,” *IEE Trans. Ultrason. Ferroelectr. Freq. Control* **44**(6), 1355–1365 (1997).

163. H. Kim et al., “3D printing-assisted fabrication of double-layered optical tissue phantoms for laser tattoo treatments,” *Lasers Surg. Med.* **48**(4), 392–399 (2016).

164. E. L. Madsen et al., “Tissue-mimicking oil-in-gelatin dispersions for use in heterogeneous elastography phantoms.,” *Ultrason. Imaging* **25**(1), 17–38 (2003).

165. K. W. Gossage et al., “Texture analysis of speckle in optical coherence tomography images of tissue phantoms.,” *Phys. Med. Biol.* **51**(6), 1563–1575 (2006).

166. Y. Hou et al., “Preparation of PVA hydrogel with high-transparence and investigations of its transparent mechanism,” *RSC Adv.* **5**(31), 24023–24030, Royal Society of Chemistry (2015).

167. F. Yokoyama et al., “Morphology and structure of highly elastic poly(vinyl alcohol) hydrogel preparaed by repeated freezing and melting/,” *Colloid Polym Sci* **264**(7), 595–601 (1986).

168. A. Kharine et al., “Poly(vinyl alcohol) gels for use as tissue phantoms in photoacoustic mammography,” *Phys. Med. Biol.* **48**(3), 357–370 (2003).

169. S. H. Hyon, W. I. Cha, and Y. Ikada, “Preparation of transparent poly(vinyl alcohol) hydrogel,” *Polym. Bull.* **22**(2), 119–122 (1989).

170. F. S. Goerlach et al., “Multi-Layered , 3D Skin Phantoms of Human Skin in the Wavelength Range 650-850nm,” in Intelligent Informatics and Biomedical Sciences (ICIIBMS), Track 3: Bioimformatics, Medical Imaging and Neuroscience, pp. 250–256 (2015).

171. N. Kiarashi et al., “Development of matched virtual and physical breast phantoms based on patient data,” *SPIE Med. Imaging Phys. Med. Imaging* **8668**, 866805 (2013).

172. B. Z. Bentz et al., “Printed optics: phantoms for quantitative deep tissue fluorescence imaging,” *Opt. Lett.* **41**(22), 5230–5233 (2016).

173. E. Maneas et al., “Gel wax-based tissue-mimicking phantoms for

multispectral photoacoustic imaging Gel wax-based tissue-mimicking phantoms for," *Biomed. Opt. Express* **9**(3), 1151–1163 (2018) [doi:https://doi.org/10.1364/BOE.9.001151].

174. E. Maneas et al., "Anatomically realistic ultrasound phantoms using gel wax with 3D printed moulds," *Phys. Med. Biol.* **63**(1), 015033, IOP Publishing (2018) [doi:10.1088/1361-6560/aa9e2c].

175. R. X. Xu et al., "Design and benchtop validation of a handheld integrated dynamic breast imaging system for noninvasive characterization of suspicious breast lesions.," *Technol. Cancer Res. Treat.* **7**(6), 471–481 (2008).

176. Z. Zhao et al., "3D printing of tissue-simulating phantoms for calibration of biomedical optical devices," in Proc. SPIE 10024, Optics in Health Care and Biomedical Optics VII, 100240N (2016) [doi:10.1117/12.2246273].

177. E. Dong and R. X. Xu, "Three-dimensional fuse deposition modeling of tissue-simulating phantom for biomedical optical imaging tissue-simulating phantom for biomedical optical" (2019) [doi:10.1117/1.JBO.20.12.121311].

178. J. Oudry et al., "Copolymer-in-oil Phantom Materials for Elastography," *Ultrasound Med. Biol.* **35**(7), 1185–1197 (2009) [doi:10.1016/j.ultrasmedbio.2009.01.012].

179. T. P. Millard, "Microbubbles as a quantitative contrast agent for x-ray phase contrast imaging," University College London (2014).

180. Wacker Chemie AG. Munich. Germany, "Overview of Elastosil grades silicone rubber for the appliance industry.," <https://www.wacker.com/cms/media/publications/downloads/6009_EN.pdf>.

181. T.-M. Lee et al., "Optical characterization of contrast agents for optical coherence tomography," *Int. Soc. Opt. Eng. San Jose, CA* **4967**, 129–134 (2003).

182. A. Aucejo et al., "Densities, Viscosities, and Refractive Indices of Some n-Alkane Binary Liquid Systems at 298.15 K," *J. Chem. Eng. Data* **40**(1), 141–147 (1995) [doi:10.1021/je00017a032].

183. I. Bodurov et al., “Modified design of a laser refractometer,” *Nanosci. Nanotechnol.* **16**, 31–33 (2016).

184. S. L. Jacques, “Origins of tissue optical properties in the UVA, visible, and NIR regions,” *OSA TOPS Adv. Opt. Imaging Phot. Migr.*(January 1996), 364–371 (1996).

185. Crystran Ltd. Poole. UK, “Silica Glass (SiO2) Data Sheet,” [doi:10.1038/067403a0].

186. Wacker Chemie AG. Munich. Germany, “Technical data sheet for Elastosil® RT 601 A/B.,” 2014, <https://www.wacker.com/cms/en/products/product/product.jsp?product=10461>.

187. A. Grimwood et al., “Elastographic contrast generation in optical coherence tomography from a localized shear stress.,” *Phys. Med. Biol.* **55**(18), 5515–5528 (2010) [doi:10.1088/0031-9155/55/18/016].

188. L. T. Zhuravlev, “The surface chemistry of amorphous silica. Zhuravlev model,” *Colloids Surfaces A Physicochem. Eng. Asp.* **173**(1–3), 1–38 (2000).

189. A. A. Christy, “Effect of Heat on the Adsorption Properties of Silica Gel,” *Int. J. Eng. Technol.* **4**(4), 484–488 (2012) [doi:10.1021/ie1018468].

190. A. Rimola et al., “Silica Surface Features and Their Role in the Adsorption of Biomolecules: Computational Modeling and Experiments,” *Chem. Rev.* **113**(6), 4216–4313 (2013) [doi:10.1016/S0927-7757(00)00556-2].

191. E. Papirer, H. Balard, and C. Vergelati, *Surfactant Science Series: Adsorption on Silica Surfaces*, E. Papiere, Ed., MARCEL DEKKER (2000).

192. A. Bradu et al., “Master slave en-face OCT/SLO,” *Biomed. Opt. Express* **6**(9), 3655, Optical Society of America (2015).

193. M. Schnaiter et al., “Measurement of Wavelength-Resolved Light Absorption by Aerosols Utilizing a UV-VIS Extinction Cell,” *Aerosol Sci. Technol.* **39**(3), 249–260 (2005).

194. Bangs Laboratories Inc. Indiana. USA., “Silica Microspheres - Product data Sheet 702” (2019).

195. R. M. Forbes, A. R. Cooper, and H. H. Mitchell, “The composition of the adult human body as determined by chemical analysis.,” *J. Biol. Chem* **203**, 359–366 (1953).

196. Y. Zhou et al., “Characterizing refractive index and thickness of biological tissues using combined multiphoton microscopy and optical coherence tomography,” *Biomed. Opt. Express* **4**(1), 38–50 (2013) [doi:10.1364/boe.4.000038].

197. F. P. Bolin et al., “Refractive index of some mammalian tissues using a fiber optic cladding method,” *Appl. Opt.* **28**(12), 2297, Optical Society of America (1989) [doi:10.1364/AO.28.002297].

198. T.-M. Lee et al., “Optical characterization of contrast agents for optical coherence tomography,” *Genet. Eng. Opt. Probes Biomed. Appl.* **4967**(September 2003), 129 (2003) [doi:10.1117/12.478396].

199. S. Ley et al., “Phantom materials mimicking the optical properties in the near infrared range for non-invasive fetal pulse oximetry,” *Conf. Proc. ... Annu. Int. Conf. IEEE Eng. Med. Biol. Soc. IEEE Eng. Med. Biol. Soc. Annu. Conf.* **2014**(August), 1432–1435 (2014) [doi:10.1109/EMBC.2014.6943869].

200. J. Narayanan, J. Y. Xiong, and X. Y. Liu, “Determination of agarose gel pore size: Absorbance measurements vis a vis other techniques,” *J. Phys. Conf. Ser.* **28**(1), 83–86 (2006) [doi:10.1088/1742-6596/28/1/017].

201. M. Hasan Nia et al., “Stabilizing and dispersing methods of TiO2 nanoparticles in biological studies,” *J. Paramed. Sci. Spring* **6**(2), 2008–4978 (2015).

202. E. A. Sergeeva et al., “Novel algorithm of processing optical coherence tomography images for differentiation of biological tissue pathologies,” *J. Biomed. Opt.* **10**(6), 064024 (2006) [doi:10.1117/1.2137670].

203. M. Almasian et al., “Validation of quantitative attenuation and backscattering coefficient measurements by optical coherence

tomography in the concentration-dependent and multiple scattering regime," *J. Biomed. Opt.* **20**(12), 121314, SPIE-Intl Soc Optical Eng (2015) [doi:10.1117/1.jbo.20.12.121314].

204. P. Ossowski et al., "Realistic simulation and experiment reveals the importance of scatterer microstructure in optical coherence tomography image formation," *Biomed. Opt. Express* **9**(7), 3122, The Optical Society (2018) [doi:10.1364/boe.9.003122].

205. M. Querry, "Optical Constants of Minerals and Other Materials from the Millimeter to the Ultraviolet" (1987).

206. Y.-T. Hung, S.-L. Huang, and S. H. Tseng, "Full EM wave simulation on optical coherence tomography: impact of surface roughness," in Biomedical Applications of Light Scattering VII **8592**, p. 859216, SPIE (2013) [doi:10.1117/12.2006107].

207. Kohzu Precision Co. Ltd., "Understanding X, XY Linear Stage," <https://www.kohzuprecision.com/technology/positioning-stages/motorized-stages/x-xy-stage/>.

208. M. Endrizzi, D. Basta, and A. Olivo, "Laboratory-based X-ray phase-contrast imaging with misaligned optical elements," *Appl. Phys. Lett.* **107**(12) (2015).

209. J. . Hubbel and S. M. Seltzer, "Tables of X-ray Mass Attenuation Coefficients and Mass Energy-Absorption Coefficients (Version 1.4)," 2004, <https://www.nist.gov/pml/x-ray-mass-attenuation-coefficients .National Institute of Standards and Technology, Ga>.

210. M. E. Poletti et al., "X-ray scattering from human breast tissues and breast-equivalent materials," *Phys. Med. Biol.* **47**(1), 47–63 (2002).

211. M. M. Swindle et al., "Swine as Models in Biomedical Research and Toxicology Testing," *Vet. Pathol.* **49**(2), 344–356 (2012) [doi:10.1177/0300985811402846].

212. F. Meurens et al., "The pig: A model for human infectious diseases," *Trends Microbiol.* **20**(1), 50–57 (2012) [doi:10.1016/j.tim.2011.11.002].

213. P. Giannios et al., "Visible to near-infrared refractive properties of

freshly-excised human-liver tissues: marking hepatic malignancies," *Sci. Rep.* **6**(1), 27910, Nature Publishing Group (2016) [doi:10.1038/srep27910].

214. R. L. P. . van Veen et al., "Determination of VIS- NIR absorption coefficients of mammalian fat, with time- and spatially resolved diffuse reflectance and transmission spectroscopy," SF4 (2014) [doi:10.1364/bio.2004.sf4].

215. Z. Kmiec, "Cooperation of liver cells in health and disease.," *Adv. Anat. Embryol. Cell Biol.* **161**, 1–151 (2001) [doi:10.1007/978-3-642-56553-3].

216. M. Strazzabosco and L. Fabris, "Functional Anatomy of Normal Bile Ducts," *Anat Rec* **291**(6), 653–660 (2008) [doi:10.1002/ar.20664].

217. A. R. Crawford, X. I. Z. Lin, and J. M. Crawford, "The normal adult human liver biopsy: A quantitative reference standard," *Hepatology* **28**(2), 323–331 (1998) [doi:10.1002/hep.510280206].

218. A. B. Farris et al., "Glomerular number and size in autopsy kidneys: The relationship to birth weight," *Kidney Int.* **63**(6), 2113–2122 (2003) [doi:10.1046/j.1523-1755.2003.00018.x].

219. J. R. Nyengaard, "Number and dimensions of rat glomerular capillaries in normal development and after nephrectomy," *Kidney Int.* **43**(5), 1049–1057, Elsevier Masson SAS (1993) [doi:10.1038/ki.1993.147].

220. O. Smithies, "Why the kidney glomerulus does not clog: A gel permeation/diffusion hypothesis of renal function," *Proc. Natl. Acad. Sci.* **100**(7), 4108–4113 (2003) [doi:10.1073/pnas.0730776100].

221. E. Maneas et al., "Gel wax-based tissue-mimicking phantoms for multispectral photoacoustic imaging," *Biomed. Opt. Express* **9**(3), 1151 (2018) [doi:10.1364/BOE.9.001151].

222. S. L. Vieira et al., "Paraffin-gel tissue-mimicking material for ultrasound-guided needle biopsy phantom," *Ultrasound Med. Biol.* **39**(12), 2477–2484 (2013) [doi:10.1016/j.ultrasmedbio.2013.06.008].

223. A. Olivo et al., "Design and realization of a coded-aperture based X-

ray phase contrast imaging for homeland security applications," *Nucl. Instruments Methods Phys. Res. Sect. A Accel. Spectrometers, Detect. Assoc. Equip.* **610**(2), 604–614, North-Holland (2009) [doi:10.1016/J.NIMA.2009.08.085].

224. B. Sheng et al., "Impaired mitochondrial biogenesis contributes to mitochondrial dysfunction in Alzheimer's disease.," *J. Neurochem.* **120**(3), 419–429, NIH Public Access (2012) [doi:10.1111/j.1471-4159.2011.07581.x].

225. N. E. Gray and J. F. Quinn, "Alterations in mitochondrial number and function in Alzheimer's disease fibroblasts," *Metab. Brain Dis.* **30**(5), 1275–1278 (2015) [doi:10.1007/s11011-015-9667-z].

226. M. Wee et al., "Tau Positive Neurons Show Marked Mitochondrial Loss and Nuclear Degradation in Alzheimer's Disease," *Curr. Alzheimer Res.* **15**(10), 928–937 (2018) [doi:10.2174/1567205015666180613115644].

227. E. Barrey et al., "Gene expression profiling in equine polysaccharide storage myopathy revealed inflammation, glycogenesis inhibition, hypoxia and mitochondrial dysfunctions.," *BMC Vet. Res.* **5**, 29, BioMed Central (2009) [doi:10.1186/1746-6148-5-29].